From Astrophysics of Galaxies to Binary Black Hole Mergers: Theoretical Modelling of the Gravitational-Wave Bias Parameter

by

Dorsa Sadat Hosseini Khajouei

A thesis
presented to the University of Waterloo
in fulfillment of the
thesis requirement for the degree of
Master of Mathematics
in
Applied Mathematics

Waterloo, Ontario, Canada, 2022

Author's Declaration

This thesis consists of material all of which I authored or co-authored: see Statement of Contributions included in the thesis. This is a true copy of the thesis, including any required final revisions, as accepted by my examiners.

I understand that my thesis may be made electronically available to the public.

Statement of Contributions

I am the sole author for Chapters 2, 3 and 4 which was written under the guidance of my advisor Ghazal Geshnizjani and were not written for the sake of publication.
The research presented in Chapter 5 is based on my research performed in collaboration with Amir Dehghani, Ph.D student at University of Waterloo and Leo Kim, Ph.D student at Queen's university, Dr. Alex Krowleski, Postdoctoral fellow University of Waterloo and Perimeter Institute, Prof. Suvodip Mukherjee, faculty at the Tata Institute of Fundamental Research and my supervisor Prof. Ghazal Geshnizjani faculty at University of Waterloo. At the time of writing this thesis, the research was in preparation for submission to be published.

Abstract

In the past few decades, the field of cosmology has become a fascinating field of study in physics. The computational advances and precision observational measurements such as Cosmic Microwave Background (CMB) measurements [13] and the Large Scale Structure (LSS) experiments [53] have thrust cosmology into the spotlight of modern physics. While research in cosmology explores the evolution of the universe on large scales, it is also closely connected from one end to the fundamental theories of physics such as theories of gravity and particle physics and from the other end to the astrophysical models and astronomical observations on small scales. Understanding the physics and formation of astronomical objects such stars or black holes can shed light on the physics of galaxy formation, nature of dark matter, models of gravity in strong field regime and history of the universe as a whole. In particular the detection of Gravitational Wave(GW) signals from binary compact objects since 2015 by the Laser Interferometer Gravitational-Wave Observatory (LIGO) collaboration [11], has opened the door to the new era of multi-messenger astronomy. Given the wealth of data we are expecting over the next few decades on this front specially including the next-generation detectors like Cosmic Explorer [57], and Einstein Telescope [55], exploring and understanding how this data with conjunction to the other astrophysical data such as galaxy surveys, can be utilized to understand the underlying physics is very crucial. The measurement of GWs is also a useful tool to understand the population of binary black holes and neutron stars and their merger rate in the universe. GW detections can also reveal the connection between the formation of binary compact objects and properties of stellar population like their brightness, star formation rate and mass [52]. Measuring these properties based on identification of an individual galaxy host of a single GW event may be unrealistic due to the large sky localization errors (even considering the next generation of GW detectors which may reach below one squared degree sensitivities). However, a statistical inference method could shed light on these properties by taking advantage of the correlation of their distribution to the matter density and large scale structure. This requires understanding and theoretical modeling of how their population traces large scale structure for different astrophysical models.

In this thesis, I will present our research on gravitational wave cosmology which lays the groundwork for one of the important aspects of these future studies: theoretical prediction of the GW bias parameter based on different choices of galaxy properties.

In particular, we develop a numerical framework for forecasting the the bias parameter for GW sources based on the observed galaxy surveys. This can provide important information about the astrophysical properties of the GW merger events, their environment and can also be used for cosmological inference models. To be more specific, We will

evaluate angular and 3-dimensional power spectrum and bias parameter of GWs given the parameters of astrophysical models using two galaxy surveys GLADE+ and Sloan Digital Sky Survey (SDSS) Data Release 7.

Our results even though preliminary and part of a bigger program still in progress, indicate some interesting features on how the bias parameter can be impacted by properties of the galaxies such as the stellar mass, metallicity and star formation rate.

It is worth mentioning that our numerical package is written such that it can easily be adopted to other galaxy surveys (photometric or spectroscopic) and accommodate different astrophysical assumptions. We are planning to make our code publicly available to scientific community in near future.

Acknowledgements

I would like to thank all people - both of academic and personal relations who made this thesis possible.
First and formost, I would like to express my appreciation to Ghazal Geshnizjani, my advisor, for her endless support and patience as I pursued my degree. I have been honoured to work with her over the two few years, she thought me lots of things both in scientific and personal aspects. I consider myself extremely fortunate to have such an exceptional advisor in every respect.
I thank my committee members Maite Dupuis and James Taylor for their very helpful and valuable feedback. I extremely grateful to Suvodip Mukherjee for his valuable guidance and leading role through out my thesis project. I thank Amir Dehghani, Leo Kim for their very helpful discussions and feedback as we collaborated. I am also really indebted to Alex Krolewski for all his help and guidance on the project, specifically his patience and the countless time he spent to provide me feedback while working with galaxy surveys.
Last but not least, I want to express my gratitude to my parents and sister for their patience and unwavering support of my goals from the beginning. I wouldn't have had the chance or the courage to explore my scientific interests without them. I am grateful to have them in my life for beyond words. I also want to thank my best friend Atiyeh Ahmadi for fun and support.
I would also like to thank our other group members Jerome Quintin, Brayden Hull, Elly Moghtaderi for their helpful comments during group meetings.
Finally, I acknowledge the support of the Natural Sciences and Engineering Research Council of Canada (NSERC) throughout the course of my degree. This work was made possible by the facilities of Perimeter Institute which helped me to run my python codes. In this work, some software and python tools have been used namely Nbodykit[7], Astropy[1], Healpy[4] and Scipy [9] and Numpy [8]. I acknowledge that I live and work on the traditional territory of the Neutral, Anishinaabeg and Haudenosaunee peoples. The University of Waterloo is situated on the Haldimand Tract, the land promised to the Six Nations that includes ten kilometres on each side of the Grand River.

Dedication

This is dedicated to my lovely parents and sister.

Table of Contents

List of Figures

List of Tables

Chapter 1

Introduction

Our mysterious universe has always incited humans to discover its deep secrets. Cosmology fulfills this ambition by creating a harmony between the mathematical and foundational theories of physics and the experimental data i.e. it provides a self consistent picture to analyse the entire universe. In recent decades, significant progress has been made in observational cosmology which has made physicists refer to the current state of cosmology as "the golden era of cosmology"[1]. This is thanks to precision measurements of cosmic microwave background [13, 14], the redshift surveys that can map the 3D distribution of matter and many other impressive astrophysical observations [59].
Meanwhile another observational front that has recently opened up to us is through gravitational wave experiments. Albert Einstein hypothesized gravitational waves as some perturbations in the space-time geometry which is produced by a moving mass which propagate from their source at extremely high velocity. The first direct detection of gravitational waves was achieved in 2015, when the Laser Interferometer Gravitational-Wave Observatory (LIGO) detectors in Livingston, Louisiana, and Hanford, Washington, detected a GW event corresponding to merging of two stellar black holes [11]. Discovery of gravitational waves provides an extraordinary chance to scientists for the first time in history to explore space and the physics of the coalescence of the compact objects like binary systems of black holes (BBH), neutron stars (BNS) and neutron star-black hole (NSBH) directly and independent from electromagnetic radiations and particle emissions.
Another potential implication of collecting more gravitational waves data in the upcoming years is that since they encode luminosity distances, using them along with existing electromagnetic signals data (which provide redshift) may shed light on the debates about

[1]Mentioned in several papers on the NASA/ADS website.

cosmological parameters such as Hubble tension [67]. However, most of the GWs are not expected to have electromagnetic counterpart which means to break the degeneracy between redshift and other cosmological parameters such as Hubble constant, statistical inference models should be used. [43, 22]. In addition to inferring cosmological properties, an abundance of GWs data can also provide us a window into exploring other astrophysical questions such as properties of the host galaxies.
In the research presented in this thesis, I will describe our approach to address one of the important and necessary aspects for future studies of GWs: theoretical prediction of the GW bias parameter based on different choices of galaxy and merger properties. This can provide valuable information about the astrophysical properties of the GW merger events, their merger rate and also their relation to the properties of the stars and galaxies. It is also a useful tool for cosmological inference models. In particular, we develop a numerical framework for forecasting the bias parameter for GW sources based on the observed galaxy surveys. To be more specific, I will describe how our frame work can be used to evaluate angular and 3-dimensional power spectrum and bias parameter of GWs given the parameters of astrophysical models using two galaxy surveys GLADE+ [24] and Sloan Digital Sky Survey (SDSS) Data Release 7 [59] .

The outline of this thesis will be as follows: in chapter (2), I will provide a brief review of the theory of standard cosmology and some updates on current status of observations. Then in chapter (3), I will present a brief discussion about statistical cosmology which will be used for the observational data analysis and the theory of Large Scale Structure (LSS). In chapter (4), I will go over the theory of gravitational waves, cosmic distance estimation from dark sirens, gravitational wave detectors and astrophysical background on the life cycle of a star, black hole and binary formation, and finally gravitational wave signal emitted by their merger. Then in chapter (5), I will present my work on modeling GW bias parameter based on specific astrophysical models including different astrophysical properties such as metallicity, star formation rate (SFR) and stellar mass of galaxy populations as well as mass distribution of black hole in binary black hole mergers. In particular, I explore the dependence of angular, 3-dimensional power spectrum and bias parameter of GWs to parameters of these models when applying to observed galaxy population in GLADE+ and Sloan Digital Sky Survey Data (SDSS) Release 7 catalogs. Finally, in chapter 6, I summarize our results and conclude that bias parameter will be affected by selecting host sirens based on the astrophysical properties of the host galaxies. In the case of galaxies' random selection, the bias fluctuates around one and will increase and deviate from one when we start selecting host galaxies based on their masses or SFR.

Chapter 2

Cosmology

In this chapter, I will use general relativity to describe a cosmological model.
To be more precise, I will describe toolbox metric and Einstein's theory of gravity to construct *Friedmann-Lemaître-Robertson-Walker (FLRW)* metric and Friedmann equations to finally get the standard model of cosmology. This chapter's theoretical backgrounds are motivated by "lecture notes on general relativity" by Sean Carroll [21], "Cosmology" by Daniel Baumann [15], "Cosmology" by Steven Weinberg [63], the [33] and [43].

2.1 Einstein Field Equations (EFEs)

In Einstein's general theory of gravity, the geometry of space-time is described through metric (which describes curvature of the manifold). Therefore, in General Relativity, EFEs (first proposed by Einstein in the 1900s) express the relation between local space-time curvature and the local energy and momentum tensor. This is similar to Maxwell's equations which express how the electric and magnetic fields depend on charges and currents.
EFEs reduce to the Newtonian laws of gravity in the limit of weak field gravitational approximation with lower velocities than spped of light.
Assuming a given 3+1 D space-time manifold M and a metric tensor $g_{\mu\nu}$ [1] defined on the manifold, we have space-time line element as :

$$ds^2 = g_{\mu\nu} dx^\mu dx^\nu, \tag{2.1}$$

[1] In this section, Greek indices are used for space-time, and Latin indices for space and the signature is $g_{\mu\nu} = diag(1, -1, -1, -1)$

in which, dx^μ, dx^ν are basis dual vectors.

Einstein Field Equations can be presented as:

$$G_{\mu\nu} = 8\pi G T_{\mu\nu}. \tag{2.2}$$

A set of coupled non-linear second-order partial differential equations. They express how space-time interacts with matter. G is the Newton's constant of gravitation, $G_{\mu\nu}$ is the Einstein tensor given by

$$G_{\mu\nu} \equiv R_{\mu\nu} - \frac{1}{2} R g_{\mu\nu}, \tag{2.3}$$

R is the Ricci scalar which obeys:

$$R = R^\mu_\mu = g^{\mu\nu} R_{\mu\nu}, \tag{2.4}$$

where $g^{\mu\nu}$ is the inverse metric and $R_{\mu\nu}$ is the Ricci tensor which itself is obtained from Christoffel coefficients as follows:

$$R_{\mu\nu} = \partial_\lambda \Gamma^\lambda_{\mu\nu} - \partial_\nu \Gamma^\lambda_{\mu\lambda} + \Gamma^\lambda_{\lambda\rho} \Gamma^\rho_{\mu\nu} - \Gamma^\rho_{\mu\lambda} \Gamma^\lambda_{\nu\rho}, \tag{2.5}$$

in which affine connection (Christoffel coefficients) follow :

$$\Gamma^\lambda_{\mu\nu} = \frac{1}{2} g^{\lambda\rho} (\partial_\mu g_{\nu\rho} + \partial_\nu g_{\rho\mu} - \partial_\rho g_{\mu\nu}). \tag{2.6}$$

$T_{\mu\nu}$ is the energy-momentum tensor describing the matter fields. Therefore, the left-hand side of Eq. (2.2) describes the geometry of the space-time manifold while the right-hand side incorporates all dependencies on the matter content in the problem.
In cosmology to leading order, we can describe most of the matter content of the Universe as perfect fluids, which can be written as:

$$T_{\mu\nu} = (\rho + P) U_\mu U_\nu + P g_{\mu\nu}, \tag{2.7}$$

where U^μ is the fluid four-velocity and ρ, P are the energy and momentum densities. Note that, in the case of the perfect fluid observed by a comoving observer (an observer who is moving by Hubble flow) stress-energy tensor will reduce to

$$T^\mu_\nu = g^{\mu\nu} T_{\lambda\nu} = diag(\rho, -P, -P, -P). \tag{2.8}$$

Taking the trace of (2.2) EFEs can also be written as:

$$R_{\mu\nu} = 8\pi G (T_{\mu\nu} - \frac{1}{2} T g_{\mu\nu}). \tag{2.9}$$

Note that, the vaccume Einstein's equation correspond to $R_{\mu\nu} = 0$, since in vaccume we have $T_{\mu\nu} = 0$.

2.2 *Friedmann-Lemaître-Robertson-Walker (FLRW)* Metric

In special relativity, space-time is considered to be flat and independent of the matter content. therefore, the Minkowski metric can be defined as

$$g_{\mu\nu} = diag(1, -1, -1, -1). \tag{2.10}$$

In general relativity, the Minkowski metric can still describe a special isotropic and homogeneous vacuum space-time that we often have. Matter and energy sources induce curvature to the geometry of space-time metric, and the metric generically depends on space-time positions, $g_{\mu\nu}(t, x^i)$.
In cosmology, since the spatial distribution of matter and radiation in the Universe on sufficiently large scales is homogeneous and isotropic (meaning that there is no preferred direction and location in the Universe), space-time is often approximated by *Friedmann-Lemaître-Robertson-Walker (FLRW)* metric [2], where the 4-dimensional line element can be written as

$$ds^2 = dt^2 - a(t)^2 dl^2. \tag{2.11}$$

Here $a(t)$ is the scale factor, characterizing the expansion (or contraction) of the Universe, and dl^2 is the so-called co-moving spacial line element given by

$$dl^2 = \frac{dr^2}{1 - kr^2} + r^2(d\theta^2 + sin\theta^2 d\phi^2). \tag{2.12}$$

The constant parameter k characterizes the curvature of comoving spacial hyper-surfaces, taking the values $0, 1, -1$ for flat, positive and negative curvature 3-dimensional spaces.
The above metric is referred to as *FLRW* metric, which is the basis for describing the cosmological background evolution of the Universe.

2.3 Friedmann Equations

The cosmos is composed of a variety of matter components. Now we want to see how these matter sources connect to cosmological background evolution, i.e. time variation of the scale factor, $a(t)$ introduced earlier in the FLRW metric (2.11).

[2] Cosmologists use variety of observation tests to make sure this assumption is justified

For this purpose, we need first to calculate the Einstein tensor $G_{\mu\nu}$ for FLRW metric, for which we need first to find Ricci tensor and Ricci scalar defined in (2.5) and (2.4). Due to the isotropy of the FLRW metric, the three-vector $R_{i0} = R_{0i}$ both vanish. The non-vanishing components are R_{00}, R_{ij} which can be calculated as following using (2.5):

$$\begin{aligned} R_{00} &= \partial_\lambda \Gamma^\lambda_{00} - \partial_0 \Gamma^\lambda_{0\lambda} + \Gamma^\lambda_{\lambda\rho}\Gamma^\rho_{00} - \Gamma^\rho_{0\lambda}\Gamma^\lambda_{0\rho} = -\partial_0 \Gamma^i_{0i} - \Gamma^i_{0j}\Gamma^j_{0i} \\ R_{ij} &= \partial_\lambda \Gamma^\lambda_{ij} - \partial_j \Gamma^\lambda_{i\lambda} + \Gamma^\lambda_{\lambda\rho}\Gamma^\rho_{ij} - \Gamma^\rho_{i\lambda}\Gamma^\lambda_{j\rho}. \end{aligned} \tag{2.13}$$

Which given $\Gamma^i_{0j} = \frac{\dot{a}}{a}\delta^i_j$ leads to

$$\begin{aligned} R_{00} &= -\frac{d}{dt}(3\frac{\dot{a}}{a}) - 3(\frac{\dot{a}}{a})^2 = -3(\frac{\ddot{a}}{a}) \\ R_{ij} &= -[\frac{\ddot{a}}{a} + 2(\frac{\dot{a}}{a})^2 + 2\frac{k}{a^2}]\ g_{ij}. \end{aligned} \tag{2.14}$$

The fact that we obtained $R_{ij} \propto g_{ij}$ is compatible with the homogeneity and isotropy of FLRW metric. Ricci scalar can also be evaluated as

$$R = g^{\mu\nu}R_{\mu\nu} = g^{00}R_{00} - g^{ii}R_{ii} = R_{00} - \frac{1}{a^2}R_{ii} = -6[\frac{\ddot{a}}{a} + (\frac{\dot{a}}{a})^2 + \frac{k}{a^2}]. \tag{2.15}$$

Therefore, non-vanishing elements of Einstein tensors are

$$\begin{aligned} G^0_0 &= g^{0\lambda}G_{\lambda 0} = 3[(\frac{\dot{a}}{a})^2 + \frac{k}{a^2}] \\ G^i_j &= [2\frac{\ddot{a}}{a} + (\frac{\dot{a}}{a})^2 + \frac{k}{a^2}]\delta^i_j\ . \end{aligned} \tag{2.16}$$

At this step, we calculated the left-hand side of the EFEs (Einstein tensors), and assuming perfect fluid approximation, the right-hand side (stress-energy tensor) can be computed using Eq. (2.8) as

$$\begin{aligned} T^0_0 &= \rho \\ T^i_j &= -P. \end{aligned} \tag{2.17}$$

Now substituting (2.17) and (2.16) in the EFEs, **Friedmann equations** are obtained,

$$\begin{aligned} (\frac{\dot{a}}{a})^2 &= \frac{8\pi G}{3}\rho - \frac{k}{a^2} \\ \frac{\ddot{a}}{a} &= \frac{-4\pi G}{3}(\rho + 3P). \end{aligned} \tag{2.18}$$

Here, ρ and P represent the total energy density in the Universe, including radiation energy density (ρ_r), matter energy density (ρ_m) and cosmological constant (ρ_Λ)[3] and their corresponding pressure. Sometimes $-\frac{k}{a^2}$ is also referred to as curvature energy density ρ_k. Eq. (2.18) can also be written as

$$\begin{aligned} H^2 &= \frac{8\pi G}{3}\rho - \frac{k}{a^2} \\ \dot{H} + H^2 &= \frac{-4\pi G}{3}(\rho + 3P), \end{aligned} \tag{2.19}$$

in which $H \equiv \frac{\dot{a}}{a}$ is called the Hubble parameter, characterizing the logarithmic expansion rate of the Universe.

After the radiation and matter components are decoupled, one can write **Continuity equation** for each component as

$$\dot{\rho}_i + 3\frac{\dot{a}}{a}(\rho_i + P_i) = 0. \tag{2.20}$$

Similarly, one can write **Equation of state** for components as

$$P = \rho w, \tag{2.21}$$

where $w = 0, 1/3, -1$, is the constant of the equation of state for matter, radiation and vacuum energy, respectively.

In the Newtonian limit and non-relativistic particles, i.e. dust, pressure is negligible and can be ignored ($P = 0$), leading to $w = 0$. Whereas, for relativistic particles and in the perfect fluid approximation, it can be shown that pressure is related to density as $P = 1/3\rho$. Using Eqs. (2.20) and (2.21), one can get energy density as

$$\rho \propto a^{-3(1+w)}, \tag{2.22}$$

which can also apply to curvature density by setting $w = -\frac{1}{3}$, so the energy density for dust, radiation, curvature and the cosmological constant are proportional to a^{-3}, a^{-4}, a^{-2} and a^0, correspondingly.

In the following, we use the subscript '0' to represent today's quantities ($t = t_0$). For instance, $a_0 = a(t_0)$ is the scale factor today, which we set to unity: $a_0 = 1$ and H_0 is today expansion rate.

We also define today's critical density and dimensionless density parameters as

$$\begin{aligned} \rho_{crit,0} &= \frac{3H_0^2}{8\pi G} = 2.8 \times 10^{11} \quad h^2 M_\odot pc^{-3} \\ \Omega_{I,0} &= \frac{\rho_{I,0}}{\rho_{crit,0}} \quad \text{where} \quad \sum_I \Omega_{I,0} = 1. \end{aligned} \tag{2.23}$$

[3]Energy density of the dark energy

Where H_0 is the so-called Hubble constant will be expressed in the following. Finally, Eq. (2.19) can be rewritten as the following

$$H^2(a) = H_0^2\ [\Omega_{r,0}(\frac{a_0}{a})^4 + \Omega_{m,0}(\frac{a_0}{a})^3 + \Omega_{k,0}(\frac{a_0}{a})^2 + \Omega_{\Lambda,0}]. \tag{2.24}$$

From (2.24), we can see when the scale factor was negligible (in the early Universe), the first term in the Friedmann equation contributed dominantly over other terms. The Universe was first in the radiation-dominated era; then, at a special value of **a**, the second term started dominating, the Universe entered its matter-dominated phase, and finally, the last term started to dominate over matter density at a point. Note that, in the real Universe, the spacial curvature density has been measured to be close to 0, so for the rest of the thesis, we set $k = 0$.

2.4 Redshift

We can deduce everything about the cosmos from the light emitted by a distant galaxy. It can be interpreted both classically (as photons propagating in space-time) and quantum mechanically (as propagating photons).
In *quantum mechanic* scenario, the wavelength related to momentum as $\lambda = h/p$ and $p \propto a^{-1}(t)$ so the observed photons at time t_0 have wavelength λ_0 which obeys

$$\lambda_0 = \frac{a(t_0)}{a(t_1)}\lambda_1, \tag{2.25}$$

where λ_1, a_1 are the wavelength and expansion rate in the emission time. Since $\frac{a_0}{a_1} > 1$, we conclude the wavelength of light will be stretched by the expansion of the Universe ($\lambda_0 > \lambda_1$).
In another scenario, we consider light as an electromagnetic wave. In this case, consider a wave emitted from a galaxy at a co-moving distance d and at time $\eta_1$which observed at time $\eta_0 = \eta_1 + d$ then, as we know, the conformal duration time is the same from both detectors and source's points of view but the physical time is different and can be written as

$$\Delta t_i = a(\eta_i)\Delta\eta \qquad i = 0, 1 \tag{2.26}$$

where Δt is the period of light-wave and we have $\lambda_i = \Delta t_i$. So that

$$\frac{\lambda_1}{\lambda_0} = \frac{a(\eta_1)}{a(\eta_0)}. \tag{2.27}$$

Now we can introduce *redshift* as the difference in the light wavelength and can be written as

$$z \equiv \frac{\lambda_0 - \lambda_1}{\lambda_1} = \frac{a(t_0)}{a(t_1)} - 1, \tag{2.28}$$

where λ_0, λ_1 are the wavelength of light in the emission and observation time. By considering, $a(t_0) \equiv 1$ we have

$$1 + z = \frac{1}{a(t_1)}, \tag{2.29}$$

for close galaxies, we have

$$a(t_1) = a(t_0) - a(t_0)(t_1 - t_0)H_0 + \dots\ , \tag{2.30}$$

where $H_0 \equiv \frac{\dot{a}(t_0)}{a(t_0)}$, then Eq. (2.29) comes as

$$z = H_0(t_0 - t_1) + ..., \tag{2.31}$$

which for nearby sources we have $t_0 - t_1 \simeq d$ (since $c = 1$). Therefore, redshift increases with co-moving distance as (see Eq. (2.12))

$$z \simeq H_0 d. \tag{2.32}$$

2.5 Cosmological Distances

- **Co-moving distance and physical distance** are two closely related distance measurements that cosmologists employ to specify distances between objects in the Universe.
  Physical (proper) distance is a notion of distance which describes the distance between two points with considering the expansion of the Universe. In contrast, co-moving distance is the measured distance between two objects in the Universe by factoring out the Universe's expansion. Co-moving distance and physical distance can be related by

  $$\frac{D_p(t)}{a(t)} = \chi, \tag{2.33}$$

  in which $D_p(t)$, χ are the physical distance and the co-moving distance, respectively. Furthermore, the co-moving distance can be calculated as

  $$\chi = \int_{t_e}^{t_{obs}} \frac{dt}{a(t)} = \int_0^z \frac{dz}{H(z)}, \tag{2.34}$$

where t_e, t_{obs} are the time photons emitted and observed by detectors and $a(t)$ are the scale factor.

- **Metric distance**
  First, consider the FLRW metric in the form

$$ds^2 = dt^2 - a^2(t)[d\chi^2 + S_k^2(\chi)d\Omega^2]. \tag{2.35}$$

  In which

$$S_k(\chi) = \begin{cases} R_0 \sinh(\chi/R_0), & k = -1 \\ \chi, & k = 0 \\ R_0 \sin(\chi/R_0), & k = 1 \end{cases} \tag{2.36}$$

  Then the metric distance comes as

$$d_m = S_k(\chi). \tag{2.37}$$

  For example, in the flat Universe where $k = 0$, the metric distance is the same as the co-moving distance χ.

- **Angular diameter distance** the angular diameter distance D_A is another helpful distance measurement. Assume an object located in the co-moving distance χ and photons are emitted at time t_1 and observed at time t_0, the *Angular diameter distance* comes as

$$d_A = \frac{D}{\delta\theta}, \tag{2.38}$$

  considering the FLRW metric, D is

$$D = a(t_1)S_k(\chi)\delta\theta. \tag{2.39}$$

  Finally *Angular diameter distance* can be calculated as

$$d_A = \frac{d_m}{1+z}. \tag{2.40}$$

- **Luminosity distance**

  If we consider an exploding supernova (standard candle), the received flux can be used to derive its luminosity distance and comes as

$$F = \frac{L}{4\pi\chi^2}. \tag{2.41}$$

Where L is the luminosity (the amount of observed energy per second) and χ is the so-called co-moving distance.
Note that, in the FLRW space-time:
The observed photon rate to the emitted rate is $1/(1+z)$, and we also have $\frac{E_{obs}}{E_{emi}} = \frac{1}{1+z}$.
So that, Eq. (2.41) can be modified as

$$F = \frac{L}{4\pi d_m^2 (1+z)^2} \ , \tag{2.42}$$

in which, $d_L = d_m(1+z)$ is the luminosity distance.

2.6 Measurement of Present-Day Hubble Constant

Since Edwin Hubble's discovery of the expansion of the Universe in 1929, the Hubble constant has been the most significant parameter characterizing cosmology which expresses the expansion rate of the Universe. On the largest scales, the Universe's expansion can be considered homogeneous and isotropic, so all its components recede from one another. General relativity demonstrates that due to the Universe's expansion, a distant object's emitted radiation wave becomes redshifted by propagating from the source toward an observer.(see Eq. (2.32)).Today H_0 measurement of the Hubble Constant is $H_0 \simeq 67\ km\ s^{-1}Mpc^{-1}$ and the Hubble time can be calculated by $1/H_0$ [67].

2.6.1 Hubble Tension

In recent years, there has been much discussion about the local Hubble parameter measurements, which is arguably one of the most widely discussed topics in cosmology right now. The debates can be divided roughly into two parts: direct measurements of H_0 from the late Universe and indirect measurements of H_0 from the early Universe. The better techniques one can use, the more precise H_0 estimation can be achieved, and the measurement uncertainties will be decreased. Fig. (2.1) provides a useful reference for the subsequent Hubble constant landscape discussion. As one can see, different methods do not agree on the range of the estimated H_0 value; this discrepancy is known as the *Hubble tension*.

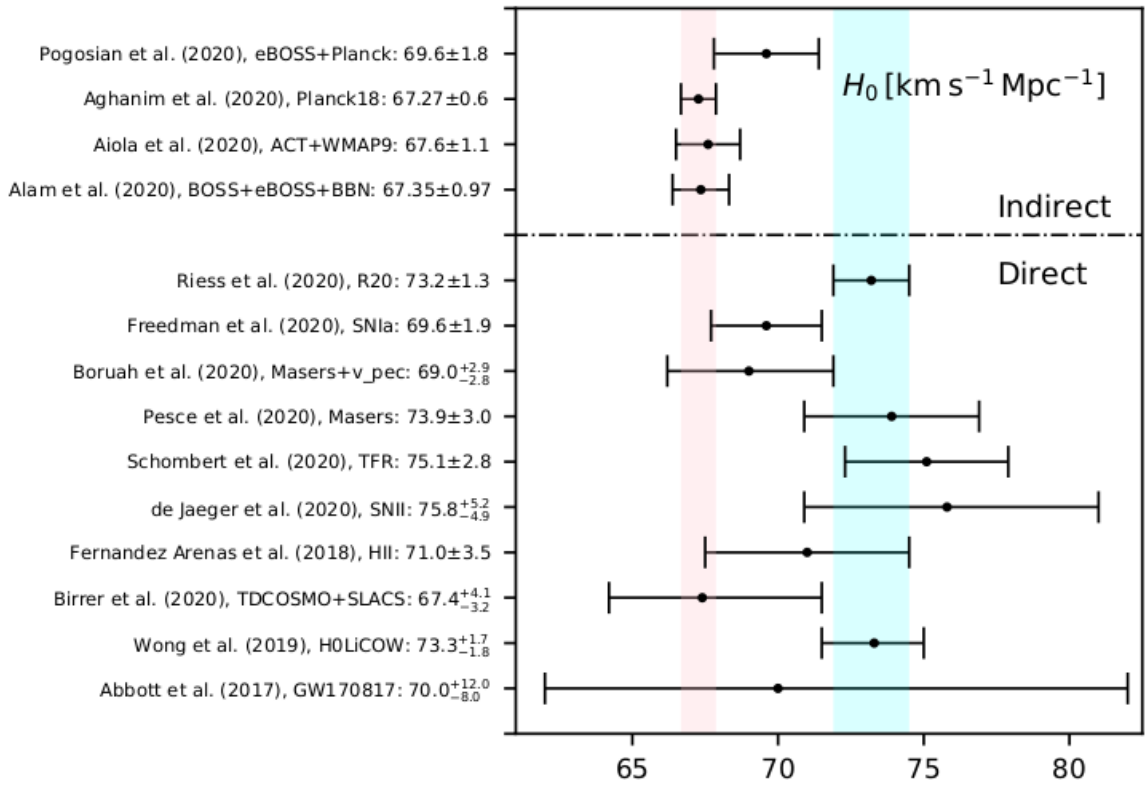

Figure 2.1: H_0 measurement from different methods. The pink band corresponds to the Planck 2018 measurement of H_0 [13] whereas The blue band is characterizing H_0 value from the SH0ES team (R20) [58]. This is a scaled-down version of the figure in [67], produced by the sample code (https://github.com/lucavisinelli/H0TensionRealm) and edited in [43].

2.6.2 Different Methods of Measuring H_0

- **Cosmic distance ladder**
  The ladder method (mostly for late Universe measurement of H_0) comes into the picture since there is no method to measure all ranges of distances to celestial objects in the Universe. The cosmic distance ladder is a series of overlapping methods used by astronomers to measure distances between objects in the Universe, ranging from nearby planets to the most distant quasars and galaxies. Fig. (2.2) shows a distance ladder; one can see that solar system distances can be established by direct measurement. Different geometrical techniques can be used to calculate the distances to stars within a few thousand light-years. Still, the Hipparcos satellite's measurements of the annual parallax of about 10,000 nearby stars provide the most precise distance estimates. The main-sequence fitting technique works for clusters with a distance of about 60,000 light-years. Going further into the Milky Way Galaxy, approximately 100 million light-years, the most reliable method for determining distances is the period-luminosity relation of Cepheid variables, supported by similar observations of much brighter stars such as RR Lyrae stars and novae. For more distant galaxies, brighter objects are required, like standard candles, which can be useful for up to about 3 billion. All mentioned ladder techniques agree on reporting $the H_0$ value from late universe methods to be about 73 km/s Mpc[67],[6].

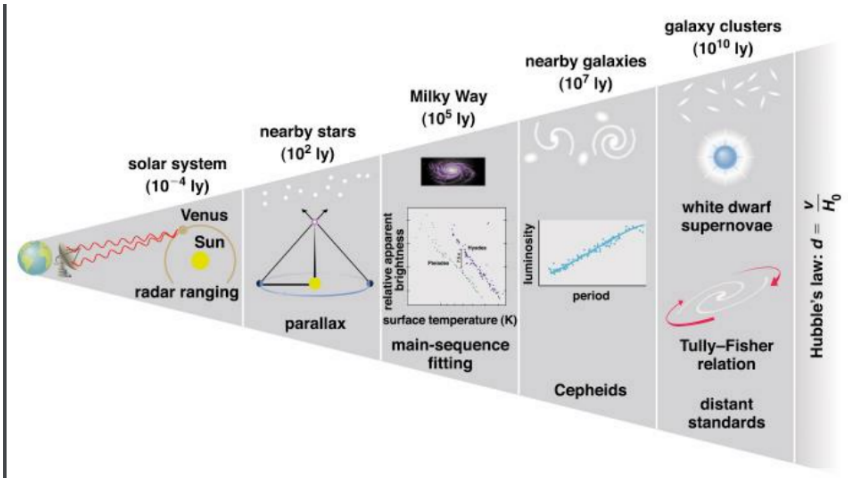

Figure 2.2: Cosmic distance ladder. Adopted from "The Essential Cosmic Perspective," Bennett et al.

- **Cosmic Microwave Background and Large Scale Structure**
  If one considers a cosmological model to be a flat ΛCDM (cosmological constant plus cold dark matter), then the H_0 measurements deduced from Cosmic Microwave Background (CMB) observation such as Planck Satellite (Aghanim et al.2020, Planck18) and large scale structure data sets at high redshifts (Zhang, Huang 2019) are in some tension with the one estimated with cosmic distance ladder method. Invoking new physics that changes the sound horizon scale in the early Universe is one of the few theoretical approaches to resolving this tension. Doing so generates CMB and Baryon Acoustic Oscillations (BAO) constraints on the Hubble constant to agree with local estimations of H_0. However, tension would probably still exist so it is important that we have another independent method to estimate H_0 [67].

- **Standard sirens**
  The gravitational wave signals from binary black holes and neutron star mergers provide a new and independent method to measure the Hubble constant that might shed light on Hubble measurement tension. In this method, one can infer the luminosity distance to the host galaxies based on the emitted Gravitational Waves (GWs) from binary compact objects coalescence (named *standard sirens*). If an electromagnetic wave counterpart for the event is also observed, one can obtain the redshift of the host galaxy and then H_0 can be estimated. Unfortunately, so far only one such events with electromagnetic counterpart, GW170817, has been detected. The Hubble constant estimated based on this particular event is $70.0^{+12.0}_{-8.0}\ km\ s^{-1}\ Mpc^{-1}$(Abbott et al. (2017), GW170817). If GWs events do not have electromagnetic wave counterparts, the so-called *dark sirens*, one could use statistical methods to deduce redshift to host galaxies and estimate the Hubble constant. There has been one such estimates obtaining $H_0 = 75^{+25}_{-22}\ km\ s^{-1}\ Mpc^{-1}$ which is not very competitive with other methods. However, this is very intriguing given the forecast for upcoming GWs observations over the next decade. We will discuss this method in the following chapters [67].

Chapter 3

Large Scale Structure and Statistics

In this chapter, I will discuss statistics in astrophysics which is a useful tools for analysing astrophysical data which will be discussed in chapter (5), Large Scale Structure (LSS), correlation functions, power spectrum and bias parameter. This chapter's theoretical backgrounds are inspired from [36],[68],[39] and [43].

3.1 Statistics in Astrophysics

3.1.1 Brief Review of Basic Probability Theory

Let's consider that Ω represents the sample space from which potential outcomes are drawn and that $A \in \Omega$ represents an event selected from. The probability function p can be defined as a function that assigns a probability to an event. A probability function must adhere to the following axioms, called Kolmogorov axioms:

1. The probability of an event can not be negative:

$$p(X) \geq 0. \tag{3.1}$$

2. If $\forall i; A_i \in \Omega$ are mutually exclusive events meaning that any 2 events are disjoint ($\forall i, j;\ A_i \bigcap A_j = \varnothing$), then we have :

$$p(\bigcup_{i=1}^{\infty} A_i) = \sum_{i=1}^{\infty} p(A_i). \tag{3.2}$$

3. if $A = \Omega$ then :

$$p(\Omega) = 1. \tag{3.3}$$

In the following, some important properties are noted:

- For not necessarily disjoint events A, B :

$$p(A \cup B) = P(A) + p(B) - p(A \cap B). \tag{3.4}$$

- Probability of events A, B happening simultaneously is:

$$p(A \cap B) = p(A, B) = P(A|B)P(B), \tag{3.5}$$

where $P(A|B)$ is the *Conditional probability*. Note that if A, B are independent events then :

$$\begin{aligned} p(A|B) &= p(A) \\ P(B|A) &= p(B). \end{aligned} \tag{3.6}$$

Since $\bigcap$ is symmetric :

$$P(A, B) = p(B, A) \Rightarrow p(A|B)p(B) = p(B|A)p(A), \tag{3.7}$$

which leads to the so-called *Bayes' rule*, written as:

$$p(A|B) = \frac{p(B|A)p(A)}{p(B)}. \tag{3.8}$$

- For any independent $B_i \in \Omega$; $\bigcup_{i=1}^{k} B_i = \Omega$ where $i = 1...k$:

$$p(A) = \sum_{i=1}^{k} p(A \cap B_i). \tag{3.9}$$

This gives us the *total probability (marginalization) law* as

$$p(A) = \sum_{i=1}^{k} p(A|B_i)p(B_i). \tag{3.10}$$

This is a useful statistical tool in cosmology that will be discussed later in this chapter. In some cases, we can quantify physics by assigning a real number (*Random variable*) to an event.

- **Random variables**
  Are mapping events from event space to the real numbers in the state space. Here the set of real numbers is called a *Realization* and a random variable can be continuous or discrete. Now *the probability density function (pdf)* is the probability function that assigns a probability to a random variable realization. So that for random variables X, Y and pdf $p(x, y)$ (where x, y are realisations), Eq. (3.10) for the continuous case comes as

$$p_X(x) = \int p(x, y)dy = \int p(x|y)p(y)dy. \tag{3.11}$$

  It can also be called a marginalized probability density function for X over Y

3.1.2 Bayesian & Frequentist Statistics

Bayesian and frequentist are the two most well-known statistical approaches. When an event occurs numerous times, in the limit, when that number reaches infinity, its relative frequency turns into its probability which Frequentists know as a probability. While Bayesian probability interprets probability as a measure of a state of knowledge rather than a frequency.

- **Bayes' theorem**
  Can be described by Bayes' formula as the following:

$$p(M|D) = \frac{p(D|M)\ p(M)}{p(D)}. \tag{3.12}$$

  In which D, M are characterizing data and hypothesis (model), respectively.

  $p(M)$ is the probability of M being correct before seeing data; is called *prior* probability.

  $p(D|M)$ is the probability of observing data, given model (hypothesis) and is called *likelihood*.

  $p(D)$ is the probability of observing data considering all possible models; is called *Bayesian evidence*. It can be evaluated by integrating of likelihood over all parameters of the possible models.

  $p(M|D)$ is the probability of the model being true, given the data; is named *posterior* probability.

Since the data explosion of the 1990s, the Bayesian approach has been nearly universally accepted in cosmology owing to its numerous advantages.
The Bayesian approach facilitates the incorporation of multiple data sets. For instance, you could use Bayes' theorem to update the prior probability with new data sets where the prior probability (on the model space M) was originally imposed by the first data set.

3.2 Large Scale Structure (LSS)

The cosmological Large Scale Structure (LSS) refers to the structure and density distribution of matter on scales larger than individual galaxies or groups of galaxies. Gravity has created and formed these correlated structures, which can be seen up to billions of light years away. On large scales, gravity pulls galaxies and matter into patterns in a similar way that it keeps pulling gas particles together to form stars and stars to form galaxies on smaller scales . These patterns frequently contain large filaments of galaxies and gaps between them, similar to a spider web, and this structure is commonly known as "cosmic web". Large-scale structure research is mostly about studying the impact od gravitational force in the Universe and on cosmic web. Astronomers can estimate the distances of various galaxies from the Earth and the correspondingly times that light was emitted fron these galaxies in the history of Universe based on the required time for light to reach us. This has enabled us to infer that as time has by, gravity has pulled more and more matter into clusters, clustering the Universe even more. LSS provides information about dark energy as well. The majority of theories on dark energy wich explain the late accelerated expansion of teh Universe also suggest that it slows down the process by which gravity produces large structures. This is in some sense intuitive since as the expansion of the Universe continues to accelerate, the matter will need more time to cluster since it must travel a greater distance. Therefore, the evolution of large-scale structures over time provides information about dark energy and gravity and how they change as the Universe evolves over time. Fig. (3.1) shows how gravity is clustering matter from the early Universe (most-left box) to the present-day (most-right box), considering the expansion of the Universe [39].

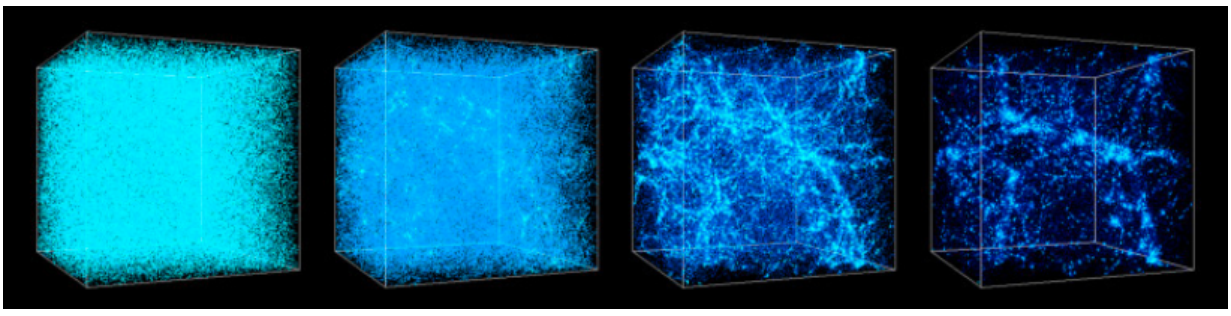

Figure 3.1: The large scale structure. From left to right gravity is increasing and the matter is clustering further and further. The Universe (boxes) is also expanding by passing the time. The simulation adopted from Dark Energy Survey (DES) website.

On reasonably large scales, the Universe is homogeneous and isotropic. Most theories of early universe suggest that the origins of structure in the Universe are quantum mechanical. Due to the random nature of the fluctuations, the Universe appears uniform on large scales but is inhomogeneous and anisotropic on smaller scales. Areas that had higher energy densities or gravitational curvature in the early universe will have over-dense eras, which will produce more galaxies than usual in the late universe. Similar to this, eras in the early Universe with lower energies will correspond to under-dense regions and have fewer galaxies than usual in the late Universe .

Density fluctuations

The over-density can be calculated as

$$\delta(X,t) = \frac{\rho(X,t) - \bar{\rho}}{\bar{\rho}}, \tag{3.13}$$

in which $\rho(X,t)$ is the matter density at time t with space coordinate X and $\bar{\rho}$ is the average density over the whole space. Note that the over-density meets the inequality $-1 < \delta \leq \infty$.
According to standard inflationary theory, primordial matter density perturbations have an initial Gaussian distribution and follow

$$P(\delta)\ d\delta = \frac{1}{\sqrt{2\pi}\sigma}\ e^{-\delta^2/2\sigma^2}\ d\delta. \tag{3.14}$$

It is worthwhile to mention that for small perturbations ($\delta \ll 1$), the distribution is Gaussian while for larger perturbations ($\delta \gg 1$), this assumption breaks down. Tests of so-called non-gaussianity, or deviations from the Gaussian distribution in Eq. (3.14), have become an interesting topic in cosmology in the past decade (for more detail see [39]).

Two point correlation function

- **Point process**
  Assume some point particles in the space and their density to be n. Therefore, the probability of existing a point particle in volume dV can be calculated as

$$dP = n\ dV. \tag{3.15}$$

Now for two particles, assuming a given particle observed in dV_1, the probability of finding the second particle in dV_2 is

$$dP(p_2|p_1) = n(1 + \xi(r_{12}))\ dV_2, \tag{3.16}$$

where the *two point correlation function* [1] for clusters and galaxies can be approximated as

$$\xi(r) = (\frac{r}{r_0})^{\gamma}, \tag{3.17}$$

where $\gamma \approx -1.8$ and $r_0 \approx 20h^{-1}\ Mpc$, $r_0 \approx 5h^{-1}\ Mpc$ for clusters and galaxies respectively. Now assume that we have a particle located at the center of a volume V, the expected number of particles in that volume is

$$\langle N \rangle = nV + n \int \xi(r) dV, \tag{3.18}$$

in which r is the distance from centered particle.
Similarly, one can find the probability of finding three points in three volume spaces dV_1, dV_2, dV_3 using *three point correlation function* ζ_{123} as

$$dP = n^3[1 + \xi(r_{12}) + \xi(r_{13}) + \xi(r_{23}) + \zeta(r_{123})]dV_1\ dV_2\ dV_3. \tag{3.19}$$

- **Continuous process**
  The two-point correlation function for a continuous density field $\rho(X)$ can be defined as

$$\xi(r) = \frac{\langle [\rho(X + r) - \langle \rho \rangle][\rho(X) - \langle \rho \rangle] \rangle}{\langle \rho \rangle^2} = \langle \delta(X + r)\ \delta(X) \rangle_X. \tag{3.20}$$

  By averaging across all X, it could be rewritten as

$$\langle \rho(X + r)\rho(X) \rangle_X = \langle \rho \rangle^2 [1 + \xi(r)]. \tag{3.21}$$

  And three-point correlation function can also be defined as

$$\begin{aligned} \zeta(r, s, |r - s|) &= \frac{\langle [\rho(X + r) - \langle \rho \rangle][\rho(X + s) - \langle \rho \rangle][\rho(X) - \langle \rho \rangle] \rangle_X}{\langle \rho \rangle^3} \\ &= \langle \delta(X + r) + \delta(X + s) + \delta(X) \rangle_X. \end{aligned} \tag{3.22}$$

  which can also be written as

$$\langle\ \rho(X+r)\ \rho(X+s)\ \rho(X)\ \rangle_X = \langle \rho \rangle^3 [1+\xi(r)+\xi(s)+\xi(|r-s|)+\zeta(r, s, |r-s|)]. \tag{3.23}$$

[1] Here ξ only depends on distances (not directions) due to the isotropy assumption.

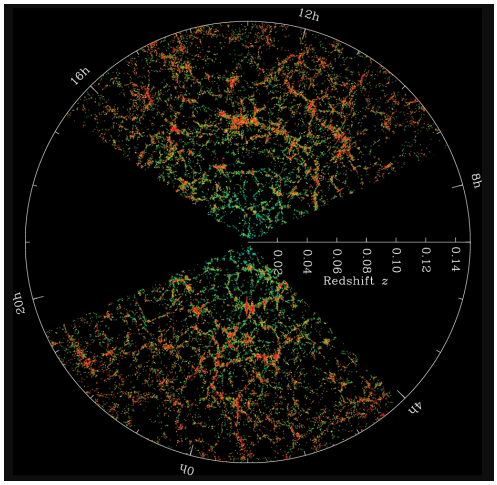

Figure 3.2: galaxies distribution from Baryon Oscillation Sky Survey (BOSS)and we are located at the center of the diagram. The photo is adapted from http://www.sdss3.org/science.

Power spectrum

The density contrast of the Universe—the difference between the local density and the mean density is described as a function of scale by *the matter power spectrum*. It can be calculated from the matter correlation function by the Fourier transform. Therefore, the over-density can be written in Fourier space as

$$\delta(\vec{r}) = \frac{\sqrt{V}}{(2\pi)^3} \int \delta_{\vec{k}}\ e^{-i\vec{k}\vec{r}}\ dk^3, \tag{3.24}$$

where V is the co-moving volume, and the Fourier components can be written as

$$\delta_{\vec{k}} = \frac{\int \delta(\vec{r}) e^{i\vec{k}\vec{r}} d^3r}{\sqrt{V}}. \tag{3.25}$$

Note that $\delta(\vec{r}) \ll 1$, $\delta_{\vec{k}} \ll 1$, by moving from r by Δr the two point correlation function will be as following

$$\langle \delta_{\vec{k}}\ \delta^*_{\vec{k'}} \rangle \rightarrow e^{i(k-k')\Delta\vec{r}} \langle \delta_{\vec{k}}\ \delta^*_{\vec{k'}} \rangle. \tag{3.26}$$

Since homogeneity is assumed, it does not depend on $\Delta\vec{r}$ so Eq. (3.26) comes as

$$\langle \delta_{\vec{k}}\ \delta^*_{\vec{k'}} \rangle = (2\pi)^3 \delta^{(3)}(\vec{k} - \vec{k'}) P(k), \tag{3.27}$$

where k, k' are wave numbers and $P(k)$ (the Fourier transform of the 2-point function) is called the *power spectrum*. In other words, it is the average of the square of the Fourier components over all locations in the Universe, so the power spectrum is the amount of the power on various scales (wave numbers k). Therefore, the power spectrum can be calculated from the correlation function in the following way

$$\begin{aligned} P(\vec{k}) &= \langle \delta_{\vec{k}}\ \delta^*_{-\vec{k}} \rangle = \langle \delta_{\vec{k}}\ \delta_{-\vec{k}} \rangle \\ &= \frac{1}{V} \int \int \langle \delta(\vec{r_1}) \delta(\vec{r_2}) \rangle\ e^{-i\vec{k}(\vec{r_2}-\vec{r_1})}\ d^3\vec{r_1} d^3\vec{r_2} \\ &= \int \xi(r_{12})\ e^{-i\vec{k}\vec{r_{12}}}\ d^3\vec{r_{12}}, \end{aligned} \tag{3.28}$$

where $r_{12} = |\vec{r_1} - \vec{r_2}|$ and we integrated over $\vec{r_2}$ considering $\int d^3\vec{r_2} = V$. Finally, the power spectrum can be calculated as[2]

$$P(k) = \frac{4\pi}{k} \int_0^\infty \xi(r) sin(kr) r\ dr, \tag{3.29}$$

where the inverse-Fourier transform reads from

$$\xi(r) = \frac{1}{2\pi^2 r} \int_0^\infty P(k) sin(kr) k\ dk, \tag{3.30}$$

and

$$\xi(0) = \int_0^\infty \frac{k^3 P(k)}{2\pi^2} d\ lnk, \tag{3.31}$$

logarithmic band power can be also defined as

$$\Delta^2(k) \equiv \frac{k^3 P(k)}{2\pi^2}. \tag{3.32}$$

For more details, see [39].

[2] $P(\vec{k}) = P(k)$

Galaxy Bias

As was demonstrated, the matter density field is a highly effective statistical tool that provides abundant information about the early and late Universe. Unfortunately, we can not directly observe most of the matter density field as it laregely consists of Dark Matter. However, visible tracers of the density field can be employed instead. One of these tracers is galaxies which can be categorized among observable objects, and their distribution follows the distribution of the matter density field. The so called bias parameter characterizes how the galaxy density field (observable field) connects to the underlying matter field. The *density field for galaxies* can be described as

$$\delta_g(x) = \frac{n_g(x)}{\bar{n}_g} - 1, \tag{3.33}$$

in which $\bar{n}_g$ is the average number density and $n_g(x)$ the number density for galaxies at location x. Note that, since the number of galaxies is countable, their density fields are typically expressed as number densities. The density field of galaxies can be defined more generally as [26]

$$\delta_g(x, \tau) = \sum_W b_W(\tau) W(x, \tau) \tag{3.34}$$

where W is a mathematical operator made up of matter density field, and b_W is the bias parameter. Since on large scales, gravity is the controlling mechanism for structure formation, the statistics of galaxies can be expressed locally as a function of over-densities in the matter field. Therefore, for smoothed density field of galaxies, the mentioned equation can be written as [34]

$$\delta_g(x) \approx \sum_0^\infty \frac{b_k(x)}{k!}\ \delta^k(x). \tag{3.35}$$

Note that in the limit of $\delta \ll 1$, one can ignore higher orders of δ so that $b_0 = 0$ and (3.35) can be reduced to

$$\delta_g(x) = b_1(x)\ \delta(x), \tag{3.36}$$

where b_1 is the so-called *linear galaxy bias*. However, In the general case, the Taylor expanded form of (3.35) is more difficult than what is mentioned above. For more information, see [26].

In Fourier space, the linear bias parameter can be obtained by the power spectrum of matter P(k) and galaxies $P_g(k)$ as

$$b_P^2(k) = \frac{P_g(k)}{P(k)}. \tag{3.37}$$

It can also be calculated by two-point correlation function of matter and galaxies as

$$b_\xi(r)^2 = \frac{\xi_g^2(|x-y|)}{\xi^2(|x-y|)} = \frac{\langle \delta_g(x)\ \delta_g(y)\rangle}{\langle \delta(x)\ \delta(y)\rangle}, \tag{3.38}$$

where $\xi_g^2(|x-y|)$ is called *galaxy-galaxy auto- correlation* or 2-point correlation function for galaxies and $\xi^2(|x-y|)$ is the 2-point correlation function for matter.

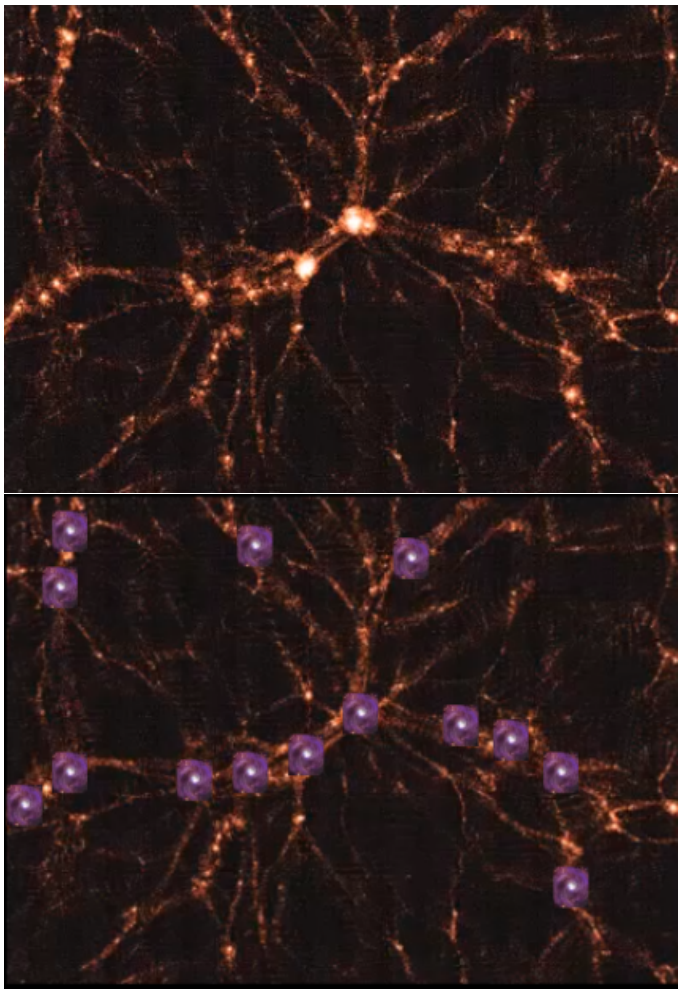

Figure 3.3: Top: observed galaxies (yellow clustered locations) from underlying matter field. Adopted from Illustris simulation website. Bottom: Galaxies which are tracing dark matter. Credit: Amir Hossein Dehghani.

Observational Constraints on Galaxy Bias

As mentioned before, it is believed that the galaxy distribution follows the distribution of underlying dark matter. This has been confirmed both through ΛCDM simulations and observations. Galaxies form in the over-dense areas (halos) that have collapsed due to the their gravity. Recent observations and simulations are now able to provide very good insight on the tracing properties of galaxies and constrain the dependency of the galaxy bias and the power spectra to the astrophysical properties like luminosity, stellar mass and star formation rate and different parameters of models which relate the galaxy field to the dark matter field. As an example, Figure 3.4 shows that the galaxy clustering can be characterized as a function of specific Star Formation Rate (sSFR) [3] and stellar mass ratio [4]. This measurement is done using two different galaxy surveys namely SDSS and PRIMUS and one mock catalog simulated by the evolution model of the universe provided in [16]. It can be seen that in a fixed stellar mass, the two-halo relative bias enhances as the sSFR decreases which means galaxies with sSFR higher than star-forming main sequence (SFMS) are more clustered than galaxies with sSFR lower than SFMS. It can also be seen that for a given value of sSFR ratio, the galaxies with more stellar mass are more clustered. However, bias has more dependency on sSFR than stellar mass. These results show that sSFR and stellar mass can both affect the connection between galaxies and dark matter haloes [18, 23]. This trend can also be seen using VIMOS Public Extragalactic Redshift Survey (VIPERS). As shown in fig 3.5, The bias of galaxies strongly depends on their mass and luminosity. As the figure indicates more massive and luminous galaxies have higher corresponded bias value (more clustered) [48].

[3] Its values corresponds to star formation rate divided by stellar mass.

[4] Here mass ratio refers to the ratio of masses of two galaxy samples.

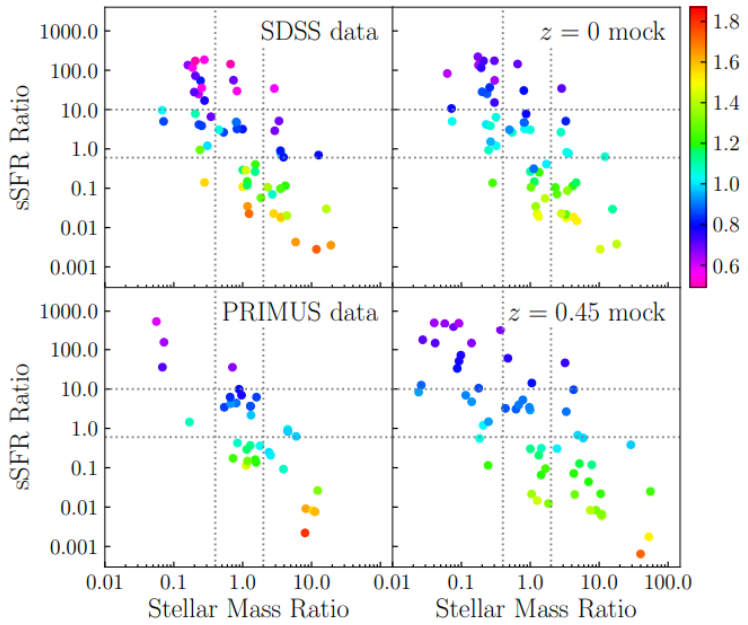

Figure 3.4: Relative bias as a function of stellar mass and sSFR, measured for two SDSS and PRIMUS galaxy surveys and the mock catalog ($z = 0, 0.45$). The dotted lines show the fixed value of stellar mass and sSFR. The color bar is associated to the color of each point corresponded to the bias value. Adopted from [18].

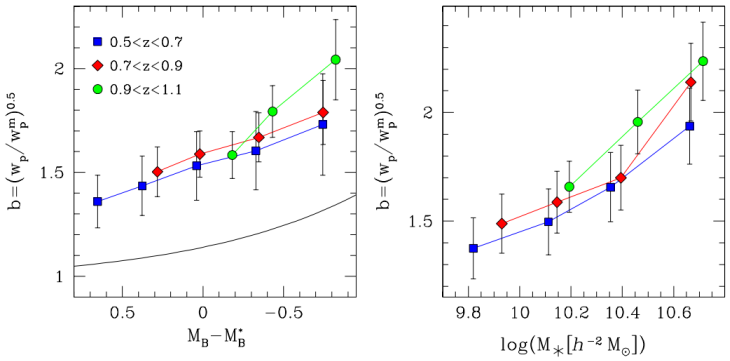

Figure 3.5: Left plot: Bias dependency on luminosity (using B-band absolute magnitude). Solid line is a fit model to bias done by [71]). Right plot: Bias as a function of stellar mass in different redshift bins [48].

Chapter 4

Gravitational Waves from Merging Compact Binaries

In this section, we will discuss gravitational wave theory in linearized gravity, estimating cosmic distance from dark sirens, gravitational wave detectors and finally, some astrophysical prescriptions. The discussion in this section is mostly inspired from references [33, 37, 60, 25, 62, 43, 27, 29, 28, 54, 32, 61, 3].

4.1 Theory of Gravitational Waves (GWs)

Albert Einstein hypothesized gravitational waves as some perturbations in the space-time geometry which are produced by a moving mass and propagate from their source at extremely high velocity (the speed of light).
However, the first indirect evidence for their existance was discovered by astronomers in 1974. They recognized a decrease in the orbit of Hulse-Taylor binary pulsar which matched the theoretical predictions for energy being emitted as gravitational waves. The first direct detection of gravitational waves came almost forty years later in 2015, when the Laser Interferometer Gravitational-Wave Observatory (LIGO) detectors in Livingston, Louisiana, and Hanford, Washington, detected a signal consistent with a gravitational wave form emitted from merging of two stellar black holes [2, 11].

In this section, I will briefly discuss the theory of GWs and, in particular, how the distances can be estimated based on a detected GW signal and then discuss the future generation of GW detectors.

Please note that in this chapter, Latin indices are used for space-time coordinates and the metric is taken as $\eta_{ab} = diag(-1, 1, 1, 1)$.

4.1.1 GWs in Linearized Gravity

In linearized gravity, the spacetime metric, g_{ab}, is assumed to be approximately flat and written as

$$g_{ab} = \eta_{ab} + h_{ab} \quad ; \quad ||h_{ab}|| \ll 1, \tag{4.1}$$

where $\eta_{ab} = diag(-1, 1, 1, 1)$ and h_{ab} represents the metric perturbation which encompasses GWs and non-radiative degrees of freedom. As the name indicates, the higher-order perturbative terms in h_{ab} are ignored in this analysis.
Note that the condition $||h_{ab}|| \ll 1$ is satisfied in weak field regime and underlying flat space-time.
The next step is calculating all the quantities needed to construct the Einstein tensor and, from there, obtaining the dynamics of GWs in linearized gravity.
First, Christoffel coefficients are computed as

$$\Gamma^a_{bc} = \frac{1}{2}(\partial_c h^a_b + \partial_b h^a_c + \partial_d h_{bc}). \tag{4.2}$$

From that Riemann tensor, Ricci tensor and Ricci scalar are obtained,

$$\begin{aligned} R^a_{bcd} &= \partial_c \Gamma^a_{bd} - \partial_d \Gamma^a_{bc} = \frac{1}{2}(\partial_c \partial_b h^a_d + \partial_d \partial^a h_{bc} - \partial_c \partial^a h_{bd} - \partial_d \partial_b h^a_c), \\ R_{ab} &= R^c_{acb} = \frac{1}{2}(\partial_c \partial_b h^c_a + \partial^c \partial_a h_{bc} - \partial_c \partial^c h_{ab} - \partial^b_a h), \\ R &= \partial_c \partial^a h^c_a - \Box h, \end{aligned} \tag{4.3}$$

where h is the trace of h_{ab} and is defined as $h = h^a_a$ and $\partial_c \partial^c = \Box$ is called wave operator. Substituting from these relations, it can be shown that the Einstein tensor reduces to

$$\begin{aligned} G_{ab} &= R_{ab} - \frac{1}{2}\eta_{ab} R \\ &= \frac{1}{2}(\partial_c \partial_b \bar{h}^c_a + \partial^c \partial_a \bar{h}_{bc} - \bar{h}_{ab} - \eta_{ab} \partial_c \partial^d \bar{h}^c_d), \end{aligned} \tag{4.4}$$

where, $\bar{h}_{ab} = h_{ab} - \frac{1}{2}\eta_{ab} h$ is called the trace-reversed perturbation. G_{ab} can be further simplified by fixing the gauge [1] freedom to Lorentz gauge $\partial^a \bar{h}_{ab} = 0$ so that Einstein Eq.

[1] Some theories in physics describe forces in terms of fields, such as the electromagnetic field, the gravitational field, and the fields describing forces between elementary particles. Some fundamental fields

(2.2) reduce to

$$G_{ab} = -\frac{1}{2}\Box\bar{h}_{ab} = -16\pi T_{ab}. \tag{4.5}$$

In the absence of matter and in the case of GWs propagating in empty space-time, the gravitational wave equation becomes homogeneous

$$\Box\bar{h}_{ab} = 0, \tag{4.6}$$

which has plane wave solutions. Therefore solutions can be written as

$$\bar{h}_{ab}(X,t) = Re\int d^3k A_{ab}(K)e^{i(KX-\omega t)}, \tag{4.7}$$

where K is the wave vector, $\omega = |K|$ and $A_{ab}(K)$ are complex coefficients. By substituting (4.7) in the Lorentz gauge condition we get $k^a A_{ab} = 0$ in which $k^a = (\omega, K)$.
These plane waves are called **Gravitational Waves**, which are the metric oscillations substituted into the Einstein Field Equations.
We now focus on the vacuum space-time where $T_{ab} = 0$. In other words, the space in which linearized Einstein equation has homogeneous, asymptotically flat [2] solutions. For having such a space-time, there are two conditions which should be satisfied:

1. Specialising the gauge to make the metric perturbation entirely spatial and traceless as

$$\begin{aligned} h_{ti} = h_{tt} &= 0 \\ h = h^i_i &= 0. \end{aligned} \tag{4.8}$$

2. Then, by implying the Lorentz gauge condition, we will get a transverse spatial perturbation in the metric. Therefore so-called "transverse-traceless gauge" which is a system in co-moving coordinate (meaning that free particles' location and their separation are constant in the coordinate system), can be written as

$$\partial_i h_{ij} = 0. \tag{4.9}$$

Now consider a GW which is propagating in the z-direction, so the solution for the wave Eq. (4.6) comes as

$$h^{TT}_{ij} = h^{TT}_{ij}(t-z), \tag{4.10}$$

cannot be directly measured, although some corresponding quantities, like charges, energies, and velocities, can be. Therefore physicist use gauge transformation to transit from one of these field configurations to another.

[2] A Lorentzian manifold in which the curvature vanishes ($h_{ab} \to 0$) at large distances ($r \to \infty$) resulting in Minkowski spacetime-like geometry at large distances.

then by applying the Lorentz condition for the asymptotically flat space-time, we will get

$$h^{TT}_{zj}(t-z) = 0. \tag{4.11}$$

Therefore, the non-zero components would be $h^{TT}_{xx}, h^{TT}_{xy}, h^{TT}_{yx}, h^{TT}_{yy}$. So by applying (4.8), we get

$$\begin{aligned} h^{TT}_{xx} &= -h^{TT}_{yy} = h_+(t-z) \\ h^{TT}_{xy} &= h^{TT}_{yx} = h_\times(t-z), \end{aligned} \tag{4.12}$$

where $h_+, h_\times$ denote waveforms of the gravitational wave. Hence the metric perturbation can be calculated as follows

$$\bar{h}_{\mu\nu}{}^{3} = h_{\mu\nu} = \begin{pmatrix} 0 & 0 & 0 & 0 \\ 0 & h_+ & h_\times & 0 \\ 0 & h_\times & -h_+ & 0 \\ 0 & 0 & 0 & 0 \end{pmatrix} \tag{4.13}$$

in which $h_+, h_\times$ are polarization components of GW. So by having wave amplitudes

$$h_{ab} = \begin{pmatrix} h_+ & h_\times \\ h_\times & -h_+ \end{pmatrix} \tag{4.14}$$

and choosing $\hat{e}_x, \hat{e}_y$ as the unit basis vectors in the considered plane. Basis tensors and TT gravitational-wave tensors can be defined as

$$\begin{aligned} e_\times &= \hat{e}_x \otimes \hat{e}_y + \hat{e}_y \otimes \hat{e}_x \\ e_+ &= \hat{e}_x \otimes \hat{e}_x - \hat{e}_y \otimes \hat{e}_y \end{aligned} \tag{4.15}$$

$$h = h_+ e_+ + h_\times e_\times.$$

4.1.2 Gravitational Wave Frequency

In order to predict a waveform in the best way, its frequency needs to be well-defined. Frequency is mostly related to the natural frequency for a self-gravitating object and can be written as

$$\omega_0 = \sqrt{\pi G \bar{\rho}} \quad , \quad f_0 = \frac{\omega_0}{2\pi} = \sqrt{G\bar{\rho}/4\pi}, \tag{4.16}$$

in which, $\bar{\rho}$ is the mean density of the mass-energy in the source. Although this is in the Newtonian regime, it is able to predict order-of-magnitude of the natural frequencies and

[3] Note that, $\bar{h}_{\mu\nu} = h_{\mu\nu}$ since we are in TT gauge which is traceless

relativistic systems like black holes.
The mean density can be calculated by the mass and the radius of the body as

$$\bar{\rho} = \frac{3M}{4\pi R^3}. \tag{4.17}$$

So that by considering Eqs. (4.16) and (4.17), the frequency of a radiation emitting by a object with mass M and radius R can be calculated as

$$f_0 = \frac{1}{4\pi}\sqrt{\frac{3M}{R^3}}. \tag{4.18}$$

For instance, in case of having a neutron star of mass $1.4M_\odot$ and radius $10km$, frequency is $f_0 = 1.9\ kHz$, and for a large black hole with mass $2.5 \times 10^6 M_\odot$ it will fall down as $f_0 = 4\ mHz$.
Fig. (4.1) describes the mass-radius diagram for the gravitational wave sources; the 3 plotted lines $f_0 = 10^{-4}Hz, f_0 = 1Hz, f_0 = 10^4 Hz$ characterize the natural frequency. Emitted GWs with frequencies between $f_0 = 1Hz, 10^4 Hz$ can be detected by ground-based detectors while radiation with lower frequencies only can be observed by space-based ones. There is also a black hole line obeying the $R = 2M$ equation, and there is no black hole below that line. It also intersects the two frequency lines meaning that black holes with masses more than 10^4 can not be detected by ground-based detectors. Another drawn line is the chrip line; if a binary locates below this line, its orbit will shrink to the point where its orbital frequency rises noticeably over the course of a year. The dashed-line also represents the 1-year coalescence line, where the timescale of the orbital shrinking (caused by gravitational radiation back reaction) is less than one year.

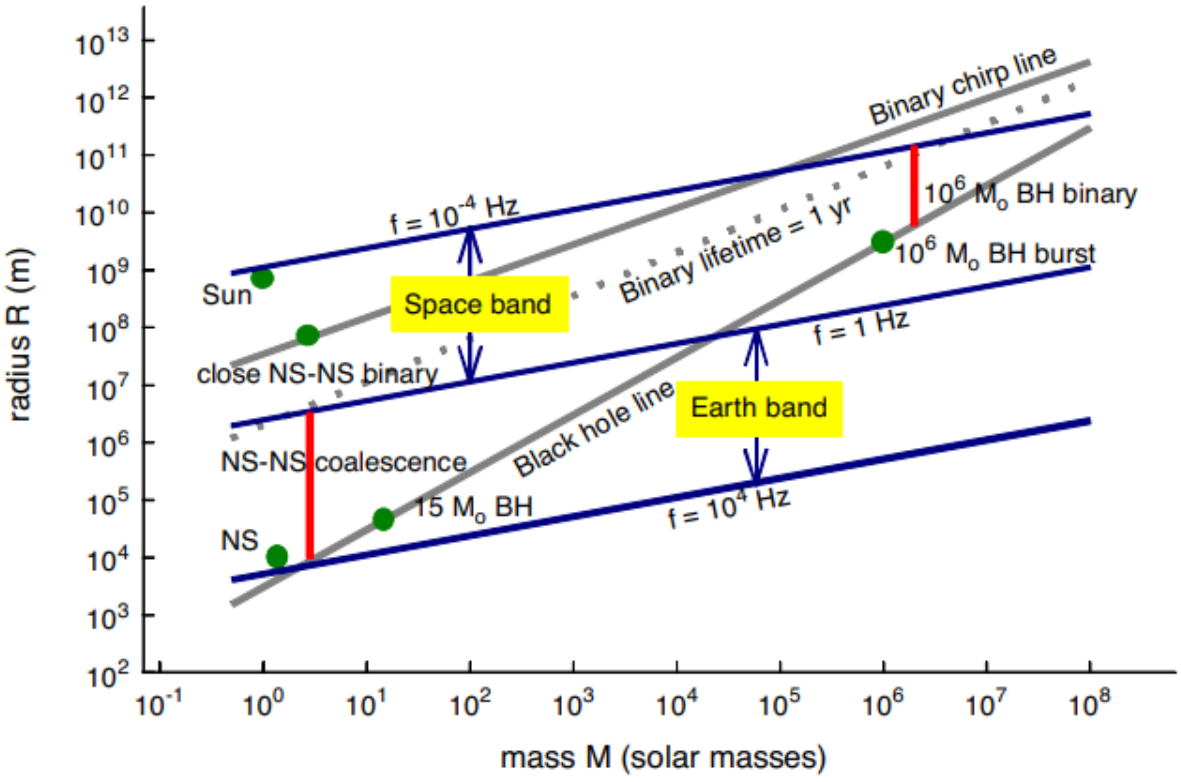

Figure 4.1: Mass-radius diagram for GW sources, the vertical and horizontal axis are the size and the mass of the GW sources. The frequency lines obey $f \sim \sqrt{\frac{G\rho}{4\pi}}$ [60].

4.1.3 Cosmic Distance Estimation by Dark Sirens

On September 14, 2015, the first observation of gravitational waves opened a new window in astronomy. When the Laser Interferometer Gravitational-Wave Observatory (LIGO) detectors detected gravitational waves emitted by a pair of merging black holes labelled GW150914. The discovery was also a victory for theory. The GW's frequency and amplitude evolution precisely matched the general relativity predictions.
In Fig. (4.2) , one can see how the strain [4] of the GW (emitted by GW150914) changes by time and the relation between frequency and amplitude with time according to Hanford data [25].

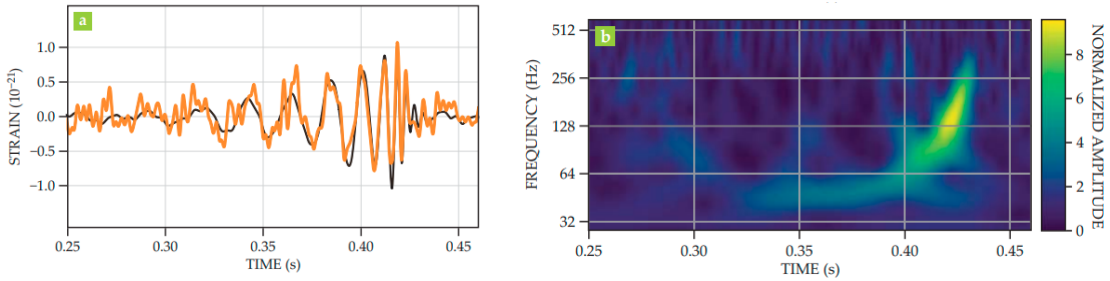

Figure 4.2: a: Strain of the data from LIGO (orange) and the black curve is a GR theoretical fit (from Hanford data).b: the relation between frequency and time achieved by Hanford data [25].

After a short while, more BBH and BNS [5] coalescence were detected. Still, due to the insufficient electromagnetic and matter fields near the merging eras, non of them had an electromagnetic counterpart. These detections were followed by the most important detection (labelled GW170817) in the history of astronomy happened on 17 August 2017; astronomers detected a gravitational-wave signal (detected by LIGO and Virgo) after about 1 second of observing a burst of gamma rays (by Fermi Gamma-Ray Space Telescope and INTEGRAL observatory) from a kilonova explosion in the NGC 4993 galaxy which was 1000 times brighter than a normal kilonova. So that the electromagnetic wave and gravitational wave emitted by GW170817 helped astronomers measure the Hubble constant and the Universe's dynamic (since distances can be encoded by GWs) via the standard

[4] The oscillation of the LIGO detectors divided by their arm length
[5] Binary of Back holes or Neutron stars

sirens method. Fig. (4.3) shows GW170817 event which was detected due to the merger of two neutron stars.

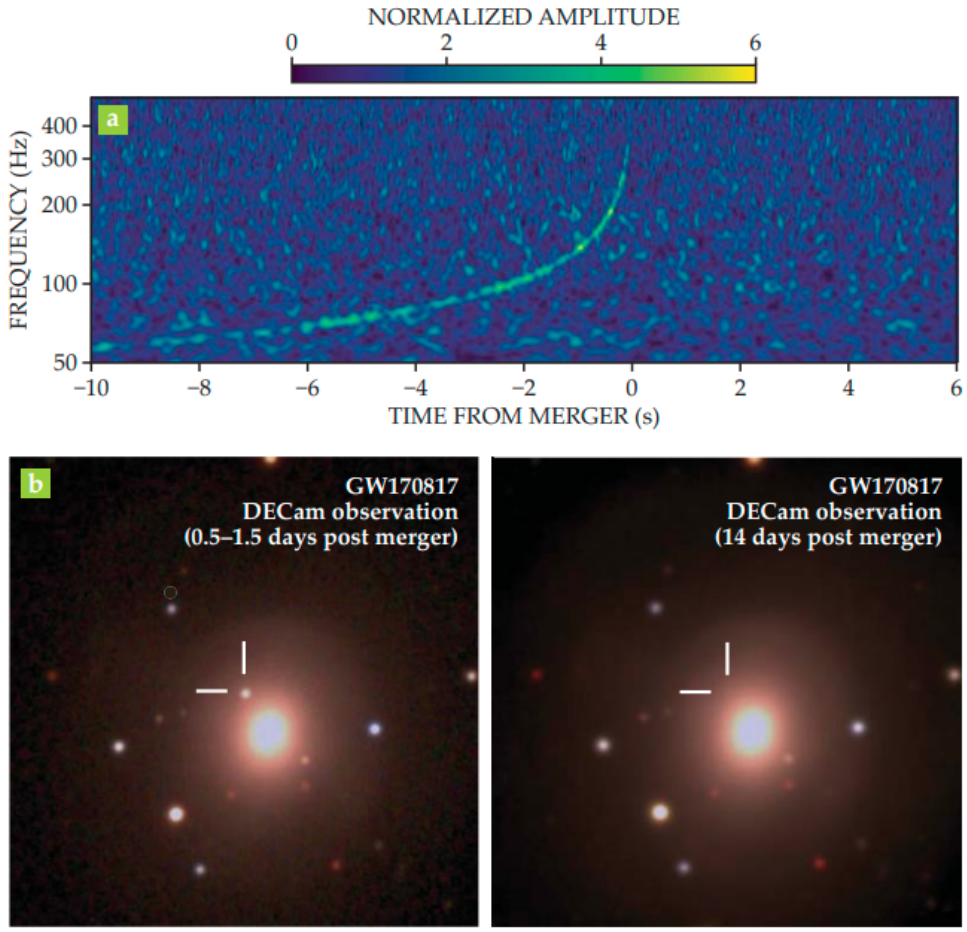

Figure 4.3: a: The frequency of GW is increased by time detected by LIGO. b: The Dark Energy Camera (DECam) also observed electromagnetic counterpart by short time after the merger. By two [62].

Consider a binary neutron star or black hole orbiting in a circular path, the two objects in this orbit is circling with frequency Ω which depends on their masses and their separation in the binary. When GW emits, it takes energy from the orbit, and the orbital separation decreases consequently, followed by an increase in the orbital frequency which causes more energy loss and a further decrease in separation and so forth. Finally, the binary merges and one can observe an outstanding increase rate in the frequency. The relation between frequency and so-called **Chirp mass** $\mathcal{M}$ is

$$\frac{d\Omega}{dt} = \frac{96}{5} \left(\frac{G\mathcal{M}}{c^3}\right)^{5/3} \Omega^{11/3}, \tag{4.19}$$

in which $\mathcal{M}$ can be calculated as

$$\mathcal{M} = \frac{(m_1 m_2)^{3/5}}{(m_1 + m_2)^{1/5}}, \tag{4.20}$$

where m_1, m_2 are the masses of two black holes or neutron stars in the binary.
Let's assume the angle between our line of sight and the normal to the orbital plane is l so that if $l = 0$, the orbital plane is observed head on and for $l = 90°$ corresponds to the case, we are viewing the plane from the edge side. There are two polarization states for gravitational waves, using the convention that the normal to the orbital plane lies in the xz-plane. Their amplitude can be written as

$$\begin{aligned} h_+ &= \frac{2c}{d_L} \left(\frac{G\mathcal{M}}{c^3}\right)^{5/3} \Omega^{2/3} \left(1 + cos^2 l\right) cos2\Phi(t) \\ h_\times &= \frac{4c}{d_L} \left(\frac{G\mathcal{M}}{c^3}\right)^{5/3} \Omega^{2/3} cosl \; sin2\Phi(t). \end{aligned} \tag{4.21}$$

Where $\Phi(t)$ characterizes the accumulated orbital phase, which can be calculated found by integrating Ω over time, and the factor of 2 (multiplied by $\Phi(t)$) corresponds to the quadrupolar nature of waves. Furthermore, d_L is the luminosity distance, G [6] the so-called gravitational constant, $cosl$ is the degeneracy.
From Gravitational wave observations, the Chrip mass (M) can be precisely determined, and in the case of measuring both polarization, one can get l. Finally, by having $\mathcal{M}$, l and according to the equations (4.21) distance to the source (the binary which was the host for the detected gravitational wave) can be estimated.

[6] G = 6.674×1011 m^3 kg^{-1} s^{-2}

4.1.4 Gravitational Wave Detectors

Observing gravitational wave signals can reveal new insight in the most energetic and violent astrophysical incidents like the Universe's black holes and neutron star mergers. As mentioned previously, the first gravitational wave detection has been observed in September 2015 (100 years after Albert Einstein predicted their presence) which was an outstanding scientific discovery in astronomy of the 21 st century. The mentioned gravitational wave had been emitted by the merging of two black holes at a distance of 1.3 billion light years from earth and was detected by LIGO and Virgo gravitational wave detectors [38].

- **Advanced LIGO and Virgo detectors** Have been run since 2015 and 2017, respectively. As shown in Fig. (4.4), they have been run in 3-time intervals, which the third one lasted for about 1 year. Even at design sensitivity, LIGO and Virgo detectors are limited to local Universe, detecting 50 sources per year, mostly black hole mergers.

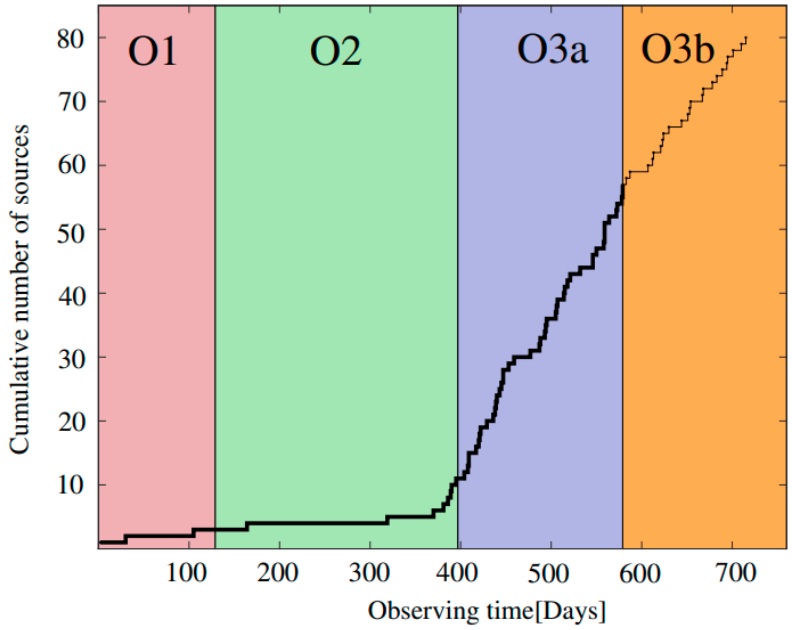

Figure 4.4: adapted from LVC public document G1901322 (see [69]).

- **LIGO A+** Is an incremental upgrade to aLIGO which will be installed in early 2022 and possibly start observing in late 2022. Its coating thermal noise is a factor of 2

lower than the reported measurement by aLIGO. As shown in Fig. (4.5), the A+ range is 1.9 times higher than the achieved LIGO operating at design sensitivity and can be a stepping stone to third-generation detectors technology [45, 56].

- **LIGO India**

  Three gravitational waves (GW) detectors are used in the Laser Interferometer Gravitational-wave Observatory (LIGO) project. Two are in the northwestern American state of Washington at Hanford, and one is in the south-eastern state of Louisiana at Livingston. These observatories are currently being upgraded to their sophisticated configurations (called Advanced LIGO). LIGO-India project proposed to transport one detector from Hanford to India. The proposed detector will be a Michelson Interferometer with Fabry-Perot-enhanced arms of 4 km length with the objective of detecting differential arm-length changes as small as 10-23 Hz-1/2 in the frequency range of 30 to 800 Hz. The design would be the same as the Advanced LIGO detectors that are currently being put into service in the USA [6].

- **KAGRA**

  The Kamioka Gravitational Wave Detector (KAGRA) is another interferometer designed to detect gravitational waves, neutrino and dark matter. The KAGRA detector is made of two three-kilometre-long arms situated underground at the Kamioka Observatory, located near the Kamioka neighbourhood of Hida, Gifu Prefecture, Japan.

- **Third-generation (3G) detectors**

  The third generation of the detectors is supposed to be a network between Einstein Telescope and Cosmic Explorer. It is expected that we will be able to get a strain sensitivity 10 times better than advanced LIGO detectors and detect black hole mergers at the large redshifts, getting a higher signal-to-noise ratio and finally observe more sources per year. The operation time is assumed to be in late of 2030.

- **Einstein telescope**
  Is a ground-based gravitational wave detector with a triangular shape and an arm length of about 10 km. It is supposed to be installed underground to properly detect gravitational waves with low frequency (Hz) (see [69]).

- **The cosmic explorer**
  Is another ground-base gravitational wave detector which will be placed on the ground to help with detecting high-frequency (kHz) or medium-frequency (100 Hz) sources.

Considering the network of Einstein Telescope and Cosmic Explorer will improve gravitational wave detection (see [69]).

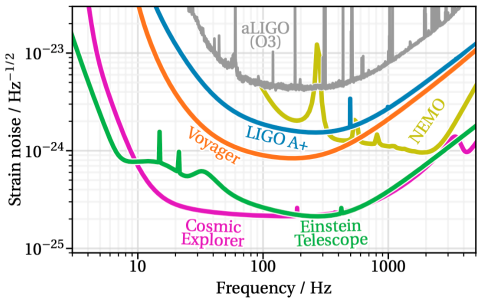

Figure 4.5: The amplitude spectrum of the detector noise as a function of frequency. Adopted from cosmic explorer website (https://cosmicexplorer.org/)

4.2 Astrophysics and Compact Objects

Neutron stars and black holes are created by either collapse of an evolved star or collapse of the white dwarf's core. In either scenario, if they end up having a non-spherical collapse, the binding energy can increase and cause emittion of gravitational waves which carry some portion of the angular momentum and binding energy. This can result in gamma-ray bursts and supernova occurrences rating between 0.01 and 0.1 per year in a Milky way equivalent galaxy (MWEG) and about 30 events per year in Virgo super-cluster. It is worth noting while the focus of this thesis is on detection of gravitational radiations from binary black holes, the detection of GWs from these events can also reveal important information about the dynamics of astronomical systems. In the following, we will discuss the life cycle of a star, supernovae formation, black hole and neutron star binaries.

4.2.1 Life Cycle of a Star

Fig. (4.6) provides a schematics summery of the life cycle of a star. It starts from enormous gas and dust clouds. The existing hydrogen fuels the nuclear reactions in the core of the star and causes the star's brightness during its life-time. Eventually, hydrogen in the core burns out and the star gets to the end of its life. Massive stars run out of fuel more quickly than smaller stars and that is why their life-time are shorter. In the next phase, star can either cool and cease to emit light or it will have a much more violent and energetic demise, exploding as a supernova, dispersing its progenitor's material into the interstellar medium and leaving a dense neutron star or black hole behind [5].

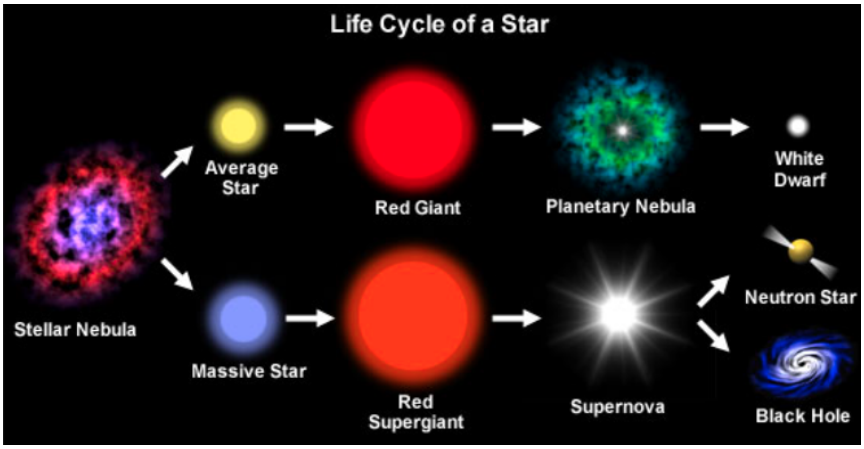

Figure 4.6: The lifetime of a star. Credit: NASA

4.2.2 Supernova and Failed Supernova

Supernova is a luminous star explosion that occurs at the end of the star's lifetime. The progenitor of the massive star may either experience a gravitational collapse or explode and then disappeared into Inter-Stellar Medium (ISM).
In fact, in an arbitrary star nuclear fusion pressure pushes the envelope outward, and gravity pulls it inward, equality of these two forces keeps the star in a stable state. At the end of the star's life-time, gravity takes over, and the star collapses into either a black hole or a neutron star (depending on the mass of the progenitor). It explodes and releases a huge amount of energy (about 10^{51} erg, the amount of energy that a star emits in its whole lifetime) which blows stellar material with the speed of about v = 30000 km/s (0.1c)[7], this derives a shock wave into surrounding ISM and sweeps up supernova remnants (gas and dust) which can be ended up to form new stars.
The collapse triggers a powerful explosion of the outer layers. It appears as a supernova or in another scenario the released gravitational energy can be deficient, and the star collapses into a neutron star or black hole with little radiation energy. Stars with compact cores fail to revive the shock wave propagated from the core, resulting in a failed supernova and eventually black hole formation. Even if the bounce shock can not propagate, a small amount of mass will be ejected due to core collapse, the gravitational mass of the core will decrease by 10 % in a few time intervals (due to the neutrino emission). This sudden loss of gravity will generate a sound pulse as a shock which propagates toward the star's surface and causes an ejection of the outer layer of star's envelope. envelope. The ejecta's mass, kinetic energy and velocity depend on the progenitor types. For instance, Red super-giant stars (RSGs) have feeble envelopes, which leads to a considerable amount of ejection but with small velocity. The Wolf-Rayet stars (WRs) have compressed envelope leading to lighter amount of ejecta with more velocity and Blue super-giant stars (BSGs) lie in between. For more see table (4.1) [31, 66, 40].

Table 4.1: Mass, kinetic energy and velocity ($\sqrt{\frac{2E_{ej}}{M_{ej}}}$) of ejecta for different type of super-massive stars. adapted from Ref.[66]

Model	$M_{ej}[M_\odot]$	$E_{ej}[erg]$	$_{eg}[kms^{-}1]$
RSG	4	2×10^{47}	70
BSG-1	0.1	6×10^{47}	800
BSG-2	0.05	2×10^{47}	630
WR	5×10^{-4}	3×10^{46}	2000

[7] c=299 792 458 m/s is the speed of the light

There are three phases in the model of the supernova remnants:
The first phase is called **Free expansion phase** in which shock evolved into Interstellar Medium (ISM) like a shell until the mass density on the both sides of the shell will be equal. In this state the star enters into the next phase named **Sedov - Taylor phase** in which the mass of the swept-up ISM (on the outer side of the star's shell) is equal to the ejected stellar mass (on the inner side of star's shell) then the star will enter to **cooling phase** in which ions get their electrons back, the thermal pressure decrease, expansion slows down and supernova remnants mixed into interstellar medium and SNR is no longer visible (see Fig. (4.7)). Fig. (4.8) shows the evolution of the shock for BSG-1 model. The shock evolves and until 10^3 years and then stops and cools down. Collision of the ejecta with Circumstellar Medium (CSM) triggers emission (analogous to supernova remnants (SNR)) created by shock-heated gas which helps us to improve detectability.

Figure 4.7: Supernova explosion. Credit: NASA,ESA and hubble heritage

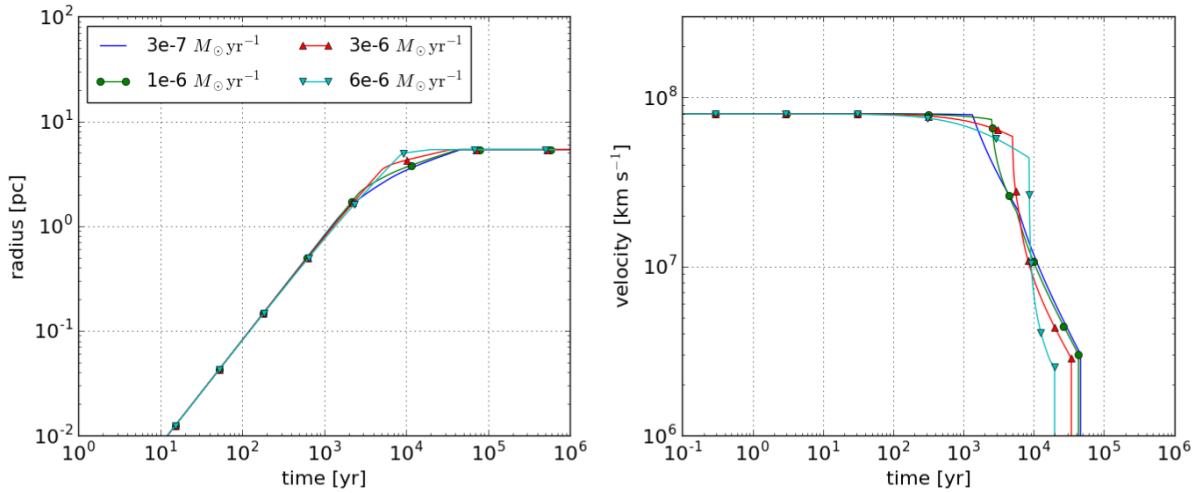

Figure 4.8: the radius and velocity of the shock for BSG-1 model for different rate of mass [66].

4.2.3 Black Hole in Astrophysics

Astronomers now acknowledge that the Universe contains a large number of black holes. There are three different classes of black holes depending on their masses [60].

- **Stellar black-holes**
  Mostly have masses about $10M_\odot$ and are formed by the gravitational collapsing of large red giant stars into their centers and occur supernova explosions. Stellar black hole radiation will fall within the frequency range detectable by ground-based detectors (see Fig. (4.1)). Even though black holes (BH) are formed less frequently than neutron stars (NS), the number of binary systems containing black holes and neutron stars, or two black holes, is greater than that of neutron-star binaries since neutron star binaries are much more easily fragmented in comparison with black hole ones. In most cases, When a NS forms, it will lose a portion of its progenitor's mass, and now the companion star (which is rotating with the same speed as before) is holding in the binary with fewer amount of gravitational attraction finally, the binary will be broken. Whereas, in the case of forming black hole, the majority of the original mass may fall into the hole, increasing the binary's chance of survival. Therefore, in the case of having a similar population of NS binaries and black-hole

binaries in the Universe, one can detect NS coalescence much more frequently rather than black-hole ones and the detection can also be done by first-generation detectors.

- **Intermediate-mass black holes**
  The mass of the intermediate-mass black holes lies between $100M_{\odot}$ and $10^4 M_{\odot}$. Due to their weaker influence on nearby stellar motions, they can not be identified.

- **Supermassive black holes**
  These black holes have masses between $10^6 M_{\odot}$ and $10^{10}.M_{\odot}$ and usually located in the center of most galaxies (which at least are sufficiently near to ours to study) resulting in having large population number. Gravitational radiation from supermassive black holes coalescence is much more powerful than discussed black holes, the amplitude is higher, but the frequency is lower ($\propto 1/M$, where M is the mass of black holes). These galactic black holes can only be detected by detectors located in space (see Fig. (4.1)).

4.2.4 Neutron Stars in Astrophysics

The collapsed core of a supergiant star with a total mass of between 10 and 25 solar mass (or more if the star was particularly metal-rich) is what we refer to as a neutron star. They known as one of the Universe's smallest and densest classes of stellar objects. When two neutron stars collide, they will exceed the Tolman-Oppenheimer-Volkoff limit [8] of $\sim 2.3\ M_{\odot}$ and will collapse into a black hole and emit gravitational waves. The nuclear matter becomes so heated by the collision that, at least initially, thermal pressure rises to a critical level. The merger radiation can be predicted by numerical simulations using theoretical equations of state, and the equation of the state's underlying nuclear physics assumptions should also be tested by observation. Comparing predicted waveforms with what was observed could give some additional context to the equation of state [60].

4.2.5 Metallicity

Hydrogen and helium comprise the majority of regular physical matter in the Universe and metallicity refers to enormous amount of elements which are heavier than hydrogen

[8] The Tolman–Oppenheimer–Volkoff limit (or TOV limit) is an upper bound for the mass of cold neutron stars which are not rotating, known by Chandrasekhar limit for white dwarf stars. If the mass of the star gets to the mentioned limit, it will collapse to a denser form of it such as a black hole [20].

and helium in an astrophysical object. The majority of the elements (metals) in the Universe heavier than hydrogen and helium are created in the cores of stars as they grow. The metals are gradually deposited into the environment by stellar winds and supernovae, enriching the interstellar medium and supplying resources for forming new stars. As a result, older stars which formed in the early Universe, less-metal-rich Universe typically have lower metallicities than younger stars that formed in the more-metal-rich Universe (late Universe). Therefore astrophysically, stars and nebulae with considerably large amount of heavier elements are referred to as metal-rich, and the ones with a lower amount of metals are called metal-poor stars.

Chapter 5

Modeling Bias Parameter for Binary Black Hole Mergers as Tracers of Galaxies based on Astrophysical Properties

As mentioned in the last chapter, the discovery of gravitational waves by the LIGO-Virgo-KAGRA (LVK) scientific collaboration has provided an opportunity to astronomers for exploring the cosmos through the physics of coalescence of the compact objects like binary systems of black holes (BBH), neutron stars (BNS) and neutron star-black hole (NSBH). The GW measurements can provide new insight into answering questions such as: how the merger rate evolved over cosmic time and how binary compact objects were populated in galaxies. The study of GW sources can also shed light into the formation of binary compact objects and how it relates to different astrophysical properties of their host galaxies such as cosmic star formation rate (SFR), stellar mass, and metallicity. While the current observation of GWs due to the large sky localization errors have not yet provided a meaningful connection between stellar properties and the population of various GW compact objects, several numbers of population synthesis simulations [42] in this regard are forecasting a promising future for the next generation of GWs observations.

In the project described in this chapter, we set out to investigate how specific astrophysical models impact the population of GW sources as tracers of galaxy populations. In particular, we will focus on BBHs and model the dependence of angular and 3-dimensional power spectra for BBH GWs to the parameters in two observed galaxy surveys: GLADE+

and Sloan Digital Sky Survey Data (SDSS) Release 7 catalogs [24, 19]. In doing so we have also developed a numerical package that can easily be adopted to other galaxy surveys (photometric or spectroscopic) and accommodate different astrophysical assumptions. We are planning to make our code publicly available to scientific community in near future.

The following sections describe our theoretical prediction of the GW bias parameter for different choices of galaxy properties. In section (5.1), we will provide a theoretical scheme to compute the BBH merger rate and then demonstrate how it can be used to evaluate the expected number of mergers in various redshift bins for a galaxy catalog such as GLADE+. In section (5.2), we obtain mass distribution of black holes in BBH mergers based on different astrophysical features such as metallicity and SFR distribution for galaxies. Section (5.3), provides a prescription for modeling the probability of each galaxy being the host of a merger event, considering the astrophysical features. Eventually, in section (5.4), we will calculate the power spectrum for galaxies and sirens and evaluate the bias parameter. The description of the two catalogs GLADE+ and SDSS DR7 that we have used in our work, is written in Appendix (A).

5.1 Expected number of Gravitational Wave Event Detections for a Galaxy Catalog

The current models of astrophysics predict that the merger rate of gravitational wave sources depends on different astrophysical properties such as redshift distance, Star Formation Rate (SFR) and delay time distribution (characterizing the time between the formation of stars and the merging of compact objects). In this section we describe a theoretical scheme to calculate the BBH merger rate and then based on that forecast the expected number of GW event sources in different redshift bins corresponding to a galaxy survey.

5.1.1 Binary Merger Rate

We model the dependence of the merger rate to astrophysics quantities as [51, 50]

$$R_{\rm GW}(z_m) = \mathcal{A}_0 \int_{z_m}^{\infty} P(t_d) \frac{dt_f}{dz_f} R_{\rm SFR}(z_f)\ dz_f, \tag{5.1}$$

where z_m, z_f denote the merger and formation redshift, respectively. In the following, we explain what each quantity corresponds to.
$R_{\rm SFR}(z_f)$ represents the redshift-dependent star formation rate (SFR) density for which, the analytically best-fit formula to observation can be written as [51, 50]

$$R_{\rm SFR}(z) = \psi(z) = 0.015 \frac{(1+z)^{2.7}}{1+[(1+z)/2.9]^{5.6}} M_\odot\ {\rm yr}^{-1}\ {\rm Mpc}^{-3}. \tag{5.2}$$

This Fig. (5.1) displays the agreement of the above formula to the observational data. It has a growing phase, is peaked at $z = 1.9$ (approximately $3.5 Gyr$ after the Big Bang) and then decays exponentially in later epochs until present day and the trend seems to be steady for higher redshifts as well [47].

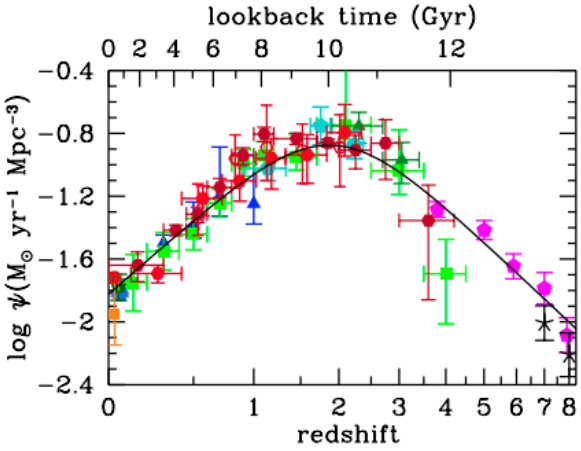

Figure 5.1: Star Formation Rate (SFR) from observational data. Image is adopted from Ref. [47]. For more information on which observation each color corresponds to, see Table 1 the reference [47].

Next, $\mathcal{A}_0$ in Eq.(5.1) denotes the normalization factor such that the local merger rate of gravitational wave sources at redshift $z_m = 0$ matches the observed value $\mathcal{R}_{\rm BBH} = 23.9^{+14.3}_{-8.6}$ Gpc^{-3} yr^{-1} ([12]). This implies

$$\mathcal{A}_0 = \frac{R_{BBH}}{\int_0^\infty P(t_d)\frac{dt_f}{dz_f}R_{\rm SFR}(z_f)\ dz_f}.$$

$t_d = t_m - t_f$ in Eq.(5.1) characterizes the delay time between the star formation time, t_f, and the black holes merger times, t_m. $P(t_d)$ quantifies the delay time distribution. While there are numerous theoretical studies in this regard, the exact distribution of the delay-time and the corresponding value of minimum delay time ($t_{d,min}$) is not well established. Therefore, delay time distribution can be written to be of the form (see Ref. [47] for more details)

$$P(t_d) \propto \Theta(t_d - t_{d,\rm min})t_d^{-\kappa}, \tag{5.3}$$

where $\Theta(t)$ is the Heaviside function. For $t_d < t_{d,min}$, the probability distribution will be equal to zero, and as t_d crossed $t_{d,min}$ and mixture of black holes from the stars formed at z_f will contribute to the merger redshift z_m. κ is one of the free parameters of the model that for now, we set to $\kappa = 1$. In this case, we can easily normalize the probability density

$P(t_d)$ which leads to

$$P(t_d) = \frac{1}{\ln(t_{d,\max}/t_{d,\min})}\Theta(t_d - t_{d,\min})t_d^{-1}, \tag{5.4}$$

where $t_{d,\max}$ is the maximum possible delayed time, taken to be sufficiently large and in the order of the age of the Universe in our models. Fig. ((5.2)) shows examples of the delay time distributions considering three different values of $t_{d,\min}$. Note that mentioned measurements on $\kappa, t_{d,min}$ are based on stochastic GW background and individual events and can be measured more precisely in future [47].
Finally, dt_f/dz in Eq. (5.1) is the standard change-of-coordinates Jacobian (relating time to redshift) for which we must invoke the usual cosmological equations. We write the lookback time to the formation as

$$t_f = \frac{1}{H_0}\int_0^{z_f} \frac{dz}{(1+z)E(z)}, \tag{5.5}$$

where H_0 is the Hubble constant and

$$E(z) = \sqrt{\Omega_{m0}(1+z)^3 + \Omega_{r0}(1+z)^4 + \Omega_\Lambda + \Omega_K(1+z)^2}. \tag{5.6}$$

So the Jacobian terms is given by

$$\frac{dt_f}{dz_f} = \frac{1}{H_0}\frac{1}{(1+z_f)E(z_f)}. \tag{5.7}$$

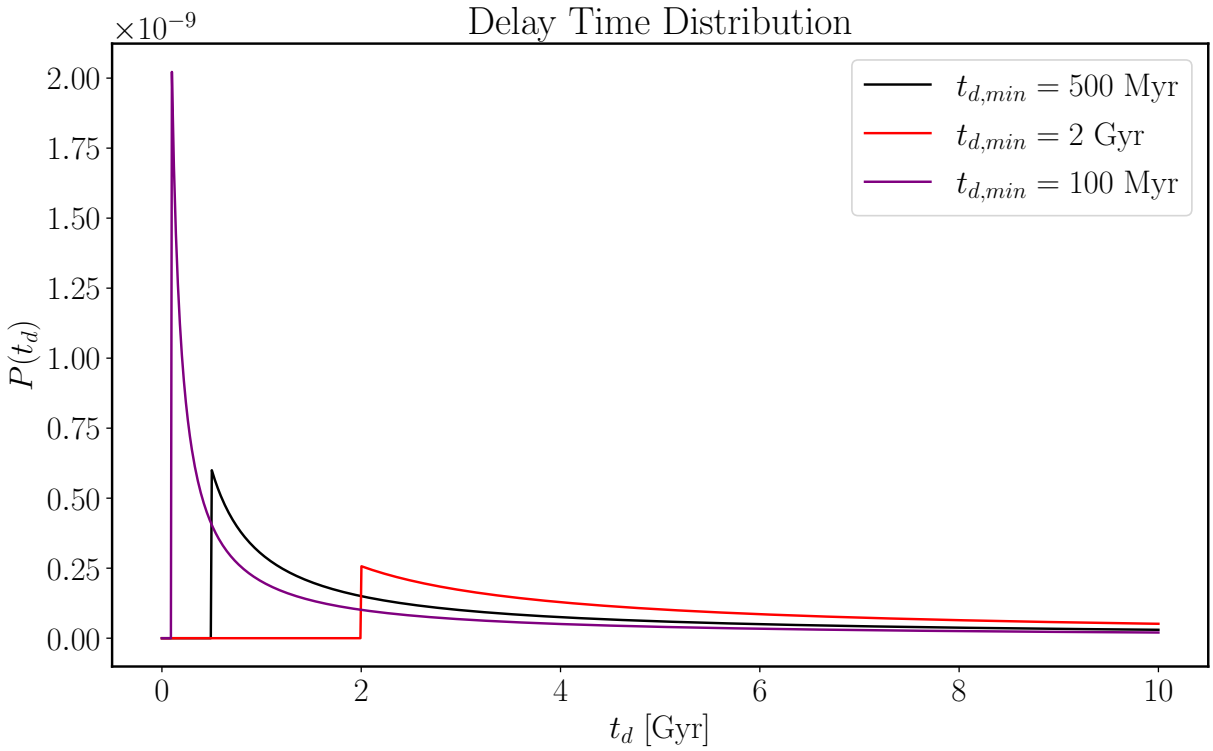

Figure 5.2: Dependence of delay time distribution for three different values of minimum delay-times, $t_{d,min}$, assuming power law decay with $\kappa = 1$.

In what follows, we will choose our fiducial cosmology to have vanishing curvature and radiation density parameters (i.e. $\Omega_K,\ \Omega_r \simeq 0$) along with $\Omega_m = 0.3$, $\Omega_\Lambda = 0.7$, and $H_0 = 70$ km/s Mpc. Substituting these values and functions back in Eq. (5.1), we can calculate the merger rate $R_{\rm GW}$ for different values of $t_{d,\rm min}$.
Fig. ((5.3)) displays merger rate calculation for different minimum delay times and different values of κ. It can be seen that as expected by increasing $t_{d,min}$, on average merger events take longer to occur, and the peaks of merger rates are moving to the lower redshifts.

Fig. ((5.4)) shows the sampled merger rate considering different delay-time which have been fit by the merger rate curve and Kernel density estimation (KDE) for the sampled merger rates. One can see an agreement between our sampling scheme based on the merger rate function normalised as pdf and our KDE estimation from sample.

Top figure in Fig. ((5.4)) shows sampling from merger rate in Eq. (5.1) normalized to a pdf with $t_{d,min} = \{100Myr,\ 500Myr,\ 5Gyr\}$ and $\kappa = 1$. Smooth lines correspond to the

underlying pdf for specific $t_{d,min}$. Bottom figure: Kernel density estimation (KDE) for the sampled merger rates in the top figure.

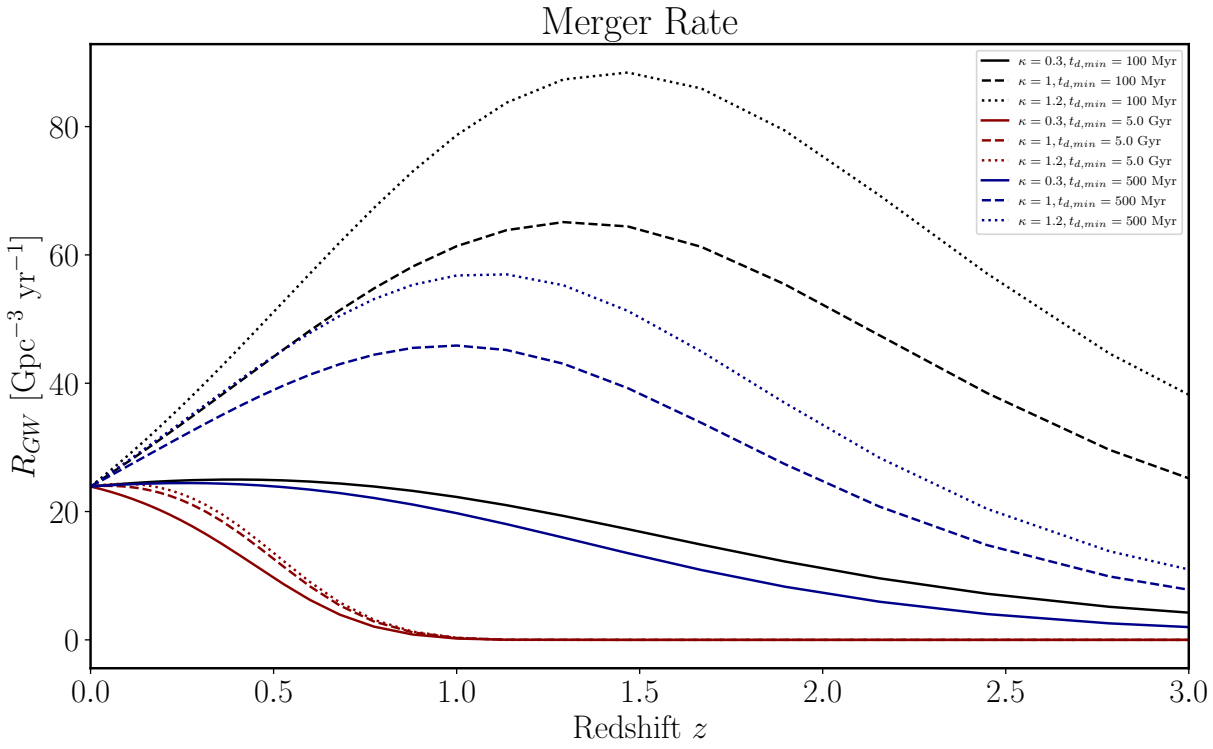

Figure 5.3: Merger rate $R_{\rm GW}(z)$ for three different minimum delay times $t_{d,\rm min} = \{100\ \text{Myr}, 500\ \text{Myr}, 5\ \text{Gyr}\}$. The red curve corresponds to the 5 Gyr minimum delay time, the black curve is the 100 Myr minimum delay time, and the blue curve is the 500 Myr minimum delay time. Different line styles correspond to different power law index κ. Note that these curves have been normalized so that they coincide at redshift $z = 0$ and $\mathcal{R}_{\rm BBH} = 23.9^{+14.3}_{-8.6}$.

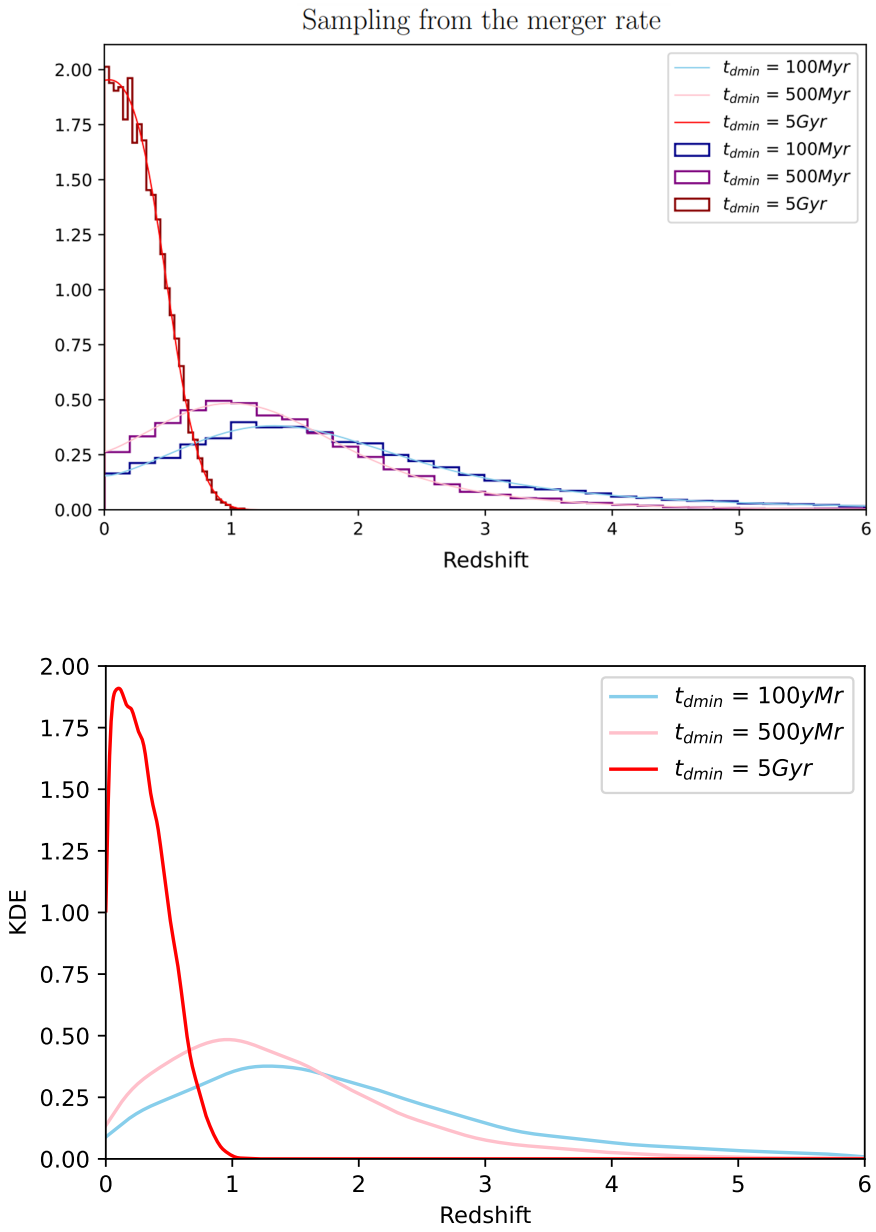

Figure 5.4: Top figure: sampling from merger rate in Eq. (5.1) normalized to a pdf with $t_{d,min} = \{100Myr, 500Myr, 5Gyr\}$ and $\kappa = 1$. Smooth lines are merger rates for specific $t_{d,min}$. Bottom figure: Kernel density estimation (KDE) for the sampled merger rates in the top figure.

5.1.2 Computing the Expected Number of Merger Events in Different Redshift Bins

To compute the number of mergers in each redshift bin, we can write

$$N_{GW}(z_a) = \int_{z_a-\Delta z/2}^{z_a+\Delta z/2} \frac{dV}{dz} \frac{R_{GW}(z)}{1+z} T_{\rm obs}\ dz, \tag{5.8}$$

where z_a is the midpoint of bins labeled as $a = 1, \cdots, N_{\rm bins}$, $N_{\rm bins}$ is the number of bins in redshift range of the galaxy survey, $[0, z_{\rm max}]$. Width of each redshift bin is taken as $\Delta z = z_{\rm max}/N_{\rm bins}$. $T_{\rm obs}$ is a constant value corresponding to the observation time and depends on the running time of the GW detectors. The following is an example of using this analytical framework to forecast the number of GW events for corresponding to a galaxy survey.

The Expected Number of Merger Events in Redshift Bins Corresponding to GLADE+ Catalog

As an example we estimate the number of merger events for the redshift depth of GLADE+ Catalog $[0, z_{\rm max}] = [0, 0.3]$. Table (5.1) and Fig.((5.5)) illustrate the computed number of mergers using Eq.(5.8) and dividing the redshift range into 6 bins ($\Delta z = 0.05$), assuming the observing time of $T_{\rm obs} = 1$. Fig. ((5.6)) displays how the host galaxies would be distributed in a HEALPix map, if sirens were sampled from the catalog using a uniform angular distribution.

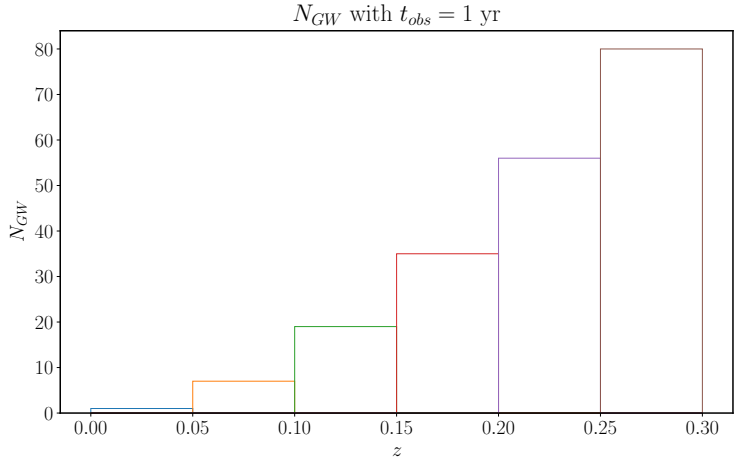

Figure 5.5: Number of GW mergers, N_{GW}, with the observation time of $T_{\rm obs} = 1$ yr. The other paramaters are set as $\kappa = 1$, $t_{d,\rm min} = 500$ Myr and redshift bin sizes are $\Delta z = 0.05$ in the interval of $[0, z_{\rm max}] = [0, 0.3]$.

Redshift bin	N_{GW}
$0 \leq z \leq 0.05$	1
$0.05 < z \leq 0.10$	7
$0.10 < z \leq 0.15$	19
$0.15 < z \leq 0.20$	35
$0.20 < z \leq 0.25$	56
$0.25 < z \leq 0.30$	80

Table 5.1: Number of mergers in different redshift bins computed via Eq. (5.8) with the observing time set as $T_{\rm obs} = 1$ yr.

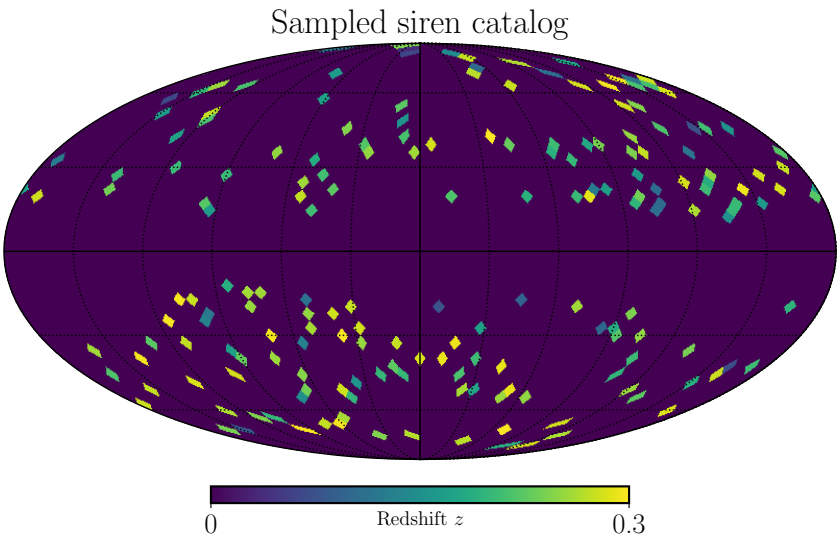

Figure 5.6: HEALPix map for the spatial distribution of sampled sirens which is discussed in Fig.((5.5)) with observation time of $T_{\rm obs} = 1$ yr.

5.2 Mass Distribution of Binary Black Holes

Now having the number of GW mergers in each redshift bin, we proceed to model their mass distribution. We will first study a simple case, where all the implicit and explicit dependencies on astrophysical properties, such as halo mass, metallicity, and star formation rate are suppressed. Then we investigate what potential impacts they have, if they are not suppressed.

5.2.1 Mass Distribution of Black Holes

To acquire the mass distribution of black holes, we begin with initial distribution of masses for star population, i.e. the Initial Mass Function (IMF). The term initial refers to the formation of stars from a parent gas cloud before any star evolution or merger occurs. However, eventually this mass distribution of stars will translate into the distribution of stellar compact objects that source the black hole population. The mass lost during the formation of black holes from stars is denoted by the loss function. This loss function is typically dependent on stellar winds since after the explosion of a star, some portion of the

initial mass and the separated mass will be carried to the interstellar medium (ISM) by the stellar winds.

Fundamental arguments indicate that the initial mass function (IMF) should change with the pressure and temperature of the cloud in which star is forming, with higher temperatures resulting in higher average stellar masses.
Here, we implement a phenomenological model in which all the physics, from star formation to black hole black formation is encoded in only a few parameters. We start by assuming the mass distribution of black holes mostly follows the same power-law behaviour as the mass distribution of stars given by Kroupa IMF [44] and it is redshift independent,

$$p_s(m)_{\text{Kroupa}} \propto \begin{cases} 0 & m < m_{min} \\ m^{-\alpha_k} & m \geq m_{min} \end{cases}. \tag{5.9}$$

The α_k parameter differs for different mass ranges but for higher mass ranges is estimated to be about 2.3 ± 0.7. The population of very low mass stars ($< 0.5M_\odot$) may not follow this distribution, but they are irrelevant to our study here and we set it to be zero since for stellar black holes the minimum mass would corresponds to upper bound on mass of neutron stars. In this work we take m_{min} to be greater than $5M_\odot$. Fig. ((5.7)) displays mass distribution $p_s(m)_{\text{Kroupa}}$ for slightly higher and lower values of α_k.

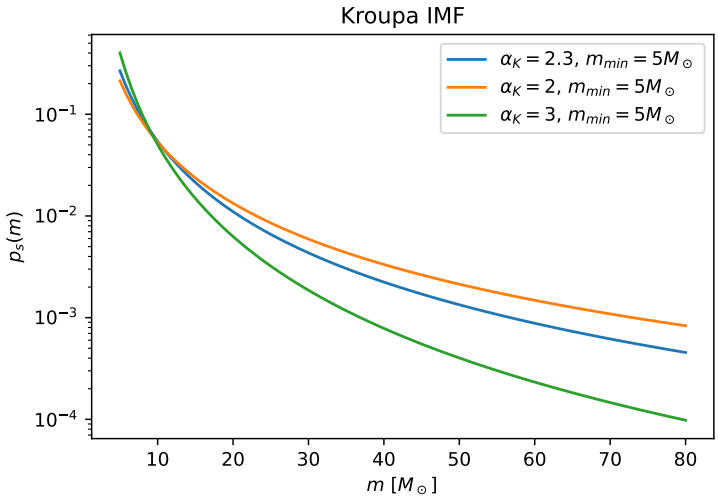

Figure 5.7: Black hole mass distribution for different values of α_k.

5.2.2 Distribution of Black hole Masses in BBH Mergers (Phenomenological Modelling)

We will now further adjust the black hole mass distribution to model BBH mass distribution at merger redshift taking into other theoretical constraints and observational evidence. We have already imposed a lower bound on mass of stellar black holes as mentioned above, we can also impose an upper bound, m_{max}, corresponding to the maximum mass scale accessible to stellar black holes in their formation channels. The absolute expected cut-off is to be set by the pair-instability supernovae process (will be explained soon) which its exact values is still being studied but but it is expected to be higher than $45M_{\odot}$ [50, 30]. Observations from LVK collaboration [10] and population synthesis models [42] also indicate a bump or pile up close to the pair-instability mass scale, which we model with super-imposing a Gaussian peak on top of the stellar mass distribution [64, 65] as,

$$p(m) \propto p_s(m)_{\text{Kroupa}} + \lambda_g N_g(\mu_g, \sigma_g), \tag{5.10}$$

where λ_g, σ_g are free parameters and μ_g is so-called PISN mass. These parameters are meant to capture the impact of pair-instability of supernovae and related to the physics that happen from star formation to the merger state of black holes. If these parameters are well fitted to observation and happen to be redshift dependent by observation, they can provide valuable information about different formation channels of black holes. Fig. ((5.8)) shows examples of mass distribution probability (at merger redshift) $p(m)$ with a power law assumption and a Gaussian peak.

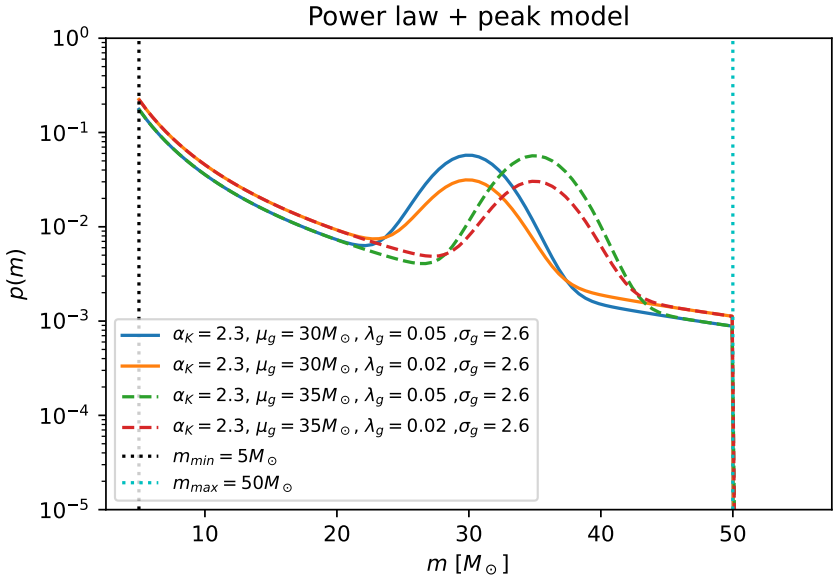

Figure 5.8: Mass distribution in BBH mergers with a power law assumption and a Gaussian peak.

5.2.3 Black Hole Mass Distribution at the Merger Redshift (Physical Modeling)

In last subsection we provided a phenomenological prescription for modeling the GW sources, we know provide a more physically motivated prescription. In practice our numerical package is equipped to implement both approaches.

As mentioned previously, present-day detection of GWs is a new and promising approach for inferring cosmological parameters. Although GWs can provide a good measurement for luminosity distance of the GW source, individual measurements can not provide the redshift information independently. However, if the population distribution of *observed* BBHs depends on astrophysical properties of their environment then exploring the redshift dependencies could lead to utilising GW data to break the degeneracy with other astrophysical and cosmological quantities as well.

We now model the redshift dependence of the observed BBH events mass distribution (at merger time) in the following way: first that the mass scale of pair-instability supernovae (PISN) at formation time has metallicity dependence and then that the evolution of the stellar metallicity itself is redshift dependent. Next since there is a delay time between

formation and merger, at any redshift the merger distribution is mixture of BBH that were formed at different redshift earlier.

It is worthwhile to start by answering this question first: what is the PISN mass? The stellar evolution theories predict a mass gap in the black hole mass distribution due to the mass loss of heavy stars during pair-instability supernovae process (PISN). These studies anticipate this process to happen due to the over production of electrons-positrons pairs and a follow up drop of the internal pressure. That will then lead to partial collapse of the star which causes accelerated burning in a runaway thermonuclear explosion. Star is eventually blown apart without leaving a compact remnant behind. The maximum stellar BH masses is expected to range between 40 and 50 $M_\odot$ which has been mostly consistent with the current population of detected binary black holes with the absence of black holes with masses more than $45M_\odot$. However, there maybe possible pathways to get a BBH merger in the PISN mass gap. For example, the most massive stellar black hole discovered to date is the primary of GW190521, with BHs with mass about $85^{+21}_{-14}M_\odot$ and $142^{+28}_{-16}M_\odot$ which is in the mass gap but a possible explanation to this is that it might have been populated by the mergers of smaller black holes which assumed to be rare and subdominant.

All in all, the start of the mass gap in the stellar mass distribution due to the PISN process is expected to be about $45M_\odot$ but change due to the stellar metallicity variation with the rate about 7% in the interval $Z = [10^{-5},\ 3\times10^{-3}]$ [49]. The PISN mass scale can also be affected by nuclear reaction rates with about 35% but since this parameter will not evolve with redshift, it will not be relevant to our calculation. In our analysis, we follow the approach taken in Ref. [42, 50] to model the redshift dependence of the PISN mass scale as

$$M_{\rm PISN}(Z) = M_{\rm PISN}(Z_*) - \alpha_Z \log_{10}(Z/Z_*) \tag{5.11}$$

where Z is the metallicity, α_Z is a free parameter and based on the results obtained by Ref. [30] $Z_* = 10^{-4}$ for $M_{\rm PISN}(Z_*) = 45{\rm M}_\odot$. If we do not have the metallicity information for the host galaxy in the catalog we estimate it using the mean metallicity of the Universe at each redshift by:

$$\log_{10}(Z(z)) = \gamma z + \zeta \tag{5.12}$$

where ζ is the current metallicity of the Universe (at $z = 0$) and γ is a free parameter capturing the redshift dependency.

Next, as noted before the mass distribution of merging black holes at redshift z_m will include contributions from black holes which were formed at earlier redshifts ($z > z_m$) due to non-zero delay-time. The sources at higher redshifts have lower metallicity leading to larger PISN mass scales compared to the BHs formed at lower redshifts (see Eq. (5.11)).

In other words, we have modeled the black hole mass distribution in the source frame. However, since each binary needs some time (so-called delay-time) to find its companion, binaries merging at a particular redshift have formed at different redshifts (see Fig. (5.9)) [42, 50, 30]. In principle, we have time lapsed between the formation of a star and the black holes and also individual black holes coming from different stellar-mass distributions and redshifts as well. However, we neglect the time lapsed between the formation of a star and the BH in comparison to the cosmic time scale of it to merge (which is a few hundred Myr to Gyr) and also assume the formation redshift of the two parent stars are also close compared to merging times.

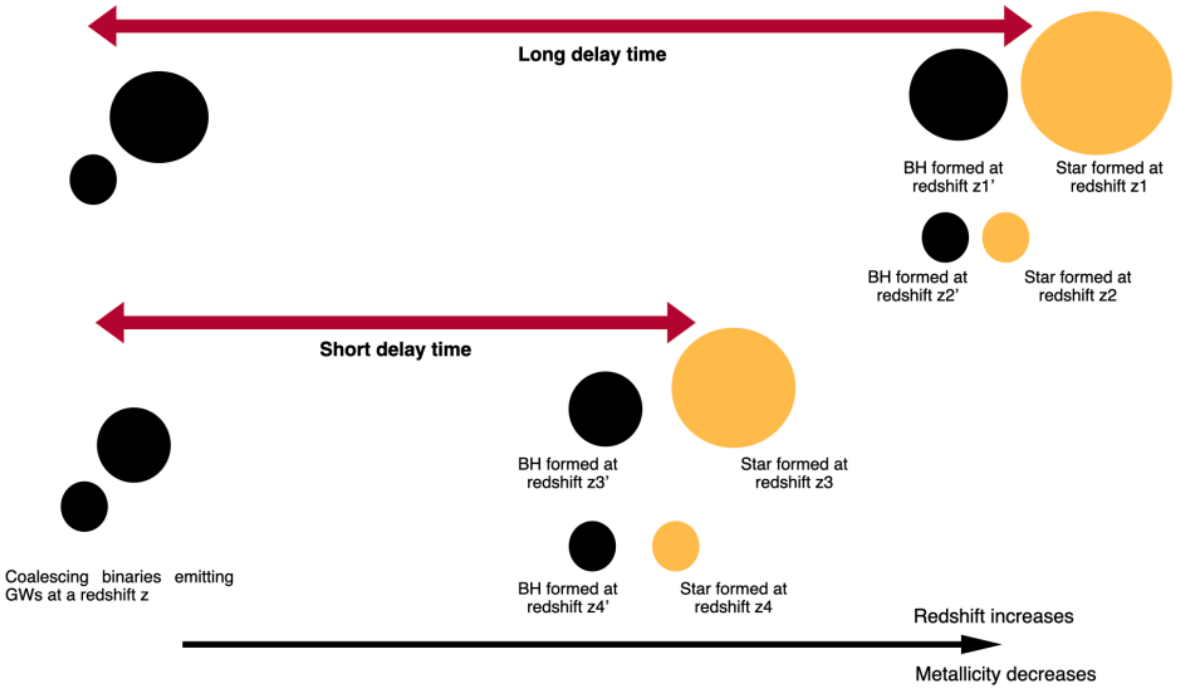

Figure 5.9: A diagram showing how the redshift dependence of the PISN mass can contribute to the mass distribution of the discovered GW events. Since delay time distribution acquire a non-zero value above the minimum delay time, BHs created at various redshifts can merge at the same redshift. Image adopted from Ref.[50].

For producing the observer frame mass distribution (onset of coalescence), we argue [42]:

$$\mathcal{P}(m(z_m)) = W(m(z_m))\mathcal{P}_s(m) \tag{5.13}$$

where $\mathcal{P}_s(m)$ is the mass distribution of BHs at any redshift (Eq. (5.9)) and $W(m(z_m))$ is the accumulated window function for allowed black hole masses in a binary system at the merging redshift[1]. One way to understand the logic behind this equation is that at a particular redshift(z_m), the mass distribution of all BHs would be given by $\mathcal{P}_s(m(z_m))$. Then the probability of some of these objects for merging in a binary system is taken into account by $W(m(z_m))$.

To calculate the window function, $W(m(z_m))$, we make a convolution of source frame window function at different formation redshifts as:

$$\mathcal{W}(m(z_m)) = \mathcal{N} \int_{z_m}^{\infty} P_{t_d}(z_m, z') \mathcal{W}_s(m(z')) dz' \tag{5.14}$$

where $\mathcal{W}_s(m(z'))$ is the mass window function in the source frame or basically allowed mass range at each redshift. $\mathcal{N}$ is a normalization factor so that $\int \mathcal{W}(m(z_m))dm = 1$. Here we set the allowed region of masses in the source frame to be from our assumed minimum stellar BH mass value up to the PISN mass,

$$\mathcal{W}_s(m(z')) = \begin{cases} 1 & m_{min} \leq m \leq M_{PISN} \\ 0 & \text{otherwise} \end{cases} \tag{5.15}$$

Since the delay time distribution we had obtained in (5.3) was expressed as a function of time difference between the formation and merger redshifts, $t_d = t_m - t_f$, and not the redshift, we make a change of variables similar to Eq. ((5.1)), and rewrite equation ((5.14)) as:

$$\mathcal{W}(m(z_m)) = \mathcal{N} \int_{z_m}^{\infty} P(t_d) \frac{dt_f}{dz'} \mathcal{W}_s(m(z')) dz' \tag{5.16}$$

The window function in the observer frame or at merging redshift (Eq. (5.14)) is shown in Fig. ((5.10)).

[1]In principle, $\mathcal{P}_s(m)$ can be redshift dependent as well and in that case, it should be convoluted in the integration with the window function at the formation redshift.

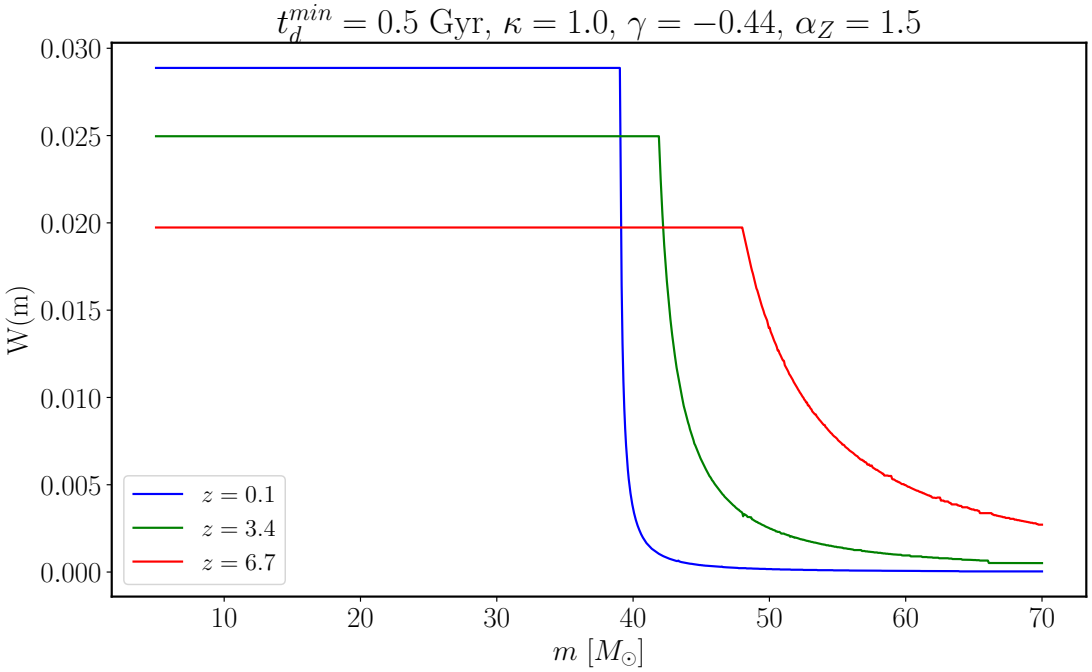

Figure 5.10: Window function, $\mathcal{W}(m(z_m))$ for different merger redshifts

Then we multiply these window functions with the source frame mass distributions $\mathcal{P}_s(m)$ using Eq. ((5.9)) to get the mass distributions in the observer frame or at the merger redshift. Plots in Fig. ((5.11)) exhibit the redshift dependence of $\mathcal{W}(m(z_m))$. For simplicity we have also imposed an uppercut of $m_{max} = 70$, since the probability is negligible beyond that value. As can be seen, the sources with higher redshift and consequently lower metallicity will have a larger PISN mass scale value. Fig. ((5.12)) shows how this will impact $\mathcal{P}(m(z_m))$ the mass distribution in merger(observer) frame.

It is worth noting here that as we have described so far in our model SFR and metallicity both can impact the merger population through the merger rate (5.1) and the BBH mass distribution (5.11). In some galaxy surveys such as SDSS DR7, these two parameters are measured for individual galaxies. For others like GLADE+, we can use Eqs. (5.12) and (5.2) to model and calculate these two quantities.

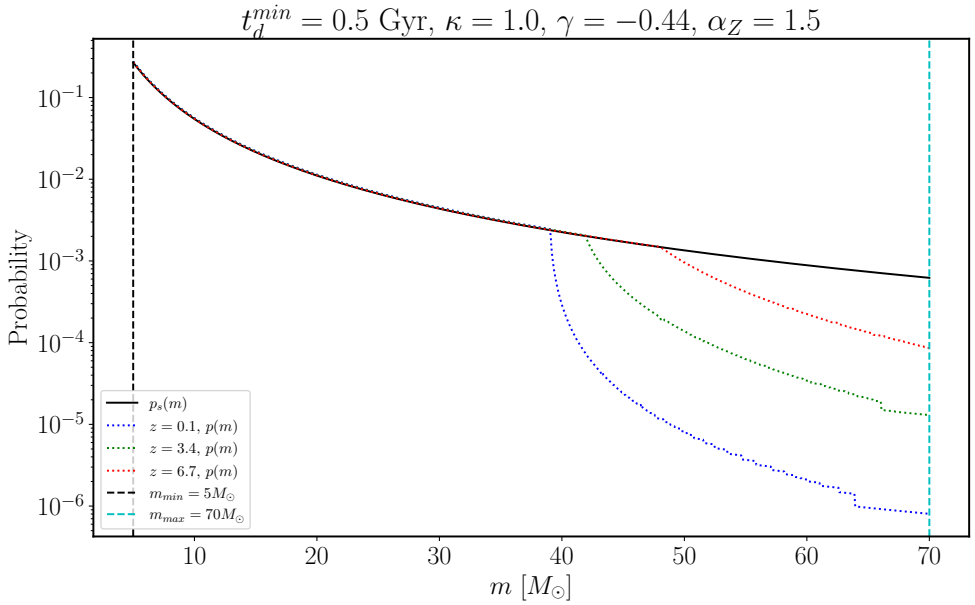

Figure 5.11: Mass distribution at merger(observer) frame at different merger redshifts

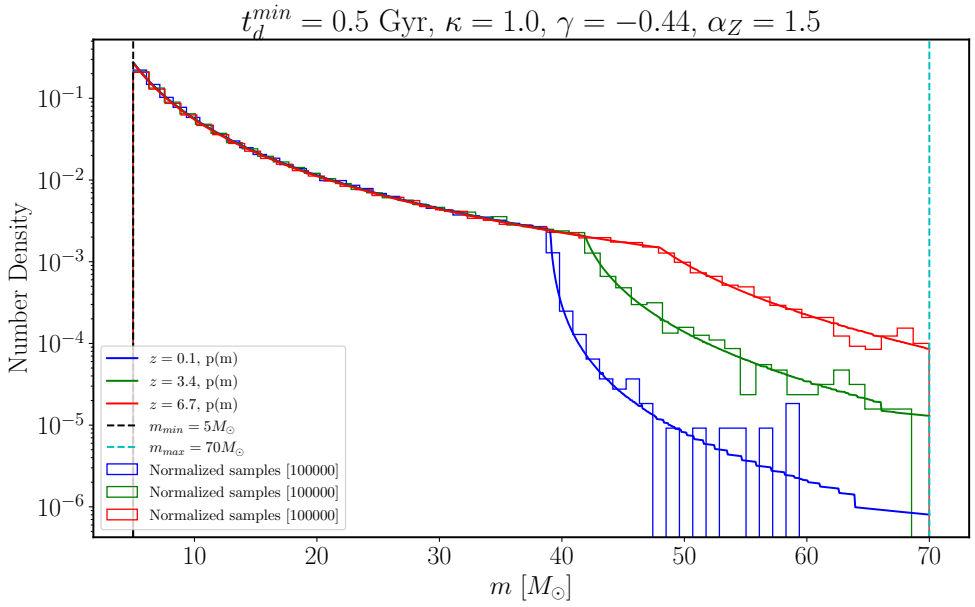

Figure 5.12: Samples for mass distribution in the observer frame.

5.2.4 Secondary Mass in Binary

While we have modeling the probability mass distribution of individual black holes that are merging at z_m, every BBH consists of two companion masses so it involves sampling a primary black hole (m_1) out of the distribution and a secondary black hole (m_2) out of it as well. To do this, we can take two approaches.

- In the first approach, the secondary mass distribution is following the primary mass distribution but conditioned to be less than m_1 (this is equivalent taking the conditional probability to include a mass ratio between $[m_{min}/m_1, 1]$ from a uniform distribution for the mass ratio as well). That extra condition however, makes the secondary mass distribution different from the distribution of the primary mass as shown in Fig. (5.13).

- In the other approach, we choose the conditional probability for m_2 to include a power-law with a positive index (β_{m_2}), minimum and maximum cuts as $[m_{min}, m_1]$. Note that, here although a single m_2 in a binary system is conditioned to be sampled from a positive power-law distribution, the global distribution of m_2 in all binaries, more or less follows the the negative power-law of m_1, see Fig (5.14). Finally, assuming $\beta_{m_2} = 0$ is equivalent to acquiring option 1 to sample the secondary mass of the binary since if we choose m_2 from a power-law with zero index and between $[m_{min}, m_1]$, we are only conditioning m_2 to be less than m_1 (which is confirmed by sampling in Fig. (5.14)).

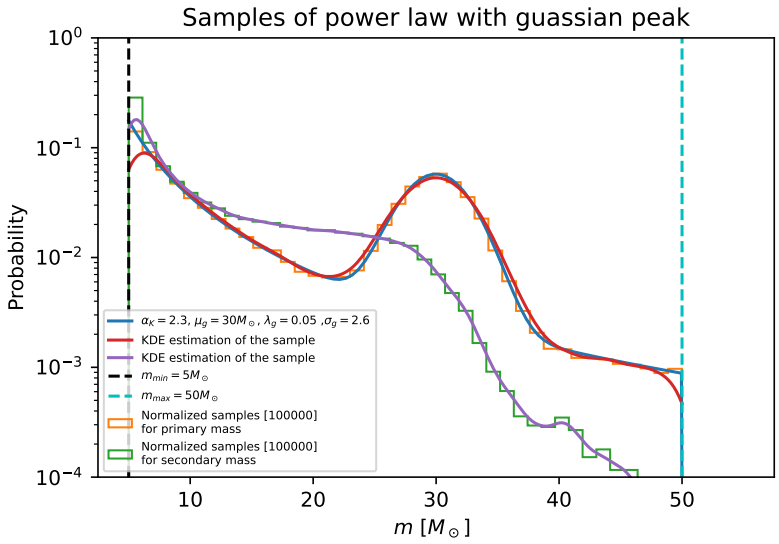

Figure 5.13: Samples (rejection sampling) of primary and secondary mass for power law+peak model .

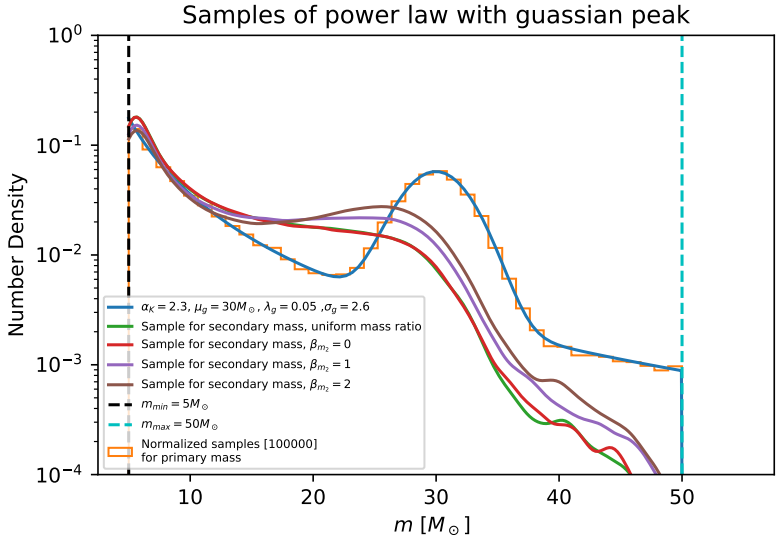

Figure 5.14: Samples of secondary mass for power law+peak model with different β values.

5.3 Assigning galaxies to the possible hosts of sirens

In the previous sections, we provided a model for mass and redshift dependence of BBHs. We now like develop a framework to calculate their distribution among galaxies based on astrophysical properties. In other-words obtain probably functions for identifying host galaxies. We will then implement them in our code that utilizes these probabilities as the chance of a galaxy being selected as the host. We call these probability functions galaxy selection functions.

5.3.1 1 Dimensional Selection Function

We first consider the galaxies selection functions for different properties to be independent of each other and each be a power low comprised of five parameters as

$$P(g) \propto \begin{cases} 0 & g \leq g_{min} \\ g^{\alpha} & g_{min} \leq g \leq g_{*} \\ g^{\beta} \frac{g_{*}^{\alpha}}{g_{*}^{\beta}} & g_{*} \leq g \leq g_{max} \\ 0 & g \geq g_{max} \end{cases} . \tag{5.17}$$

where g would be an astrophysical feature of a galaxy such as mass, metallicity, or star formation rate (SFR). Powers α and β are assumed to be positive and negative respectively and g_{min}, g_{max}, g_{*} represent the cut off values and transition scale from monotonically growing to decaying for the corresponding feature.

Fig. ((5.15)) displays the schematic behaviour of the selection function in Eq. ((5.17)) if g is chosen to be the mass of the galaxies. It also portrays the performance of our sampling scheme in our code. In this example we have taken the galaxies from GLADE+ catalog.

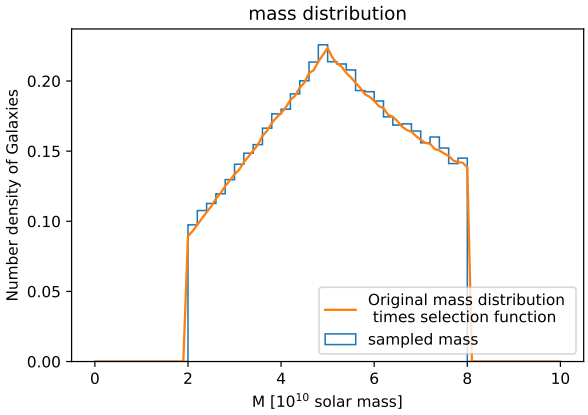

Figure 5.15: The selection function is from Eq. (5.17) where g is the mass of galaxies, $m_{min} = 2 \times 10^{10} M_{\odot}$, $m_* = 5 \times 10^{10} M_{\odot}$, $m_{max} = 8 \times 10^{10} M_{\odot}$, $\alpha = 1$, and $\beta = -1$. The number of samples is 80000 out of 3689580 galaxies.

5.3.2 3 Dimensional Selection Function

In previous subsection we assumed the galaxy selection functions for different astrophysical features are independent from each other. However, in principle, these properties are not independent. Therefore, we equip our code to accommodate the probability of selecting a host galaxy with mass (M), star formation rate (SFR) and metallicity (Z) as a joint probability $P(M, SFR, Z)$. The joint probability can be split in multiple conditional probabilities depending on specific astrophysical models. For example it can be implemented in our code in the following is:

$$P(M, SFR, Z) = P(M|SFR, Z)P(SFR, Z) = P(M|SFR, Z)P(SFR|Z)P(Z) \quad (5.18)$$

Or if we assume M, SFR, and Z are independent, the joint probability reduces to

$$P(M, SFR, Z) = P(M)P(SFR)P(Z), \quad (5.19)$$

where we can take $P(M)$, $P(SFR)$, and $P(Z)$ to follow the selection functions provided in (5.17). We tested the joint probability sampling package for independent selection functions to make sure our code is reliable. The results for joint probability, taking into account mass dependent, while assuming uniform prior on SFR and metallicity are shown in Fig. ((5.16)). The figure is for galaxies with real masses from GLADE+ galaxy catalog. The GLADE+ galaxy catalog does not have metallicity and SFR information, so we artificially produced

some random metallicity. The SFR can be also calculated by Eq ((5.2)). Now we have a selection function that enable us to choose the host galaxies based on their astrophysical properties such as SFR, Mass and metallicity.

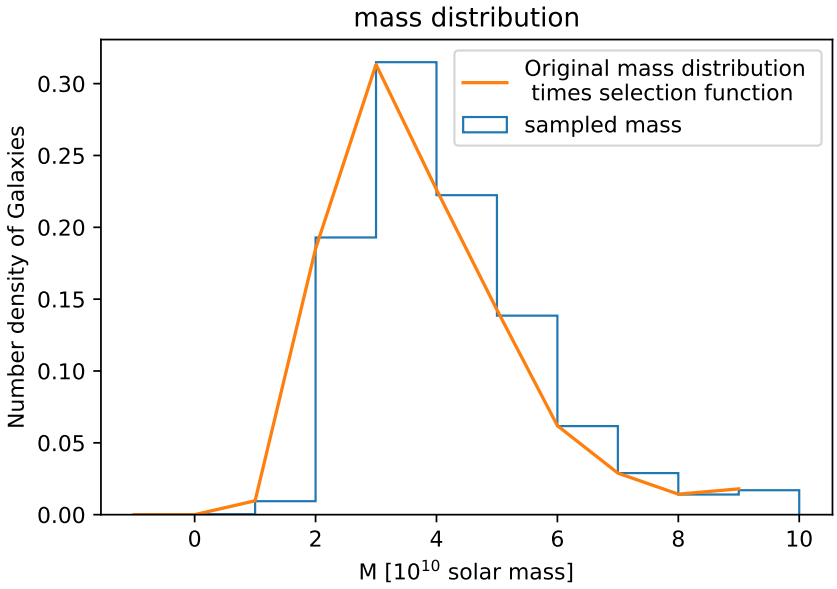

Figure 5.16: The selection function is from Eq. (5.19). For the mass selection $m_{min} = 0M_{\odot}$, $m_* = 5 \times 10^{10} M_{\odot}$, $m_{max} = 10 \times 10^{10} M_{\odot}$, $\alpha = 1$, and $\beta = -1$. For SFR and metallicity part $\alpha = \beta = 0$ with no cutoff which basically means random selection. Here the considered redshift bin of the galaxy catalog here is $0.25 < z \leq 0.30$. The number of samples is 80000 out of 3689580 galaxies.

5.4 Modeling GW Bias Parameter for Angular Power Spectra through GLADE+ Catalog

In this section, we will make theoretical modeling of the GW bias for angular power Spectra and apply it to GLADE+ catalog. This will involve producing a masked density map to get a more uniform galaxy map and to manage the shot-noise, then calculating 2D power spectrum for both galaxies and sirens with and without shot-noise subtraction. We will finally obtain the GW bias parameter for GLADE+ catalog. In next section, we will model GW bias for 3D power spectra for galaxies and sirens for the SDSS Dr7 catalog and then calculate bias parameter.

5.4.1 Density Map

Given a galaxy catalog such as GLADE+ (Appendix.(A)), we can use our prescription in the previous sections to sample the galaxy hosts of the expected number of GW sources (sirens), N^a_{GW}, in a redshift bin (denoted as a) out of it. We can then compute the redshift-bin density map by computing the over-density in each pixel with label i, as

$$\delta^a_{GW,i} = \frac{N^a_{GW,i}}{\bar{N}^a_{GW}} - 1, \tag{5.20}$$

where $N^a_{GW,i}$ is the number of sirens in the pixel i of the redshift bin a. $\bar{N}^a_{GW}$ is the redshift bin-specific average number of sirens a pixel. The average is computed from $\bar{N}^a_{GW} = N^a_{GW}/(n_{\rm pix} \times f_{sky})$, where N^a_{GW} is the total number of mergers in each redshift bin and $n_{\rm pix}$ is the number of pixels, determined by $n_{\rm pix} = 12N^2_{\rm side}$ in the Hierarchial Equal Area isoLatitude Pixelization (HEALPix)[2] language [35].
By prescribing an over-density to each pixel, we can generate a density map rather than a position map [3] which was previously shown for random host selection (not applying galaxy selection functions) in Fig. (5.6) . As can be noted there the expected number of GW events per year is too low to produce a meaningful power spectrum for sirens. Therefore, we amplify the number of sirens by a constant factor ($N_{GW}(z_a) \to 10^4 N_{GW}(z_a)$) in all the redshift bins $[z_a - \Delta z/2, z_a + \Delta z/2]$[4]. The left panel of Fig. (5.17), shows a density map of

[2] https://healpix.sourceforge.io/

[3] When we were making these plots initially for the first version of GLADE+, we discovered a bug in the catalog which has since been fixed!

[4] Note that since we multiply each number by a constant number, this is effectively the same as increasing the observation time by that factor.

the galaxy catalog in a HEALPix plot for the redshift bin $0.1 \leq z \leq 0.15$ while the right panel of Fig. (5.17) shows the density map of the GW catalog for the same redshift bin, and with the "jacked up" number of sirens from the ones computed in Section (5.1.2). As expected, the GW density map in the right panel is a just more grainy and less-smooth version of the density map in the corresponding redshift bin of the GLADE+ catalog since no galaxy selection function is applied.

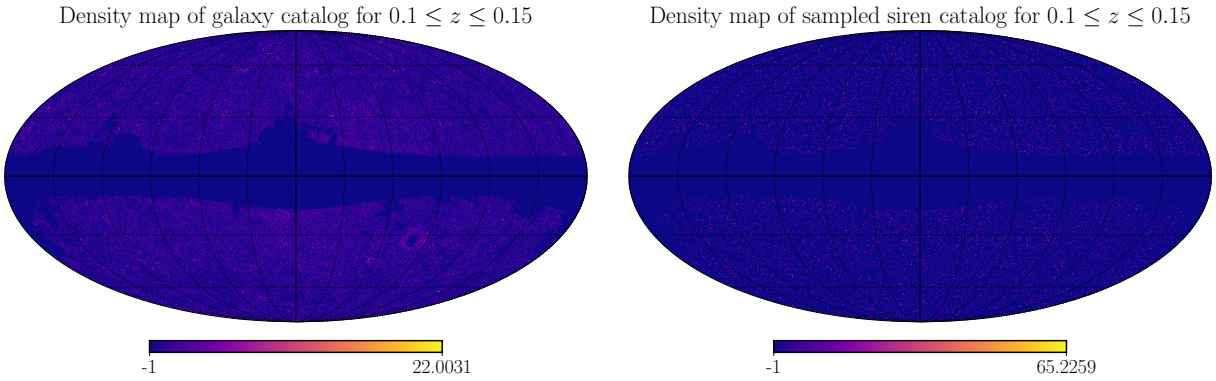

Figure 5.17: Left panel: HEALPix map for the density map of galaxies in the GLADE+ catalog in the redshift bin $0.1 \leq z \leq 0.15$. Right panel: HEALPix map for the density map of (amplified) sirens in the GLADE+ catalog in the redshift bin $0.1 \leq z \leq 0.15$ for an observation time of $T_{\rm obs} = 10^4$ yr. Both figures are produced with $N_{\rm side} = 128$ for demonstration purposes.

5.4.2 Binary Mask

Since the GLADE+ catalog is composed of several various galaxy surveys, we construct a binary mask to mask over the remaining incomplete regions and the galactic plane. Fig. (5.18) shows the two maps in question. The left panel corresponds to a HEALPix map of the full GLADE+ catalog across all redshifts with $N_{\rm side} = 512$, while the right panel corresponds to a HEALPix map generated with $N_{\rm side} = 256$ so that the mean number of galaxies inside non-empty pixels[5] was about ~ 32. In this binary map, we have taken the pixels with no galaxies to have a density equal to 0, and pixels with galaxy counts less than a threshold amount of 15 to have a density equal to 1 (we are also masking bright

[5]This is with the goal of having an average of about ~ 25 galaxies in non-empty pixels so that a pixel with zero galaxies is a 5σ fluctuation, where $\sigma = \sqrt{\bar{N}_{\rm gal}}$ is the mean in Poisson statistics.

parts). This was chosen so that the galactic plane and the brighter regions in the map are masked out.

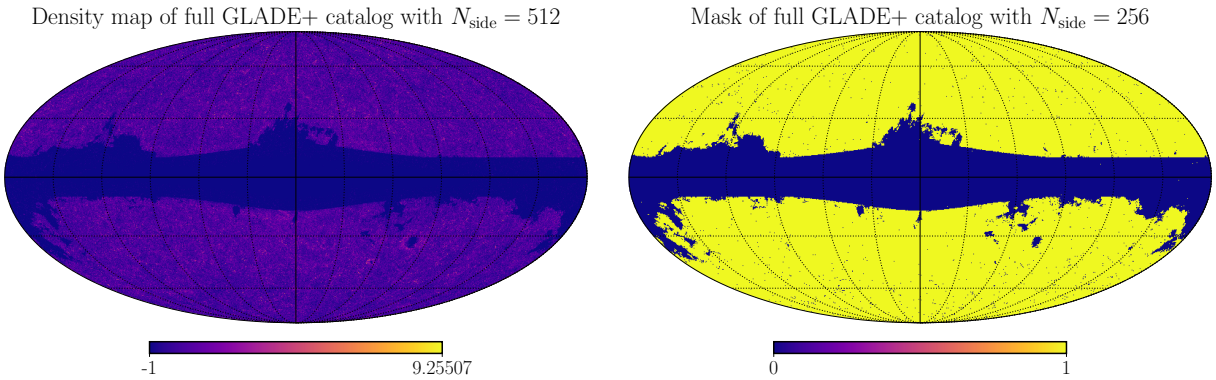

Figure 5.18: Left panel: HEALPix map of the full galaxy catalog with $N_{\text{side}} = 512$. Right panel: HEALPix map of the binary mask with $N_{\text{side}} = 256$. The resolution was chosen so that the mean number of galaxies inside a non-empty pixel was given to be ~ 32. The threshold amount of galaxies in the mask was 15 so that the galactic plane and the middle "strip" in the upper middle part of the map is sufficiently masked.

After producing the map, we use the `healpy.ud_grade()` method to increase the resolution of the mask to match the resolution of the density map. By multiplying the mask to the map, we produce the masked density map. Hence to produce redshift-binned power spectra, we multiply the density map in each redshift bin with the full-survey mask.

5.4.3 Shot Noise

We compute the shot noise associated with each sample of galaxies/GWs via

$$\sigma^2_{n,X} = \frac{1}{n_X}, \tag{5.21}$$

where X is a label for either galaxies or GWs and n_X is the number density. Recall that the definition of number density function was taken to be (suppressing any redshift labels since we will be working with the first redshift bin temporarily):

$$n_{X,i} = \frac{N_{X,i}}{\bar{N}_X} - 1, \tag{5.22}$$

where i is the pixel label and $N_{X,i}$ is the number of galaxies/GW samples in the corresponding pixel. $\bar{N}_X$ is the average number of galaxies/GW samples in an unmasked pixel, ie. the pixels where the binary map has a value of 1. Note that, we must consider the fraction of the sky that remains after masking. In other words, we introduce a sky fraction parameter f defined through the pixels of the mask via

$$f = \frac{\text{non-zero pixels}}{\text{total pixels}}, \tag{5.23}$$

and then can write

$$\bar{N}_X = \frac{N_{X,tot}}{f n_{pix}}, \tag{5.24}$$

where n_{pix} is the total number of pixels in the `HEALPix` map, and f is the sky fraction defined by the binary mask. We can now perform a sanity check to see our shot noise subtraction behaves well by setting the various parameters of the model to a base model case with no mass sampling or metallicity selection. We label this model as the *fiducial* model and the values for the relevant model parameters can be found in Table (5.2).

Model parameter	Value
$z_{\max}$	0.3
N_{bins}	6
T_{obs}	10^4 yr
$t_{d,\min}$	500 Myr
N_{thresh}	15
$n_{\text{side,map}}$	512
$n_{\text{side,mask}}$	256

Table 5.2: Fiducial values for the *simple* model parameters. Note that we take $z_{\min} = 0$ to be fixed across all models so that the redshifts considered are $z \in [0, z_{\max}]$.

We can compute the shot noise for both galaxies and sirens, Fig. (5.19) shows angular power spectrum for large values of the multipoles, ℓ, converges towards the computed shot noise as expected. In what follows in the next section, we will subtract this shot noise out and compute the relationships between the two bias parameters involved.

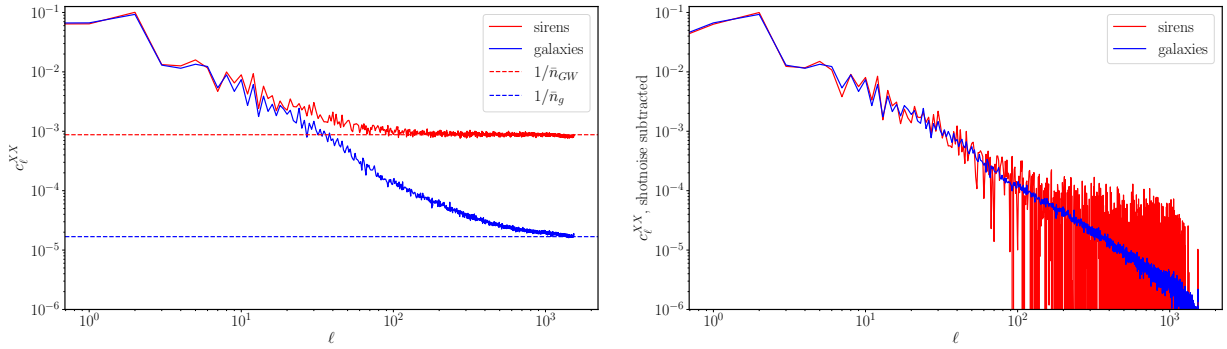

Figure 5.19: **Left**: Corrected c_ℓ^{XX} for the first redshift bin in the fiducial scenario. The dashed lines represent the theoretical estimate for shot noise. **Right**: Corrected c_ℓ^{XX} for the first redshift bin with the theoretical shot noise term subtracted off.

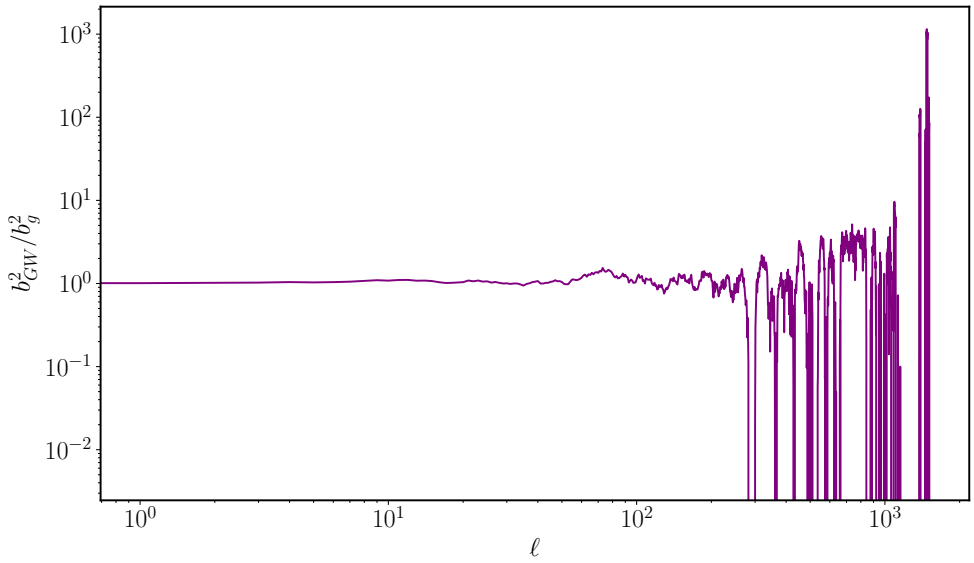

Figure 5.20: Bias parameter in the first redshift bin of the fiducial model.

The left panel of Fig. (5.19) shows the corrected form of c_ℓ, with the sky fraction divided off of the masked c_ℓ outputs. The dashed lines represent the theoretical estimates for shot noise, which seems to match much better with the asymptotic behaviour of the c_ℓ's for high ℓ-values. However, the c_ℓ for sirens still ends up dipping below the shot noise line. The right panel of Fig. (5.19) shows the resulting c_ℓ's with the theoretical estimate of

shot noise subtracted off. For low ℓ there is excellent agreement as expected. Also dividing the two subtracted angular power spectra, we obtain the ratio of the bias parameters GW sources to galaxies, b^2_{GW}/b^2_g be one (shown in Fig. (5.20)) as theoretically expected since we have not applied any galaxy selection functions at this point.

5.4.4 Theoretical Error Estimation for Angular Power spectrum and Bias

When the variables in a function represent the values of observational measurements, their measurement uncertainties propagate due to the combination of variables as a result. If we assume Poison-sampling from a Gaussian density field for both galaxies and sirens is a good approximation then the expected error for bin-averaged power spectrum is given by standard theoretical Gaussian errors, i.e.:

$$\sigma_{C_{l,gg}} = \sqrt{\frac{2C^2_{l,gg}}{(2l+1)\Delta l f_{sky}}} \tag{5.25}$$

$$\sigma_{C_{l,ss}} = \sqrt{\frac{2C^2_{l,ss}}{(2l+1)\Delta l f_{sky}}} \tag{5.26}$$

where l, and Δl are the center and the width of the bin and f_{sky} is the sky fraction. For analytical calculation of the error for bias in previous subsection, we have used the following error propagation scheme:

$$\sigma_{\text{bias}} = \sqrt{2}\sqrt{(\frac{1}{C_{l,gg}})^2\sigma^2_{C_{l,ss}} + (\frac{C_{l,ss}}{C^2_{l,gg}})^2\sigma^2_{C_{l,gg}} - 2\frac{C_{l,ss}}{C^3_{l,gg}}cov(C_{l,ss}, C_{l,gg})} \tag{5.27}$$

where *cov* is given by:

$$cov(C_{l,ss}, C_{l,gg}) = \frac{C_{l,gg}C_{l,ss} + C^2_{l,gs}}{(2l+1)\Delta l f_{sky}} \tag{5.28}$$

5.4.5 Testing Gravitational Wave Bias Calculation for Uniform Galaxy Selection Functions

Having tested our shot noise subtraction, we continue to further test the sensitivity of our bias calculation to different parameters compared to the fiducial model with uniform

selection function on the survey. The ratio of the bias parameters squared for the mergers and the galaxies as a function of the multipole moments ℓ with different astrophysical parameters are plotted out in the following. All the plots will have the fiducial model as the top panel. Fig. (5.21) is with redshift bin size variation, Fig. (5.22) is with the masking threshold changed (note that this is the only scenario where the sky fraction is different), Fig. (5.23) is with $T_{\rm obs}$-variation, Fig. (5.24) is with κ-variation in the delay time distribution, while Fig. (5.25) is with $t_{d,min}$-variation in the delay time distribution. Interestingly enough, the final panel of Fig. (5.25), corresponding to a minimum delay time of $t_{d,min} = 10$ Gyr has c_ℓ's in the final redshift bin that are very spurious in the intermediate ℓ-values. The siren count corresponding to this bin is a whopping 2947, which could be why the spectrum gets shot noise dominated early on. As one can see by enhancing the minimum delay time, the number of mergers allowed in higher redshift bins decreases (since binaries do not have enough time to merge). Therefore, the power spectrum for sirens at higher redshift bins become shot-noise dominated much faster than at lower redshift bins due to the small sample size.

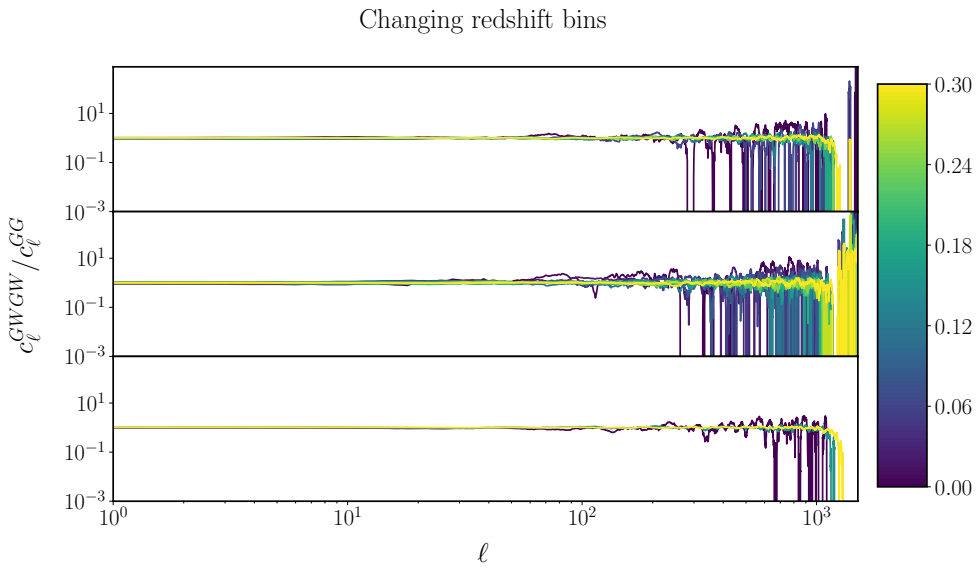

Figure 5.21: Fixed $c_\ell^{GWGW}/c_\ell^{gg}$ for various number of redshift bins. The right colour bar is in redshift, with yellow being the highest and blue being the lowest. **Top**: 6 redshifts bins with size $\Delta z = 0.05$ (fiducial model). **Middle**: 12 redshifts bins with size $\Delta z = 0.025$. **Bottom**: 3 redshifts bins with size $\Delta z = 0.1$. All other parameters were taken to be their fiducial values.

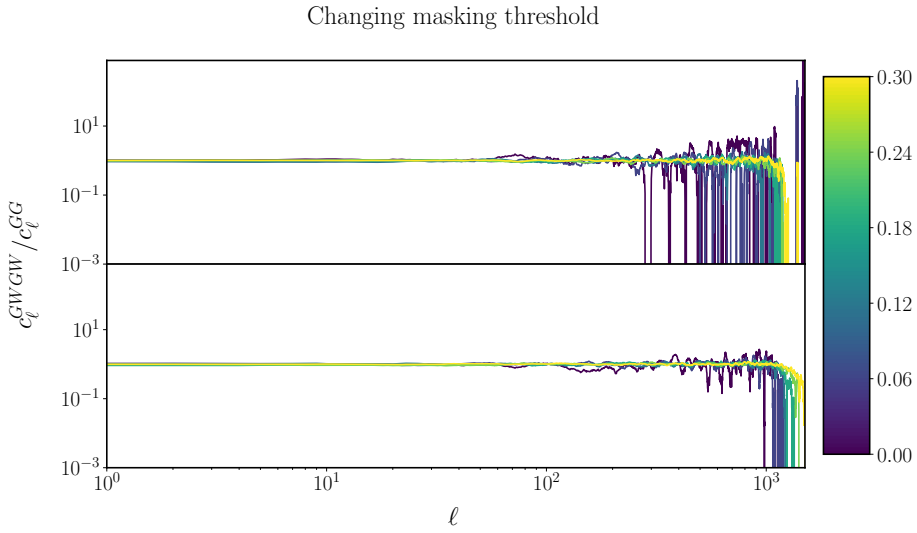

Figure 5.22: Fixed $c_\ell^{GWGW}/c_\ell^{gg}$ for different masking thresholds. The right colour bar is in redshift. **Top**: Fiducial model with a masking threshold of 15. **Bottom**: Masking threshold of 40.

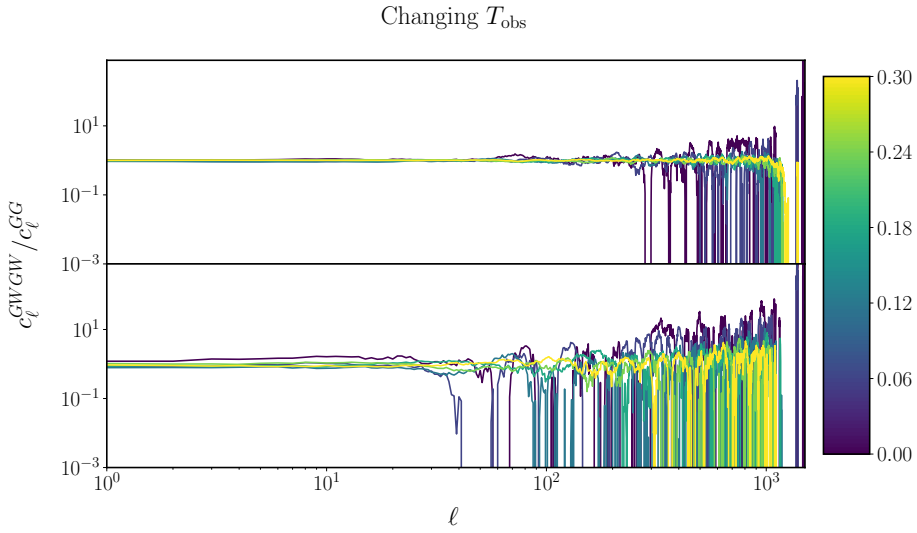

Figure 5.23: Fixed $c_\ell^{GWGW}/c_\ell^{gg}$ for different observation times $T_{\rm obs}$ in Eq. (5.8). The right colour bar is in redshift. **Top**: Fiducial model with an observation time of $T_{obs} = 10^4$ yr. **Bottom**: Observation time of $T_{obs} = 10^3$ yr.

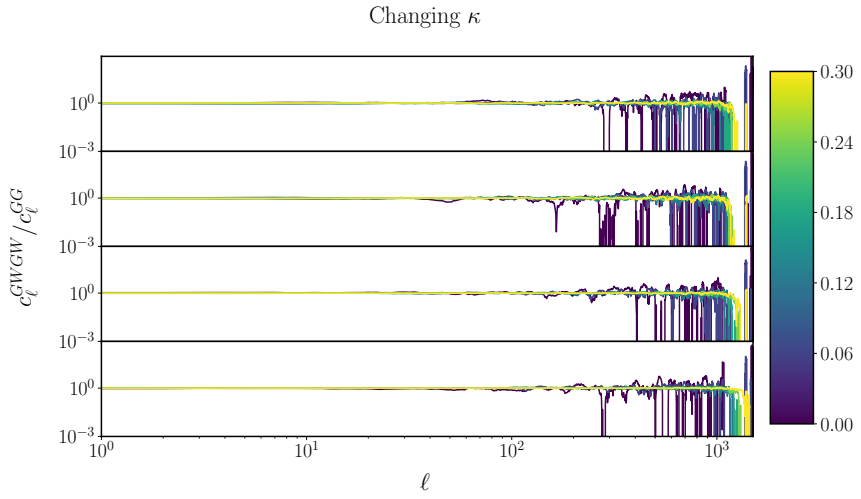

Figure 5.24: Fixed $c_\ell^{GWGW}/c_\ell^{gg}$ for different scaling κ in the delay time distribution Eq. (5.4). The right colour bar is in redshift. **Top**: Fiducial model with $\kappa = 1$. **Second**: $\kappa = 0.2$. **Third**: $\kappa = 2$. **Bottom**: $\kappa = 3$.

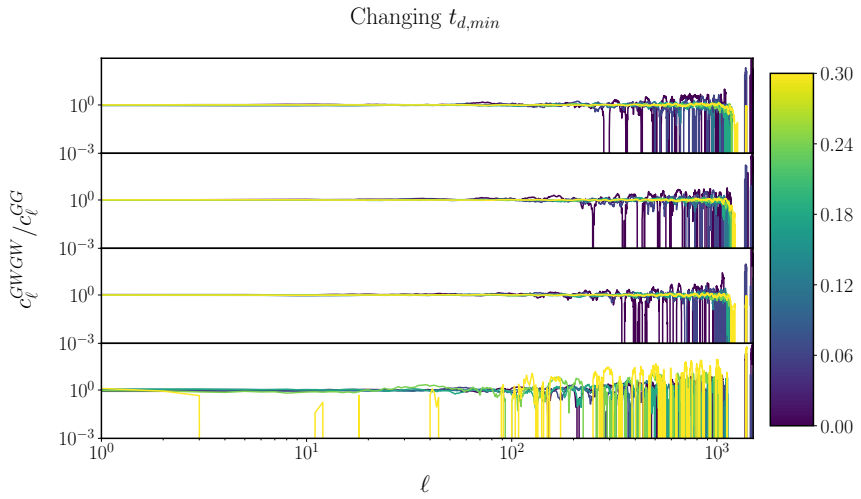

Figure 5.25: Fixed $c_\ell^{GWGW}/c_\ell^{gg}$ for different minimum delay times $t_{d,min}$ in the delay time distribution Eq. (5.4). The right colour bar is in redshift. **Top**: Fiducial model with $t_{d,min} = 500$ Myr. **Second**: $t_{d,min} = 100$ Myr. **Third**: $t_{d,min} = 1$ Gyr. **Bottom**: $t_{d,min} = 10$ Gyr.

5.4.6 Bias Calculation for Non-Uniform Galaxy Selection Functions

We now turn on the host galaxies selection functions for mass and SFR based on Eq. (5.17) and will compare the result to the fiducial model in Table.(5.2). Fig. (5.26) shows the ratio of biases squared for fiducial model in which we set $\alpha, \beta = 0$ for all parameters such as SFR, M and metallicity (see Eq.(5.17)). This means BBH hosts are selected randomly and it seems reasonable for the ratio to be about one for smaller values of $\ell \leq 1000$, where it can be interpreted as a uniform sampling of host galaxies.

Fig.(5.27) presents the effect of turning on the mass selection function on the bias parameter. We have tested 3 versions of mass selection, with $\alpha_M = -\beta_M = 1$ and $M_* = 5,\ 10,\ 100 \times 10^{10} M_\odot$. Error bars are theoretically calculated using (5.27), using the analytic Gaussian covariance for the angular power spectrum and Taylor series error propagation. For all 3 selection functions, we find that the ratio of the GW auto-correlation and the galaxy auto-correlation significantly increases at low redshift (i.e. the bias becomes greater than one). The results interestingly show that there is a clear redshift dependency due to using mass selection function on the bias and deviation from unity which we observed in the fiducial model. The increase in bias is statistically significant and the one sigma error bars for different redshift bins in figure (5.27) largely do not overlap with each other but it is harder to differentiate it from uniform sampling in the sixth redshift bin. To see the mass dependence trend better, we have plotted the the ratio of angular power spectra for three different mass selection functions in the 6th redshift bins in Fig.(5.29). The blue-dashed line shows the bias for the model where sirens are randomly selected. The bias is consistent with one within error bars for this model as expected. Orange, red, green lines are showing the bias for selecting the host of sirens based on different values of $M_* = 5,\ 10,\ 100 \times 10^{10} M_\odot$ and $\alpha_M = -\beta_M = 1$. One can see that the biases deviate from one and it increases with M_* which is consistent with saying if BBH are more probable to be hosted in more massive galaxies, they are also more clustered. As pointed out our result also indicate a redshift dependence for bias i.e. fixing the stellar mass selection, the GW bias is higher at low redshift (see Fig. (5.27)). This suggests that bias increases at lower redshift for fixed stellar mass distribution. This is a somewhat surprising result, as our expectation from previous works is that at a fixed stellar mass, bias should increase toward higher redshifts. For instance, figure 5 in [17] shows that at fixed stellar mass bellow $10^{11} M_\odot$, halo mass increases slightly towards higher redshifts. So for galaxies in that range one expects that bias increases monotonically at higher redshift. However, since we are not just fixing the stellar mass and choosing a distribution peaked at M_* but normalized over the survey the impact is more subtle. We are planning to further investigate this in

the follow up work.

Fig. (5.28) also presents the effect of turning on the SFR selection function. However, since Glade+ catalogue does not have SFR information, all the galaxies in the same redshift bin are assigned the same mean value and sampling based on SFR does not have any effect on bias ratio (see fig (5.28)). Therefore, in this analysis we conclude that bias can be indicative of the astrophysical properties of the host galaxies in this case their masses.

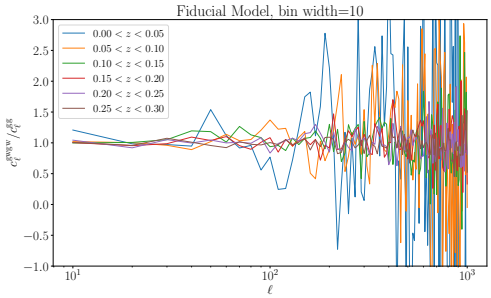

Figure 5.26: The bin-averaged bias parameter for fiducial model with parameters mentioned in Table.(5.2) in different redshift bins. Here $\alpha, \beta = 0$ which means sirens are randomly selected out of galaxies.

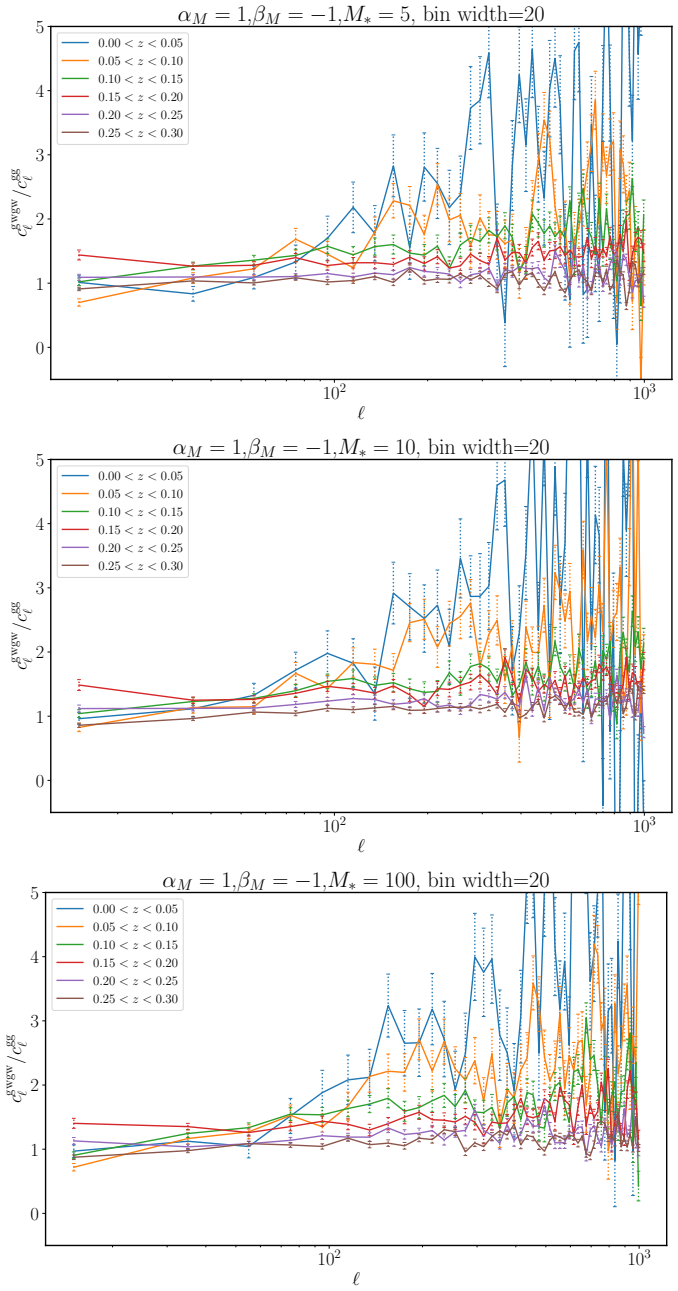

Figure 5.27: The bin averaged bias parameter comparison for GW sirens selected using stellar mass with different mass $M_* = 5,\ 10,\ 100 \times 10^{10} M_\odot$ in 6 different redshift bins. α, β are parameters in Eq.(5.17). Error bars are theoretically calculated using (5.27), using the analytic Gaussian covariance for the angular power spectrum and Taylor series error propagation.

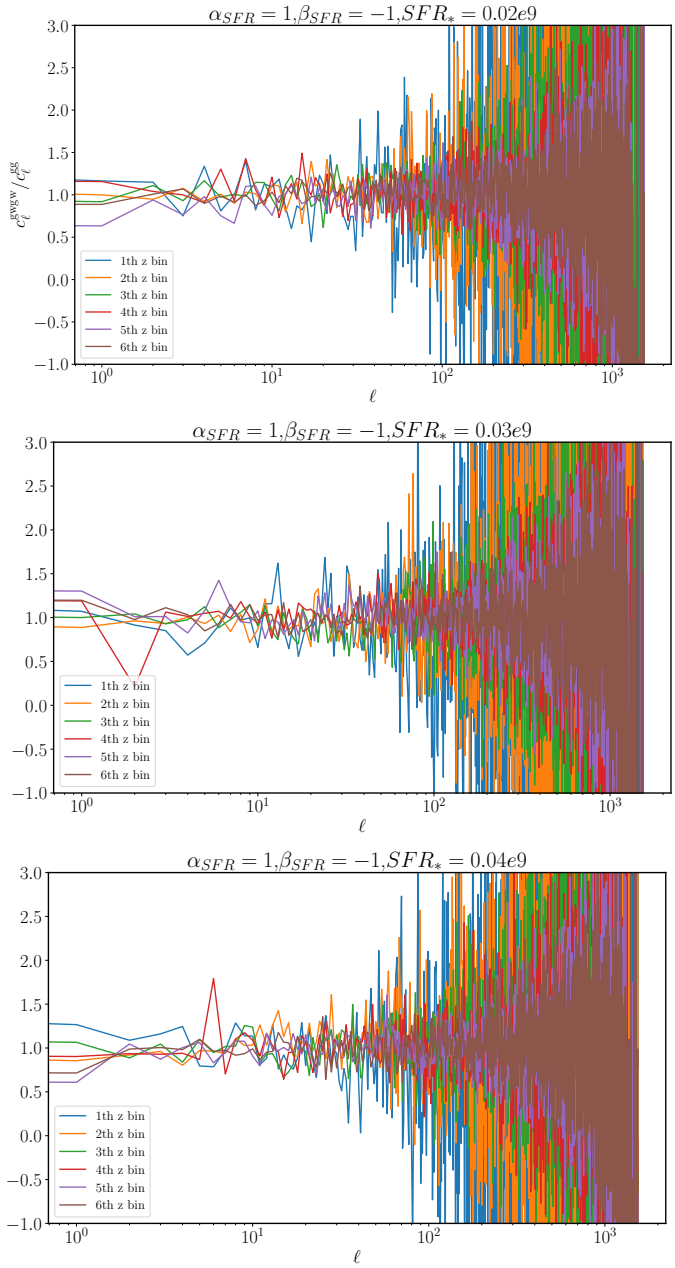

Figure 5.28: Bias Parameter comparison for GW sirens selected using star formation rate, with different star formation rate density $SFR_* = 0.02, 0.03, 0.04 \times 10^{10}\ M_\odot\ \mathrm{yr}^{-1}\ \mathrm{Mpc}^{-3}$ in 6 different redshift bins. α, β are parameters in Eq. (5.17).

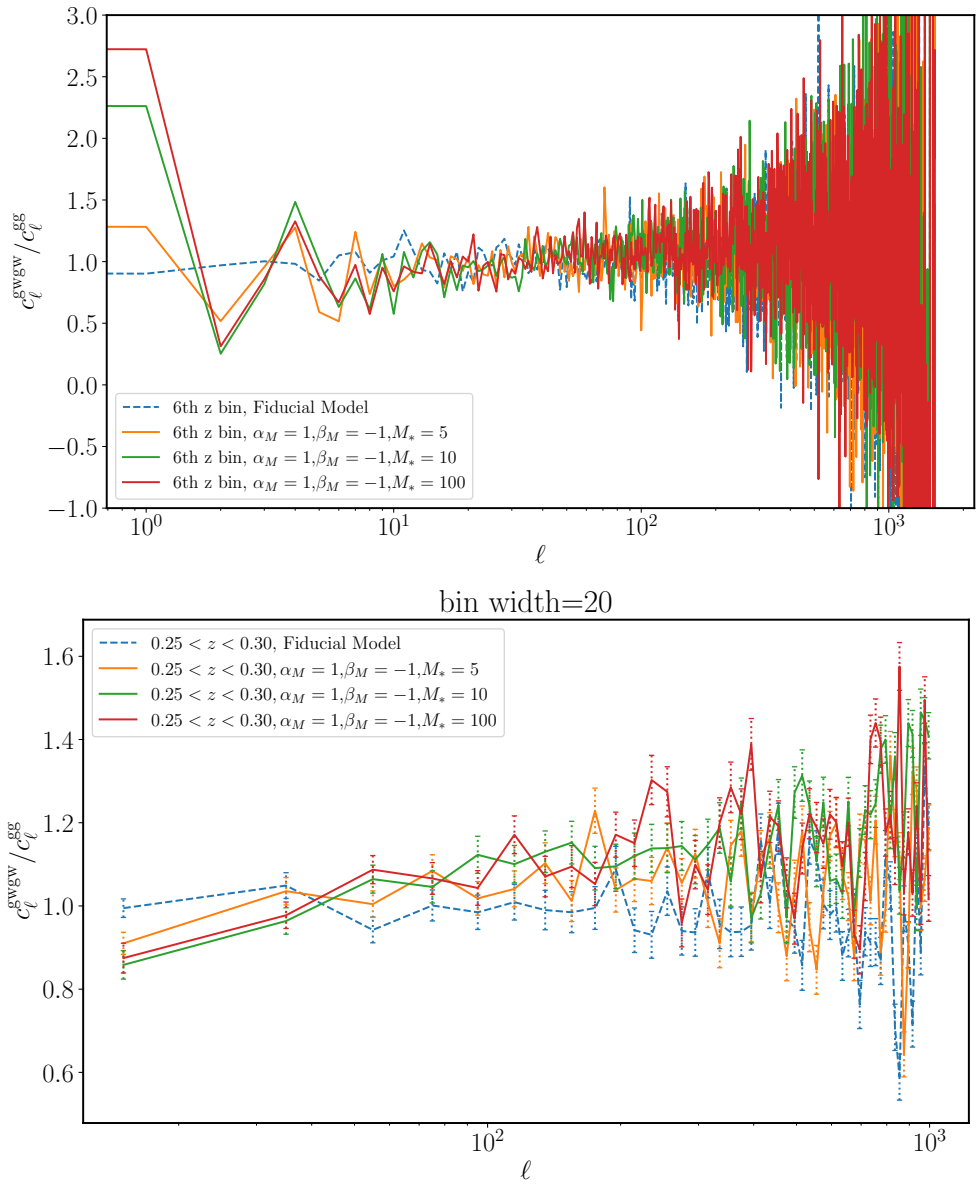

Figure 5.29: The top plot displays dependence of angular GW bias on varying M_* in the 6th redshift bin ($0.25 \leq z \leq 0.3$). The values of the parameters controlling the selection function for M_* are set as $\alpha_M = 1$ and $\beta_M = -1$ Eq.(5.17).The bottom plot displays the bin-averaged version of the top plot. Error bars are theoretically calculated using (5.27).

5.5 Modeling GW Bias based on 3 Dimensional Power Spectra through SDSS DR7

In this section, we will present theoretical modeling of the GW bias for 3D power Spectra. We calculate 3D power spectrum (for both galaxies and sirens with shot-noise subtraction) and bias parameter for SDSS DR7 catalog.

5.5.1 3D Power Spectrum

The redshift and angular position of observed galaxies are provided in a redshift survey. The redshift is directly related to the galaxy's radial distance linearly, using the Hubble's law at low redshift, and using the co-moving distance Eq. (2.34) at high redshift. Therefore, if we measure galaxies' redshifts, we can measure their clustering in three dimensions. Redshifts are recession velocities and contain both a cosmological component from the expansion of the Universe and a peculiar velocity component (from large-scale radial velocities induced by the matter distribution). Since velocities are correlated with densities, galaxy clustering along the redshift-space direction will be distorted, with the apparent density increased along the line of sight due to galaxies moving closer to an overdensity (see [41] for more details). This anisotropic clustering can be expressed as a function of wavenumber and angle, or by computing the multipoles of the galaxy power spectrum. Due to the reflection symmetry of the galaxies, only even multipoles survive; the monopole (P0) represents the spherically averaged part of the power spectrum, whereas the quadrupole (P2) and hexadecapole (P4) represent the redshift space distortion part. In this work, rather than using the multipoles, we use a spherically averaged power spectrum.

5.5.2 Gaussian Error Bar for Power Spectrum

We calculate errorbars analytically assuming Gaussian random field, neglecting the smaller contribution from the connected four-point function and super sample covariance [46]. Furthermore, we haven't included the effects of the window function. The Gaussian piece can be written as

$$C_{ij}^{G} = \frac{1}{V_w}\frac{2\pi}{V_{k_i}} 2P(k_i)^2 \delta_{ij}^{k}, \tag{5.29}$$

where k is the wave number, $P(k_i)$ is the power spectra, $V_{k_i} = 4\pi k_i^2 \delta k_i$, V_w is the survey volume and $\delta_{ij}^{k} = 1$ and δk_i is the bin width, if $k_i = k_j$ in the bin width. In the following

sections, we will use Eq.(5.29) for producing error bars corresponding to galaxy and siren power spectra. We have checked that these theoretical error bars agree with the jacknife error bars from Ross et al paper [59] within 20%. We measured error bars for the bias by creating 100 new samples of the sirens with different random seeds, and re-measuring the bias for each case. The error bars is the standard deviation of these 100 samples.

5.5.3 3D Power Spectrum for Sloan Digital Sky Survey (SDSS) Data Release 7

In this section, we will calculate 3 dimensional power spectrum for SDSS DR7 catalog. We consider all the cuts mentioned in Appendix.(A) except for the cuts on color information. We take the fiducial model to correspond to the parameters described in Table (5.4) for the rest of this section. Note that since the number of sirens are much fewer than galaxies in each bin for order of one year or even a decade of observing time, we multiply the number of sirens with amplitude=1000 or in other words take $T_{obs} = 10^3$years to obtain a meaningful theoretical prediction. We calculate the number of mergers in each redshift bin using Eq. (5.8) then we aim to populate the potential host galaxies with binary mergers using astrophysical properties such as metallicity, stellar mass and star formation rate (SFR) as mentioned in sections (5.2) and (5.3). Once again, we will first test the fiducial model with $\alpha,\ \beta = 0$ in Eq. (5.17), meaning assuming uniform distribution for selection of the GW hosts out of the galaxies in the survey. This will allow us to check and ensure that the code is working properly. Fig. (5.30) shows the 3D power spectrum for galaxies in redshift bin $0 < z \leq 0.1$. Table (5.3) shows the number of sirens in that redshift bin but in two mass bins. Note that, by mass bins we mean binning based on the chirp mass (4.20) which can be calculated using the masses of the two bodies in the binary. Fig. (5.31) shows the 3D power spectrum of the sirens in this redshift bin and the two different mass bins. Note that, the second mass bin is about two times larger than the first mass bin since for equal partition, number of sirens in the second mass bin will be much fewer than the first one and bias becomes more noisy consequently.

Redshift	Mass	Number of sirens
$0 < z \leq 0.1$	$4M_{\odot} \leq m_{ch} < 9M_{\odot}$	6085
$0 < z \leq 0.1$	$9M_{\odot} \leq m_{ch} < 34M_{\odot}$	2187

Table 5.3: Number of sirens in the redshift bin 0¡ z $\leq$ 0.1 for two mass bins (chirp mass). Note that since the number of sirens are much fewer than galaxies in each bin for order of one year or a decade of observing time, we multiply the number of sirens with amplitude=1000 or in other words take $T_{obs} = 10^3$years.

Model parameter	Value
z_{min}	0
z_{max}	0.2
T_{obs}	$10^3 yr$
$t_{d,min}$	500 Myr
number of redshift bins	2
number of mass bins	2
κ	1

Table 5.4: Parameter for fiducial model.

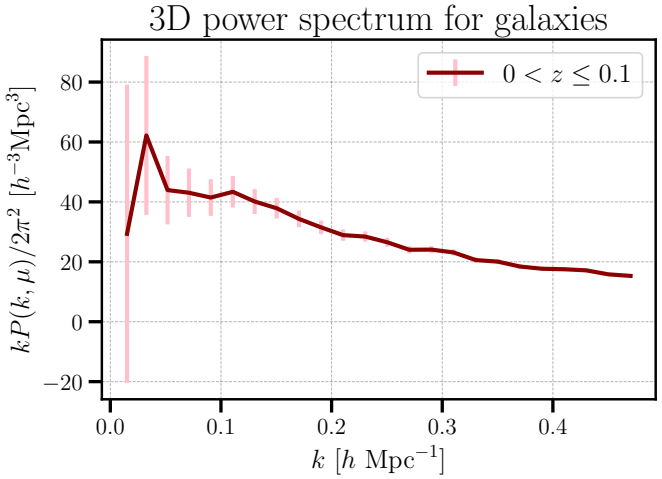

Figure 5.30: 3D power spectrum for galaxies in redshift bin $0 < z \leq 0.1$. The error bars are calculated by Eq.(5.29).

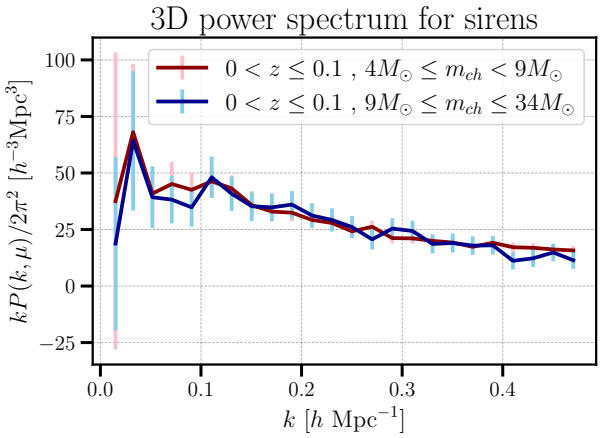

Figure 5.31: 3D power spectrum for sirens in redshift bin $0 < z \leq 0.1$ and mass bins ($4M_\odot \leq m_{ch} < 9M_\odot$, $9M_\odot \leq m_{ch} \leq 34M_\odot$). The error bars are calculated using Eq.(5.29). Random selection is used for choosing host galaxies.

Figure (5.32), displays the calculated estimate of the bias squared ratios in different mass bins in this redshift bin as function of scale. The difference from one is not statistically significant, as expected for random selection of host galaxies.

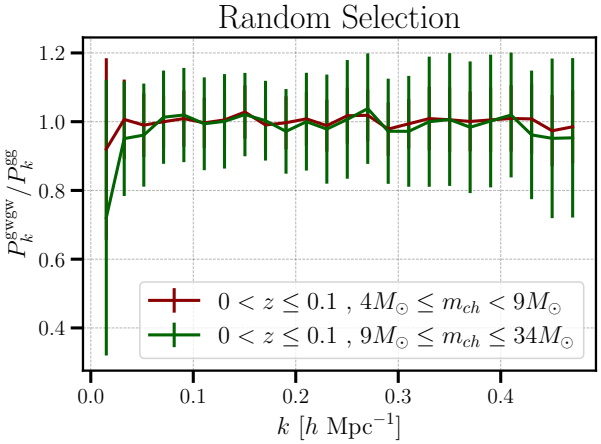

Figure 5.32: Bias parameter in redshift bin $0 < z \leq 0.1$ and mass bins ($4M_\odot \leq m_{ch} < 9M_\odot$, $9M_\odot \leq m_{ch} \leq 34M_\odot$). Random selection is used for choosing host galaxies.

Now we use the selection functions according to Eq.(5.17) to choose the host galaxies. Figure (5.33) shows the 3D power spectrum of sirens for the same redshift bin and mass bins as before but we have now set $\alpha_M = 1,\ \beta_M = -1$ and $M_* = (10,\ 56) \times 10^{10} M_\odot$. This means we are sampling the host galaxies based on their masses and specially from more massive galaxies in the survey but we are considering uniform distribution on SFR and metallicity. Figure (5.34) shows the resulting impact on the siren bias compared to the galaxy bias. It is evident that the bias deviates from one (corresponding to the random selection case) and it increases by enhancing the mass of the host galaxies. This means that the distribution of host galaxies is getting more clumped if we select more massive galaxies. These difference are statistically significant, especially once we average over k bins. The scatter in the bias is smaller than the size of the error bars which could be due to the covariance between the bins (due to the small k width of the bins compared to the scales couple by the window). Analyzing and understanding these errors further is also part of our follow up works. However, we can see that the bias is clearly deviating from 1 specially for $M_* = 56 \times 10^{10} M_\odot$. So that we can conclude that the theoretically GW bias can be a statistical indicative of mass properties of the host galaxies.

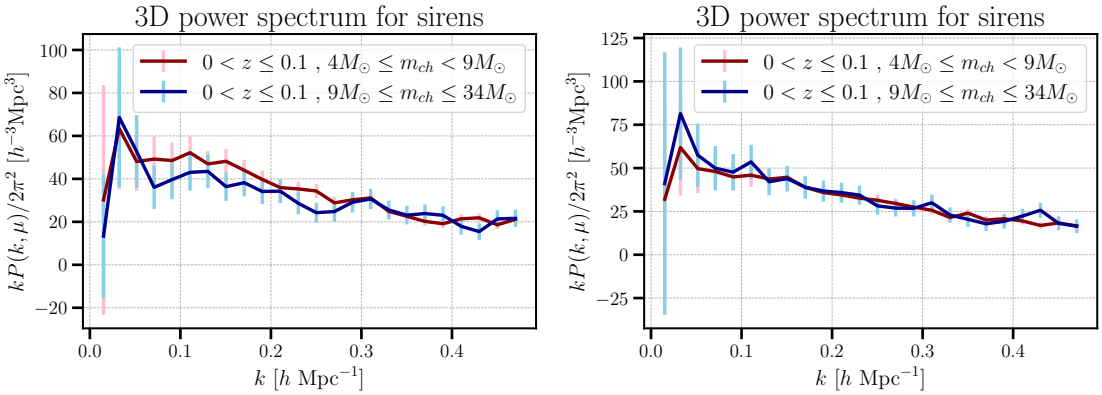

Figure 5.33: 3D power spectrum for sirens in redshift bin $0 < z \leq 0.1$ and mass bins $(4M_\odot \leq m_{ch} < 9M_\odot\ ,\ 9M_\odot \leq m_{ch} \leq 34M_\odot)$. The error bars are calculated by Eq. (5.29). Here we have considered $\alpha_M = 1,\ \beta_M = -1,\ M_* = 10 \times 10^{10} M_\odot$(right plot) and $M_* = 56 \times 10^{10} M_\odot$ (left plot) in Eq. (5.17).

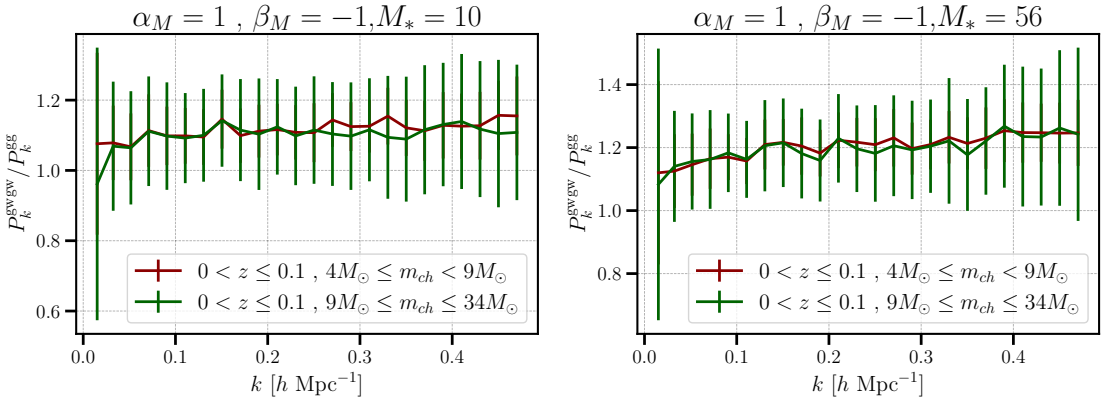

Figure 5.34: Bias parameter for redshift bin $0 < z \leq 0.1$ and mass bins ($4M_\odot \leq m_{ch} < 9M_\odot$, $9M_\odot \leq m_{ch} \leq 34M_\odot$). Here we considered $\alpha_M = 1, \beta_M = -1$ and $M_* = (10, 56) \times 10^{10} M_\odot$ in Eq. (5.17).

Next, we turn on the SFR selection function using again Eq.(5.17) to choose host galaxies, while considering uniform distribution on mass and metallicity. Figure (5.35) shows the 3D power spectrum of sirens for same redshift bin and mass bins as before but we have now set $\alpha_{SFR} = 1$, $\beta_{SFR} = -1$, $SFR_* = 4 \times 10^{11}\ M_\odot\ \mathrm{yr}^{-1}\ \mathrm{Mpc}^{-3}$. Figure (5.36) displays the impact of SFR selection function on bias for host galaxies. We can observe that taking into account the one standard deviation error, bias equal to 1 is excluded for the SFR selected sample. In particular since the host galaxies are now taken from galaxies with lower SFR than the average (in our sample $\mathrm{SFR}_{ave} \sim 6 \times 10^{11}\ M_\odot\ \mathrm{yr}^{-1}\ \mathrm{Mpc}^{-3}$) they are more clustered than the random selection case.
We will end this chapter by noting that in principle as discussed before, one can use joint probabilities and vary both SFR and mass which together with the scale dependence of bias can break the degeneracy for their impact on clustering of the host galaxies.

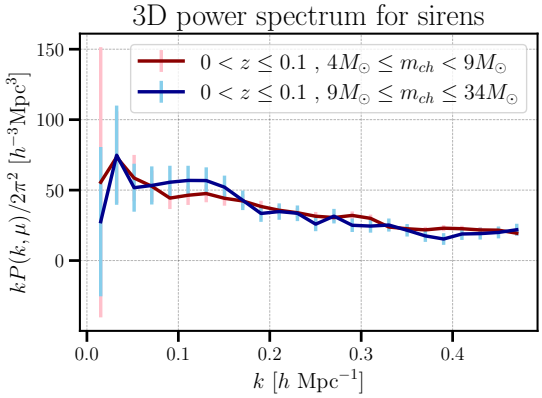

Figure 5.35: 3D power spectrum for sirens in redshift bin $0 < z \leq 0.1$ and mass bins ($4M_\odot \leq m_{ch} < 9M_\odot$, $9M_\odot \leq m_{ch} \leq 34M_\odot$). The error bars are calculated by Eq. (5.29). Here we considered $\alpha_{SFR} = 1, \beta_{SFR} = -1, SFR_* = 4 \times 10^{11}\ M_\odot\ \mathrm{yr}^{-1}\ \mathrm{Mpc}^{-3}$ in Eq. (5.17).

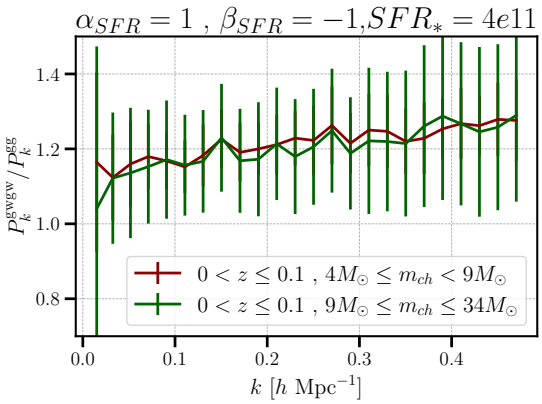

Figure 5.36: Bias parameter for redshift bin $0 < z \leq 0.1$ and mass bins ($4M_\odot \leq m_{ch} < 9M_\odot$, $9M_\odot \leq m_{ch} \leq 34M_\odot$). Here we considered $\alpha_{SFR} = 1, \beta_{SFR} = -1, SFR_* = 4 \times 10^{11}\ M_\odot\ \mathrm{yr}^{-1}\ \mathrm{Mpc}^{-3}$ in Eq. (5.17).

Chapter 6

Conclusion

In this thesis, I briefly reviewed the theory of standard cosmology and the bases of the general theory of relativity needed to describe the background evolution of cosmose in chapter (2). I then moved on to introduce some important concepts in theory of large scale structure and statistical cosmology such as power spectrum and bias parameter in chapter (3). In chapter (4), I presented the primer to physics and observational status of Gravitational Waves from Merging Compact Binaries.
Chapter (5), summarizes my research contribution during my master's program which aimed at constructing a framework for making theoretical prediction of the GW bias parameter for different choices of galaxy properties using both Spec-z and Photo-z galaxy catalogs. We investigated the effect of astrophysical models on properties of GWsources as tracers of galaxy populations. We first explored how one can model the mass distributions and redshift dependence of GW sources based on their merger rate. We then studied how different astrophysical properties of galaxies (such as metallicity, mass and star formation rate density) can affect their probability to be host of a merger event. Finally we put forward computational scheme to calculate the dependence of the angular and 3-dimensional power spectra of GWs and the corresponding bias parameters to the parameters of these models. Our work is currently tailored for observed galaxy population in GLADE+ and Sloan Digital Sky Survey Data (SDSS) Release 7 catalogs but it is easily extendable to other catalogs. Note that this work is just one part in a more ambitious program of using the upcoming GWs data and galaxy surveys in a meaningful way to infer cosmological and astrophysical parameters. After numerous sanity tests, our result in chapter (5) show that our codes are all working and communicating well. In fact, we have some preliminary results that indicate how astrophysical parameters such as mass and SFR of host galaxies can systematically affect the bias parameter. As can be seen in chapter (5), if we increase

the mass of GW event host galaxies or decrease their SFR, the bias increases and deviates from one (expected to be one for random selection case) which agrees with host galaxies being more clustered in these cases than the case of random selection. More over the scale dependence of bias can distinguish between these two effects. Our code is easily extendable to different prescriptions for populating the GW host galaxies.
In this research, the following two different galaxy catalogs were used:

- GLADE+ which does not include SFR and color information (metallicity) of galaxies. In this case we used best-fit models to compute them. 2D angular power spectrum and bias parameter are presented in chapter (5). The result indicated some dependency between bias and the available astrophysical property namely mass. However, we need to construct more realistic models to test the connection between galaxies and binaries.
- SDSS ER7 catalog has all the necessary astrophysical properties. Our result at this point shows how clustering of host galaxies impacts the GW bias parameter for 3D power spectrum.

Future works can be summarized as following:

- Exploring different assumptions in the astrophysical modelling of the binary synthesis module and selection function.
- Exploring the impact of BBH masses on the hosts astrophysical properties and how it will impact GW bias.
- One long-term objective can be once GW bias is better understood it can be used to optimise the statistical inference cosmological parameters such as H_0 based on cross correlation of sirens and galaxy surveys.
- Exploration of the GW bias parameter for different galaxy completeness scenarios.
- Measurability of the signal from current and the next generation GW detectors.
- Comparison of the GW bias parameters for Primordial BHs and Astrophysical BHs.

References

[1] Astropy. https://www.astropy.org/.

[2] First observation of gravitational waves. https://en.wikipedia.org/wiki/First_observation_of_gravitational_waves.

[3] Gravitational wave. https://en.wikipedia.org/wiki/Gravitational_wave.

[4] Healpy. https://healpy.readthedocs.io/en/latest/tutorial.html.

[5] Life cycle of a star. https://www.schoolsobservatory.org/learn/astro/stars/cycle.

[6] Ligo-india. http://www.gw-indigo.org/tiki-index.php?page=LIGO-India.

[7] Nbodykit. https://nbodykit.readthedocs.io/en/latest/getting-started/install.html.

[8] Numpy. https://numpy.org/doc/.

[9] Scipy. https://docs.scipy.org/doc/scipy/.

[10] B. P. Abbott, R. Abbott, T. D. Abbott et al., The LIGO Scientific Collaboration, and the Virgo Collaboration. Binary black hole population properties inferred from the first and second observing runs of advanced ligo and advanced virgo. *The Astrophysical Journal Letters*, 882(2):L24, sep 2019.

[11] B. P. Abbott, R. Abbott, and T. D. Abbott et al. Observation of gravitational waves from a binary black hole merger. *Physical Review Letters*, 116(6), feb 2016.

[12] R. Abbott, T. D. Abbott, S. Abraham et al., The LIGO Scientific Collaboration, and the Virgo Collaboration. Population properties of compact objects from the second ligo–virgo gravitational-wave transient catalog. *The Astrophysical Journal Letters*, 913(1):L7, may 2021.

[13] N. Aghanim, Y. Akrami, and M. Ashdown et al. iplanck/i 2018 results. *Astronomy &amp Astrophysics*, 641:A6, sep 2020.

[14] Simone Aiola and Calabrese et al. The Atacama Cosmology Telescope: DR4 maps and cosmological parameters. , 2020(12):047, December 2020.

[15] Daniel Baumann. *Cosmology*. SAO/NASA Astrophysics Data System, 2005.

[16] Peter Behroozi, Risa H Wechsler, Andrew P Hearin, and Charlie Conroy. UniverseMachine: The correlation between galaxy growth and dark matter halo assembly from z = 0–10. *Monthly Notices of the Royal Astronomical Society*, 488(3):3143–3194, 05 2019.

[17] Peter S. Behroozi, Charlie Conroy, and Risa H. Wechsler. A Comprehensive Analysis of Uncertainties Affecting the Stellar Mass-Halo Mass Relation for 0 ¡ z ¡ 4. , 717(1):379–403, July 2010.

[18] Angela M. Berti, Alison L. Coil, Andrew P. Hearin, and Peter S. Behroozi. Main-sequence scatter is real: The joint dependence of galaxy clustering on star formation and stellar mass. *The Astronomical Journal*, 161(1):49, dec 2020.

[19] Michael R. Blanton, David J. Schlegel, Michael A. Strauss, J. Brinkmann, Douglas Finkbeiner, Masataka Fukugita, James E. Gunn, David W. Hogg, Željko Ivezić, G. R. Knapp, Robert H. Lupton, Jeffrey A. Munn, Donald P. Schneider, Max Tegmark, and Idit Zehavi. New York University Value-Added Galaxy Catalog: A Galaxy Catalog Based on New Public Surveys. , 129(6):2562–2578, June 2005.

[20] I. Bombaci. The maximum mass of a neutron star. , 305:871, January 1996.

[21] Sean M. Carroll. Lecture notes on general relativity, 1997.

[22] Hsin-Yu Chen, Maya Fishbach, and Daniel E. Holz. A two per cent hubble constant measurement from standard sirens within five years. *Nature*, 562(7728):545–547, oct 2018.

[23] Alison L. Coil, Alexander J. Mendez, Daniel J. Eisenstein, and John Moustakas. PRIMUS+DEEP2: The Dependence of Galaxy Clustering on Stellar Mass and Specific Star Formation Rate at 0.2 ¡ z ¡ 1.2. , 838(2):87, April 2017.

[24] G. Dálya et al. GLADE+: An Extended Galaxy Catalogue for Multimessenger Searches with Advanced Gravitational-wave Detectors. 10 2021.

[25] Bernard F. Schutz Daniel E. Holz, Scott A. Hughes. Measuring cosmic distances with standard sirens. 8.

[26] Vincent Desjacques, Donghui Jeong, and Fabian Schmidt. Large-scale galaxy bias. *Physics Reports*, 733:1–193, feb 2018.

[27] A. Einstein and N. Rosen. On Gravitational Waves. *Journal of The Franklin Institute*, 223:43–54, January 1937.

[28] Albert Einstein. Näherungsweise Integration der Feldgleichungen der Gravitation. *Sitzungsberichte der Königlich Preussischen Akademie der Wissenschaften*, pages 688–696, January 1916.

[29] Albert Einstein. Über Gravitationswellen. *Sitzungsberichte der Königlich Preussischen Akademie der Wissenschaften*, pages 154–167, January 1918.

[30] R. Farmer, M. Renzo, S. E. de Mink, P. Marchant, and S. Justham. Mind the gap: The location of the lower edge of the pair-instability supernova black hole mass gap. *The Astrophysical Journal*, 887(1):53, dec 2019.

[31] Rodrigo Fernández, Eliot Quataert, Kazumi Kashiyama, and Eric R Coughlin. Mass ejection in failed supernovae: variation with stellar progenitor. *Monthly Notices of the Royal Astronomical Society*, 476(2):2366–2383, 2018.

[32] Dave Finley. "einstein's gravity theory passes toughest test yet: Bizarre binary star system pushes study of relativity to new limits".

[33] Éanna É. Flanagan and Scott A. Hughes. The basics of gravitational wave theory. *New Journal of Physics*, 7(1):204, September 2005.

[34] J. N. Fry and Enrique Gaztanaga. Biasing and Hierarchical Statistics in Large-Scale Structure. , 413:447, August 1993.

[35] K. M. Gorski, E. Hivon, A. J. Banday, B. D. Wandelt, F. K. Hansen, M. Reinecke, and M. Bartelmann. HEALPix: A framework for high-resolution discretization and fast analysis of data distributed on the sphere. *The Astrophysical Journal*, 622(2):759–771, apr 2005.

[36] Alan Heavens. Statistical techniques in cosmology, 2009.

[37] Daniel E. Holz, Scott A. Hughes, and Bernard F. Schutz. Measuring cosmic distances with standard sirens. *Physics Today*, 2018.

[38] Robert Hurt. Gravitational wave international committee, 2021.

[39] Dragan Huterer. Lecture notes on structure formation in the universe, 2020.

[40] Mario Ivanov and Rodrigo Ferná ndez. Mass ejection in failed supernovae: Equation of state and neutrino loss dependence. *The Astrophysical Journal*, 911(1):6, apr 2021.

[41] Nick Kaiser. Clustering in real space and in redshift space. , 227:1–21, July 1987.

[42] Christos Karathanasis, Suvodip Mukherjee, and Simone Mastrogiovanni. Binary black holes population and cosmology in new lights: Signature of PISN mass and formation channel in GWTC-3. *arXiv e-prints*, page arXiv:2204.13495, April 2022.

[43] Jungjoon Leo Kim. Spectrum of cuscuton bounce and cosmological parameter inference using dark sirens.

[44] Pavel Kroupa. On the variation of the initial mass function. *Monthly Notices of the Royal Astronomical Society*, 322(2):231–246, 04 2001.

[45] M.Evans P. Fritschel L. Barsotti, L. McCuller. The a+ design curve, 2019.

[46] Yin Li, Wayne Hu, and Masahiro Takada. Super-sample covariance in simulations. *Phys. Rev. D*, 89:083519, Apr 2014.

[47] Piero Madau and Mark Dickinson. Cosmic star-formation history. *Annual Review of Astronomy and Astrophysics*, 52(1):415–486, aug 2014.

[48] F. Marulli, M. Bolzonella, E. Branchini, I. Davidzon, S. de la Torre, B. R. Granett, L. Guzzo, A. Iovino, L. Moscardini, A. Pollo, U. Abbas, C. Adami, S. Arnouts, J. Bel, D. Bottini, A. Cappi, J. Coupon, O. Cucciati, G. De Lucia, A. Fritz, P. Franzetti, M. Fumana, B. Garilli, O. Ilbert, J. Krywult, V. Le Brun, O. Le Fèvre, D. Maccagni, K. Małek, H. J. McCracken, L. Paioro, M. Polletta, H. Schlagenhaufer, M. Scodeggio, L. A. M. Tasca, R. Tojeiro, D. Vergani, A. Zanichelli, A. Burden, C. Di Porto, A. Marchetti, C. Marinoni, Y. Mellier, R. C. Nichol, J. A. Peacock, W. J. Percival, S. Phleps, M. Wolk, and G. Zamorani. The VIMOS Public Extragalactic Redshift Survey (VIPERS) . Luminosity and stellar mass dependence of galaxy clustering at 0.5 ¡ z ¡ 1.1. , 557:A17, September 2013.

[49] M. R. Mokiem, A. de Koter, J. S. Vink, J. Puls, C. J. Evans, S. J. Smartt, P. A. Crowther, A. Herrero, N. Langer, D. J. Lennon, F. Najarro, and M. R. Villamariz. The empirical metallicity dependence of the mass-loss rate of O- and early B-type stars. , 473(2):603–614, October 2007.

[50] Suvodip Mukherjee. The redshift dependence of black hole mass distribution: is it reliable for standard sirens cosmology? *Monthly Notices of the Royal Astronomical Society*, 515(4):5495–5505, aug 2022.

[51] Suvodip Mukherjee, Tom Broadhurst, Jose M Diego, Joseph Silk, and George F Smoot. Impact of astrophysical binary coalescence time-scales on the rate of lensed gravitational wave events. *Monthly Notices of the Royal Astronomical Society*, 506(3):3751–3759, 07 2021.

[52] Suvodip Mukherjee and Azadeh Moradinezhad Dizgah. Toward a precision measurement of binary black holes formation channels using gravitational waves and emission lines. *The Astrophysical Journal Letters*, 937(2):L27, sep 2022.

[53] Will J. Percival. Large scale structure observations, 2013.

[54] H. Poincaré. Note de h. poincaré. c.r. t.140 1504-1508, 1905.

[55] M Punturo, M Abernathy, F Acernese, B Allen, N Andersson, K Arun, F Barone, B Barr, M Barsuglia, M Beker, N Beveridge, S Birindelli, S Bose, L Bosi, S Braccini, C Bradaschia, T Bulik, E Calloni, G Cella, E Chassande Mottin, S Chelkowski, A Chincarini, J Clark, E Coccia, C Colacino, J Colas, A Cumming, L Cunningham, E Cuoco, S Danilishin, K Danzmann, G De Luca, R De Salvo, T Dent, R De Rosa, L Di Fiore, A Di Virgilio, M Doets, V Fafone, P Falferi, R Flaminio, J Franc, F Frasconi, A Freise, P Fulda, J Gair, G Gemme, A Gennai, A Giazotto, K Glampedakis, M Granata, H Grote, G Guidi, G Hammond, M Hannam, J Harms, D Heinert, M Hendry, I Heng, E Hennes, S Hild, J Hough, S Husa, S Huttner, G Jones, F Khalili, K Kokeyama, K Kokkotas, B Krishnan, M Lorenzini, H Lück, E Majorana, I Mandel, V Mandic, I Martin, C Michel, Y Minenkov, N Morgado, S Mosca, B Mours, H Müller–Ebhardt, P Murray, R Nawrodt, J Nelson, R Oshaughnessy, C D Ott, C Palomba, A Paoli, G Parguez, A Pasqualetti, R Passaquieti, D Passuello, L Pinard, R Poggiani, P Popolizio, M Prato, P Puppo, D Rabeling, P Rapagnani, J Read, T Regimbau, H Rehbein, S Reid, L Rezzolla, F Ricci, F Richard, A Rocchi, S Rowan, A Rüdiger, B Sassolas, B Sathyaprakash, R Schnabel, C Schwarz, P Seidel, A Sintes, K Somiya, F Speirits, K Strain, S Strigin, P Sutton, S Tarabrin, A Thüring, J van den Brand, C van Leewen, M van Veggel, C van den Broeck, A Vecchio, J Veitch, F Vetrano, A Vicere, S Vyatchanin, B Willke, G Woan, P Wolfango, and K Yamamoto. The einstein telescope: a third-generation gravitational wave observatory. *Classical and Quantum Gravity*, 27(19):194002, sep 2010.

[56] David Reitze. The future of ground-based gravitational-wave detectors, 2018.

[57] David Reitze, Rana X Adhikari, Stefan Ballmer, Barry Barish, Lisa Barsotti, Gari-Lynn Billingsley, Duncan A. Brown, Yanbei Chen, Dennis Coyne, Robert Eisenstein, Matthew Evans, Peter Fritschel, Evan D. Hall, Albert Lazzarini, Geoffrey Lovelace, Jocelyn Read, B. S. Sathyaprakash, David Shoemaker, Joshua Smith, Calum Torrie, Salvatore Vitale, Rainer Weiss, Christopher Wipf, and Michael Zucker. Cosmic explorer: The u.s. contribution to gravitational-wave astronomy beyond ligo. 2019.

[58] Adam G. Riess, Stefano Casertano, Wenlong Yuan, J. Bradley Bowers, Lucas Macri, Joel C. Zinn, and Dan Scolnic. Cosmic distances calibrated to 1% precision with gaia EDR3 parallaxes and hubble space telescope photometry of 75 milky way cepheids confirm tension with {*upLambda*CDM. *The Astrophysical Journal Letters*, 908(1):L6, feb 2021.

[59] Ashley J. Ross, Lado Samushia, Cullan Howlett, Will J. Percival, Angela Burden, and Marc Manera. The clustering of the SDSS DR7 main Galaxy sample – I. A 4 per cent distance measure at z = 0.15. *Monthly Notices of the Royal Astronomical Society*, 449(1):835–847, 03 2015.

[60] B. S. Sathyaprakash and Bernard F. Schutz. Physics, astrophysics and cosmology with gravitational waves. *Living Reviews in Relativity*, 12.

[61] American Scientist. "the secret history of gravitational waves".

[62] M. Soares-Santos, Holz et al., Dark Energy Survey, and Dark Energy Camera GW-EM Collaboration. The Electromagnetic Counterpart of the Binary Neutron Star Merger LIGO/Virgo GW170817. I. Discovery of the Optical Counterpart Using the Dark Energy Camera. , 848(2):L16, October 2017.

[63] S.Weinberg. *Cosmology*. 2008.

[64] The LIGO Scientific Collaboration, The Virgo Collaboration, The KAGRA Collaboration, R. Abbott, and H et al. Abe. Constraints on the cosmic expansion history from gwtc-3, 2021.

[65] The LIGO Scientific Collaboration, The Virgo Collaboration, The KAGRA Collaboration, and R. et al. Abbott. The population of merging compact binaries inferred using gravitational waves through gwtc-3, 2021.

[66] Daichi Tsuna. Failed supernova remnants. 73(3):L6–L11, 2021.

[67] Eleonora Di Valentino, Olga Mena, Supriya Pan, Luca Visinelli, Weiqiang Yang, Alessandro Melchiorri, David F Mota, Adam G Riess, and Joseph Silk. In the realm of the hubble tension a review of solutions. 38(15):153001, jul 2021.

[68] L. Verde. Statistical methods in cosmology. In *Lectures on Cosmology*, pages 147–177. Springer Berlin Heidelberg, 2010.

[69] Salvatore Vitale. on behalf of the cosmic explorer project team, 2021.

[70] Anna K. Weigel, Kevin Schawinski, and Claudio Bruderer. Stellar mass functions: methods, systematics and results for the local universe. *Monthly Notices of the Royal Astronomical Society*, 459(2):2150–2187, apr 2016.

[71] Idit Zehavi, Zheng Zheng, David H. Weinberg, Michael R. Blanton, Neta A. Bahcall, Andreas A. Berlind, Jon Brinkmann, Joshua A. Frieman, James E. Gunn, Robert H. Lupton, Robert C. Nichol, Will J. Percival, Donald P. Schneider, Ramin A. Skibba, Michael A. Strauss, Max Tegmark, and Donald G. York. Galaxy Clustering in the Completed SDSS Redshift Survey: The Dependence on Color and Luminosity. , 736(1):59, July 2011.

APPENDIX

Appendix A

Catalogs

A.1 GLADE+ catalog

GLADE+ is an expanded version of the GLADE galaxy survey designed for multi-messenger probes with gravitational-wave detectors. GLADE+ includes data from six distinct but interconnected astronomical catalogues namely, GWGC, 2MPZ, 2MASS XSC, HyperLEDA, and WISExSCOSPZ, and the SDSS-DR16Q. About 22.5 million galaxies and 750,000 quasars are included in GLADE+. As can be seen if fig. A.1, the completeness of GLADE+ is until luminosity distances of about 47 Mpc (by integrating the galaxies' B-band luminosity). To compare with GW detectors, the maximum BNS detection range for the fourth observing run of LIGO (O4) (for BNSs with masses about $1.4M_{\odot}$ with signal-to-noise ratio about 8) is about $190Mpc$ so that GLADE+ is about 45 percent complete in this areas. It contains location information of galaxies such as right ascension (ra), declination (dec), luminosity distance (D_L) and redshift (z). GLADE+ also reports some colour information and other quantities discussed in detail in the official GLADE+ website[1]. Fig. A.4 shows some columns of the GLADE+ catalog that are used in our work. The figure shows the mollweide projection(using mollview from healpy package in python) which visualizes related HEALPix maps (ref. [24]). NSIDE is also defining the resolution of the map.[2]

[1] At http://glade.elte.hu/.

[2] For more information about the HEALPix map and Mollview map see the official healpy website at https://healpy.readthedocs.io/en/latest/.

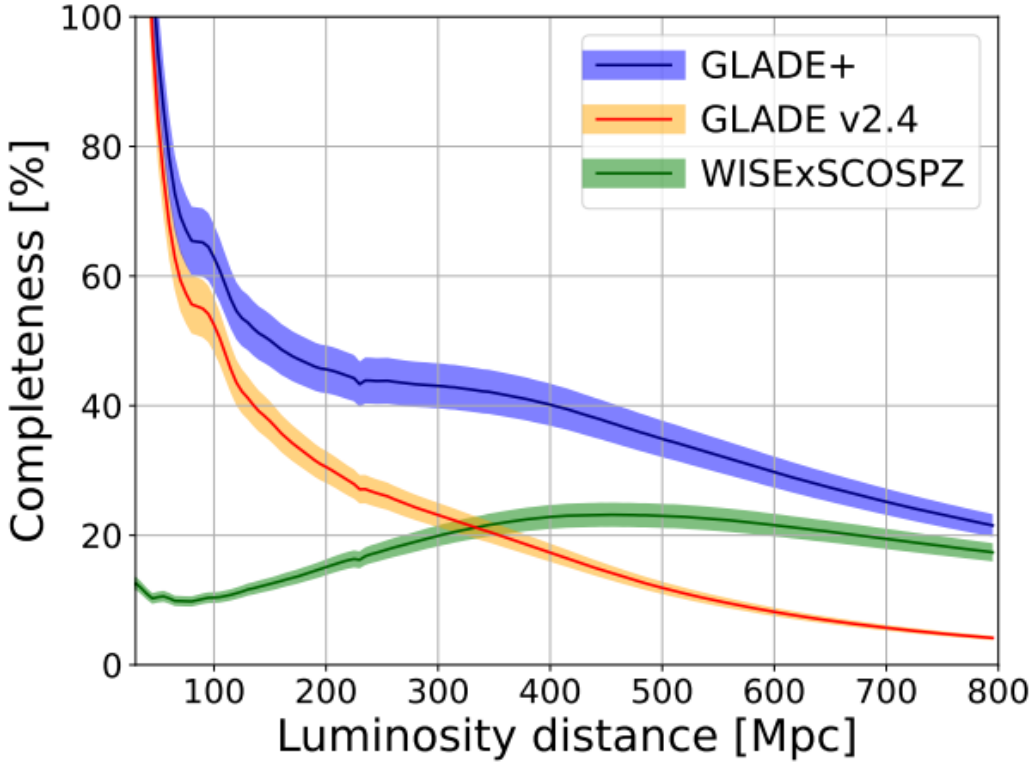

Figure A.1: GLADE+ completeness (ref. [24]).

	GWGC	Hyp	2MASS	wiseX	SDSS-DR16Q	type	ra	dec	B magnitude	H magnitude	z	D_L	M
0	NGC4736	NGC4736	12505314+4107125	J125053.14+410712.7	NaN	G	192.721451	41.120152	-19.4135	5.418	0.001733	4.392418	NaN
1	NGC4548	NGC4548	12352642+1429467	J123526.45+142946.9	NaN	G	188.860123	14.496320	-20.1537	7.600	0.003573	15.876007	0.20
2	NGC6503	NGC6503	17492651+7008396	J174926.45+700840.8	NaN	G	267.360474	70.144341	-20.1953	7.615	0.002803	12.446600	NaN
3	NGC4442	NGC4442	12280389+0948130	J122803.90+094813.3	NaN	G	187.016220	9.803620	-19.0062	7.593	0.002582	11.461371	0.09
4	NGC4469	NGC4469	NaN	J122928.05+084500.8	NaN	G	187.367000	8.749890	-18.5065	NaN	0.003417	15.180920	0.10
...	...	...	...	...	...	...	...	...	...	...	...	...	...
23181753	NaN	NaN	NaN	NaN	235959.78+285717	Q	359.999118	28.954734	NaN	NaN	2.447875	20403.464630	NaN
23181754	NaN	NaN	NaN	NaN	235959.83+344315	Q	359.999303	34.720842	NaN	NaN	3.103939	27158.368406	NaN
23181755	NaN	NaN	NaN	NaN	235959.90+031606.9	Q	359.999615	3.268586	NaN	NaN	1.230502	8792.439985	NaN
23181756	NaN	NaN	NaN	NaN	235959.94+204315.8	Q	359.999759	20.721079	NaN	NaN	2.006303	16022.500633	NaN
23181757	NaN	NaN	NaN	NaN	235959.98+344449.6	Q	359.999954	34.747133	NaN	NaN	2.371187	19629.730536	NaN

Figure A.2: GLADE+ catalog of about 23 million galaxies. Adopted from http://glade.elte.hu/

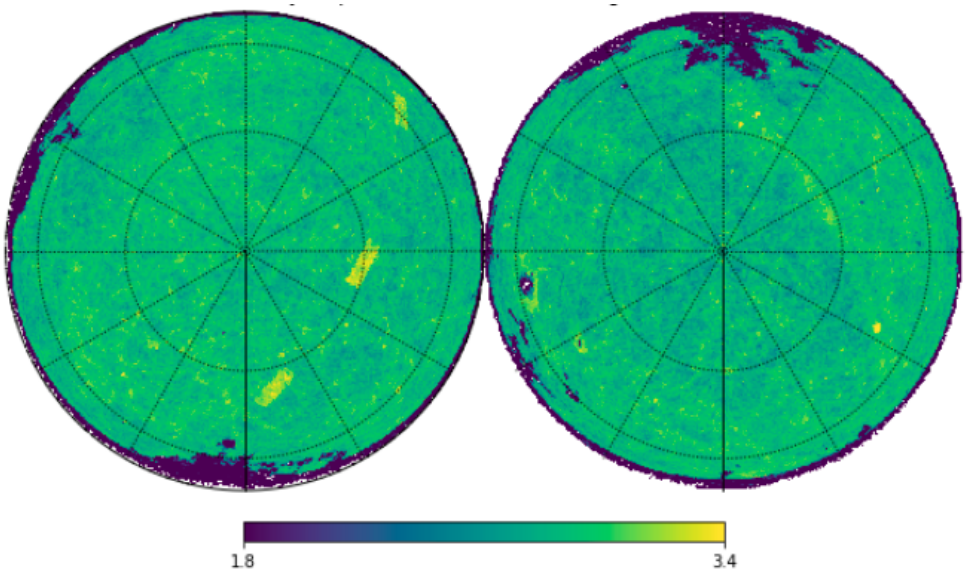

Figure A.3: The log mollview map of galaxies in the GLADE+ catalog with Nside=128.

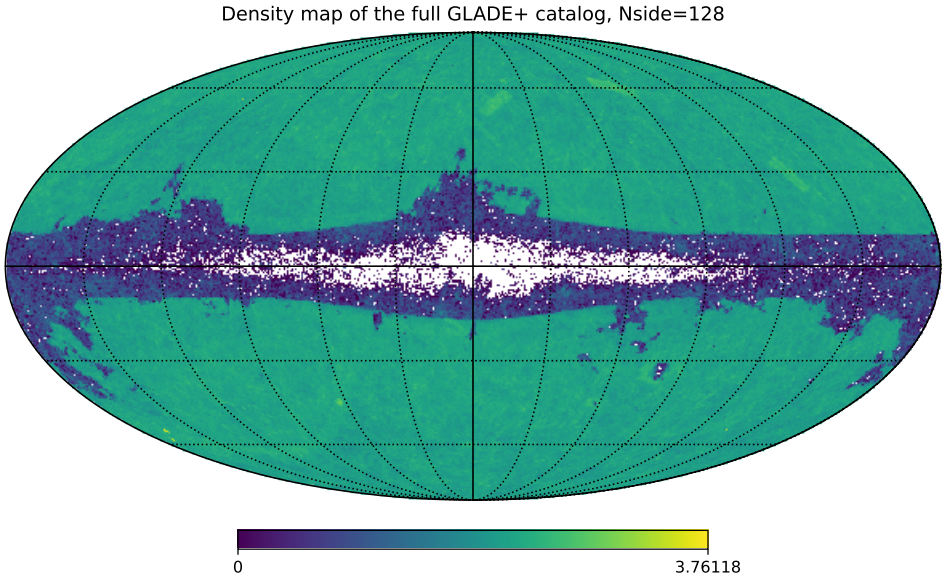

Figure A.4: The mollview map of galaxies in the GLADE+ catalog with Nside=128.

A.2 Sloan Digital Sky Survey (SDSS) Data Release 7

New York University Value-Added Galaxy Catalog (NYU-VAGC) is a collection of galaxy catalogs that can be used to compute power spectra and correlation functions. A catalog of galaxies with the maximum of $z = 0.3$ compiled from surveys that have been made publicly available and accommodate to the Sloan Digital Sky Survey (SDSS) Data Release 2 with about 693,319 galaxies, QSOs, and stars in the photometric catalog; of these, 343,568 have redshift measurements from the SDSS. Except regions obscured by bright stars, the photometric sample encompasses 3514 deg^2, and the spectroscopic sample encompasses 2627 deg^2 (with the completeness of approximately 85%) (ref. [19]).
The SDSS DR7 includes the SDSS-I and SDSS-II full data sets. In these surveys, CCD photometry field (Gunn et al. 1998, 2006) was obtained in five bands (u, g, r, i, z), calibrated utilizing the "uber-calibration" method (Padmanabhan et al. (2008)), Creating an overall area of $11,663$ deg^2. From this data set, galaxies with a footprint of 9380 deg^2(Abazajian et al. 2009) were chosen as the main galaxy sample (MGS; Strauss) for spectroscopic follow-up which roughly includes every galaxy with the extinction-corrected r-band Petrosian magnitude (r_{pet}) smaller than 17.77, in other words, the magnitude sample of SDSS is complete up to $r = 17.77$ [59]. So that, the sample is complete to stellar mass 10^9 at $z = 0.02$ and 10^{10} at $z = 0.06$ (see fig. A.5). we can extrapolate the limiting mass using the luminosity distance. In ref. [70], Weigel et al define the limiting mass as the stellar mass corresponding to the faintest galaxy in the sample. Since stellar mass is proportional to luminosity, they are computing the luminosity of the faintest galaxy in the sample. At fixed apparently magnitude, going to higher redshift means that the least massive/luminous galaxy is more massive/luminous. The mass/luminosity scales as luminosity distance squared. Now we can calculate [3] $D_l = 988Mpc$ at $z = 0.2$ and $D_l = 270Mpc$ at $z = 0.06$ (scaling by a factor of 13). So that is a minimum log stellar mass of 11.3 (scaling the log stellar mass of 10.2 at z=0.06 from Weigel et al [70]).
We acquired the SDSS DR7 MGS data from (NYU-VAGC) hosted by NYU. They consist of K-corrected absolute magnitudes, as calculated by the methods of Blanton et al (2003), and comprehensive mask information. We choose our galaxy sample from among the "safe" NYU-VAGC catalog. Fig. A.6, A.7 show the Mollview map which describe the number of galaxies in each pixel in the Celestial sphere in both Galactic and Equatorial plane. Table A.1 shows different columns in the 'safe0' file in the SDSS catalog (ref. [59]).

[3] Using this website: https://www.astro.ucla.edu/ wright/CosmoCalc.html

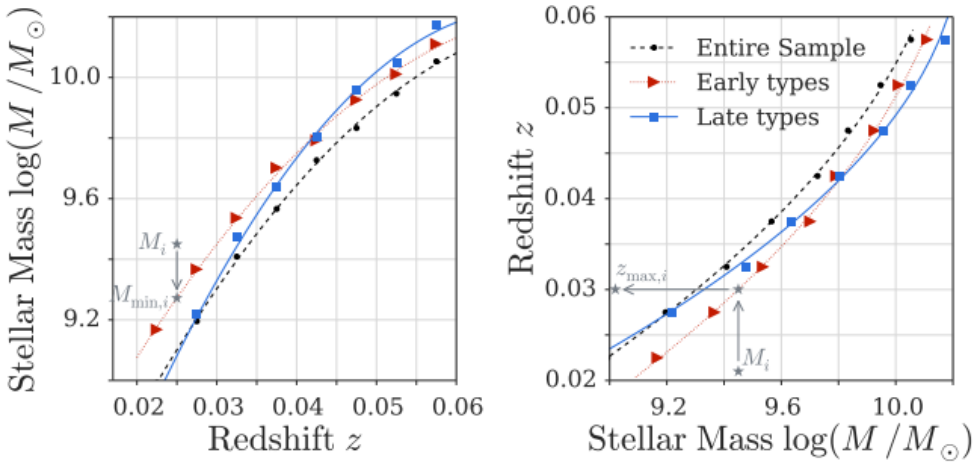

Figure A.5: Stellar mass completeness for three different samples(early, late and whole galaxies). For more information see ref [70].

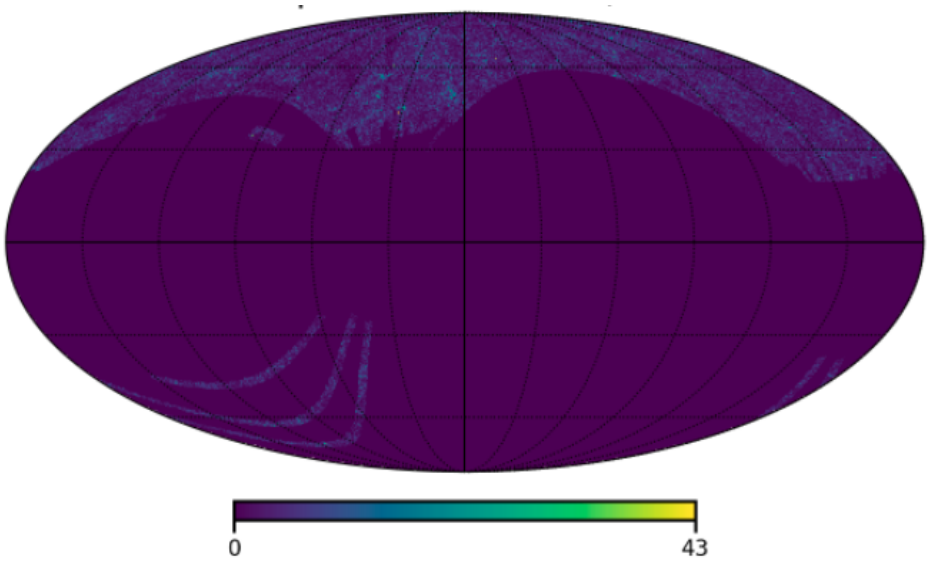

Figure A.6: The Mollview map of 'safe0' file from SDSS DR7 galaxy catalog with Nside=256.

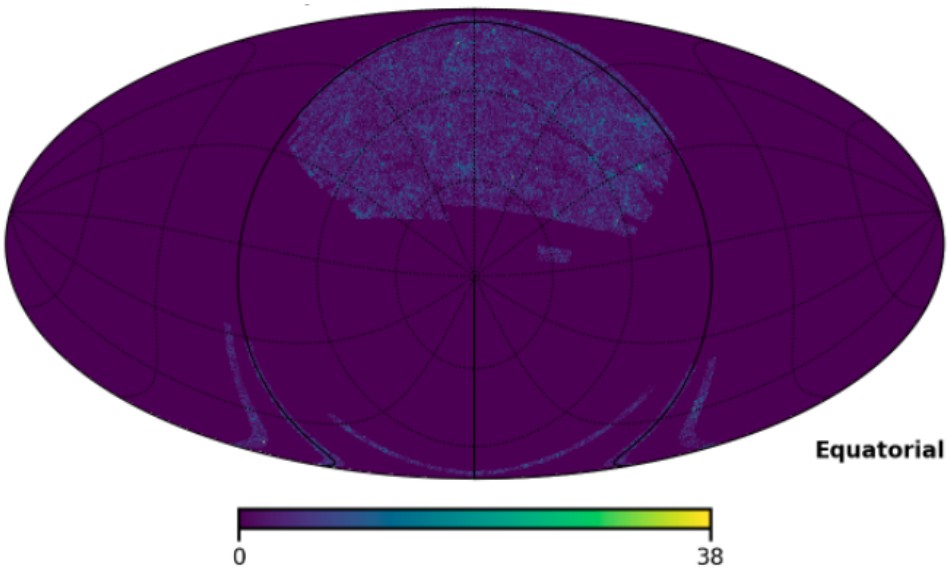

Figure A.7: The Mollview map of SDSS DR7 galaxy catalog in equatorial plane with Nside=256.

SDSS DR7 catalog also contains random catalogs which are dispersed inside the window with equal surface density and outside the mask. Fig. A.8, A.9 show the counts map which describe the number of galaxies in the each pixels in the Celestial sphere in both Galactic and Equatorial planes. Table A.2 shows different columns in the 'random0' file in the SDSS catalog.

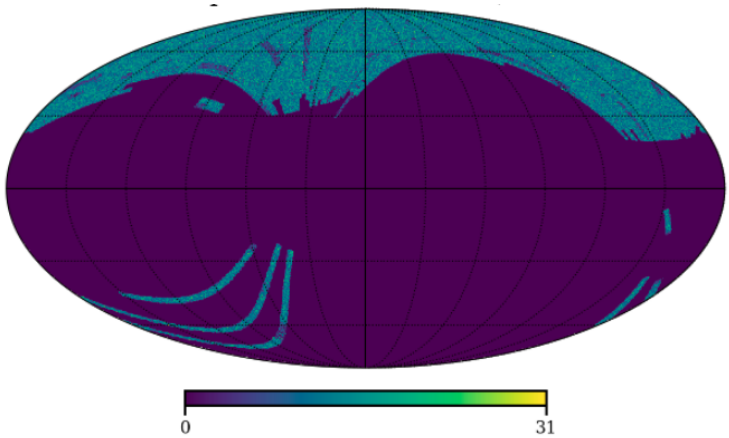

Figure A.8: The mollview map of 'random' file from SDSS galaxy catalog with Nside=256.

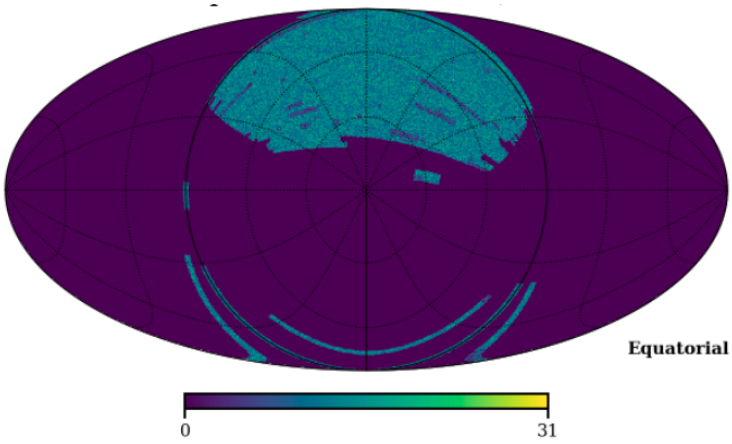

Figure A.9: The mollview map of SDSS galaxy catalog with Nside=256 in equatorial plane.

Table A.1: Information of each object mentioned in the SDSS catalog "safe0" file

SDSS catalog	Description
RA	Right ascension, J2000, degrees
DEC	Declination, J2000, degrees
Z	Redshift (set to -1 if not available)
M	Apparent magnitude (extinction-corrected r-band Petrosian)
WEIGHT	Weight related to north and south caps
MMAX	Main sample flux limit
IWINDOW	Index for this subsample of the polygon containing this object in the window file
ABSM	Absolute magnitudes in ugrizJHK bands
OBJECT POSITION	Index mentioned in the VAGC catalog
LETTER MASK	Bitmask describing what happened to this object:
0 (LETTER TARGET)	It is a target in the photometric catalog which passing our cuts
1 (LETTER TILED TARGET)	It was a tiled target in the target reductions
2 (LETTER TILED)	It was assigned a fiber on a tile
3 (LETTER TRIED)	Attempts were made to obtain a spectrum or a redshift by correcting a collision.
4 (LETTER GOT)	A redshift has been identified (by a spectrum or fixing of collisions)
5 (LETTER FIXED)	The collision was fixed to obtain the redshift.
6 (GALAXY)	It was referred to as a galaxy.

Table A.2: Information of each object mentioned in the SDSS catalog "random" file

SDSS catalog	Description
RA	Right ascension, J2000, degrees
DEC	Declination, J2000, degrees
FGOT	completeness of the map
MMAX	Main sample flux limit
WEIGHT	Weight related to north and south caps.

The footprint of galaxies in the NYU VAGC safe0 catalog is $7356 deg^2$. We use a sample of galaxies with $14.5 < r_{pet} < 17.6$ in which the lower bound guarantees that only galaxies with trustworthy SDSS photometry are utilized, and the upper bound enables uniform selection across the whole sample.
In order to have a more uniform sample, we only consider the north galactic cap. We only include regions where the completeness, calculated without considering missed galaxies due to fibre collisions, is greater than 0.9. Therefore, the footprint will be reduced to 6813 deg^2. We also applied more cuts on the NYU VAGC safe0 sample (inspired from Ref. [59]) as written in the following:

- We only used galaxies with $0 < z < 0.2$ (to sample at lower redshifts in comparison with BOSS)
- We put some colour cuts which make the sample more homogeneous (as a function of z) and enhance the clustering amplitude, which causes an increase in the mass of the halo hosting the galaxy.

After all these cuts applied on the galaxy and random catalogs, the maps of the final sample are as shown in the Fig. A.10, A.11, A.12, A.13. As a sanity check, we used this sample to reproduce the power spectrum similar to the one calculated in Ross et al. paper [59]. Figs. A.14,A.15 and A.16 show that our measurement is almost the same as the Ross et al. paper. Therefore, in the next step, we will delete all considered cuts (except the completeness and the cuts on locations) and measure the 3-dimensional power spectrum by considering all mentioned astrophysical features mentioned in section **??**.

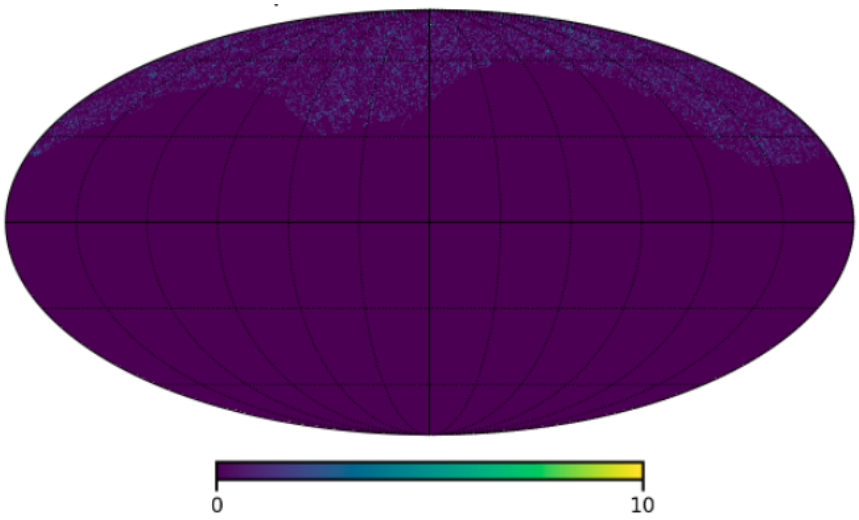

Figure A.10: The Mollview map of 'safe0' file from SDSS galaxy catalog with Nside=256.

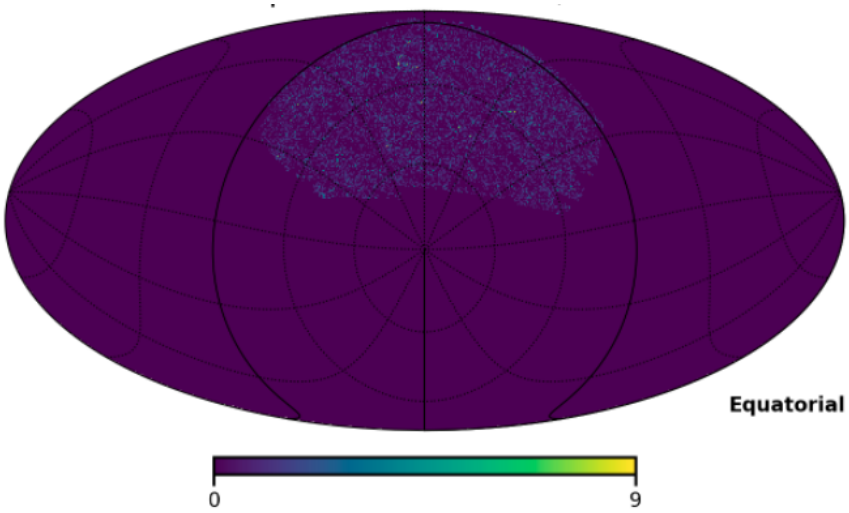

Figure A.11: The Mollview map of 'safe0' file from SDSS galaxy catalog with Nside=256 in equatorial plane.

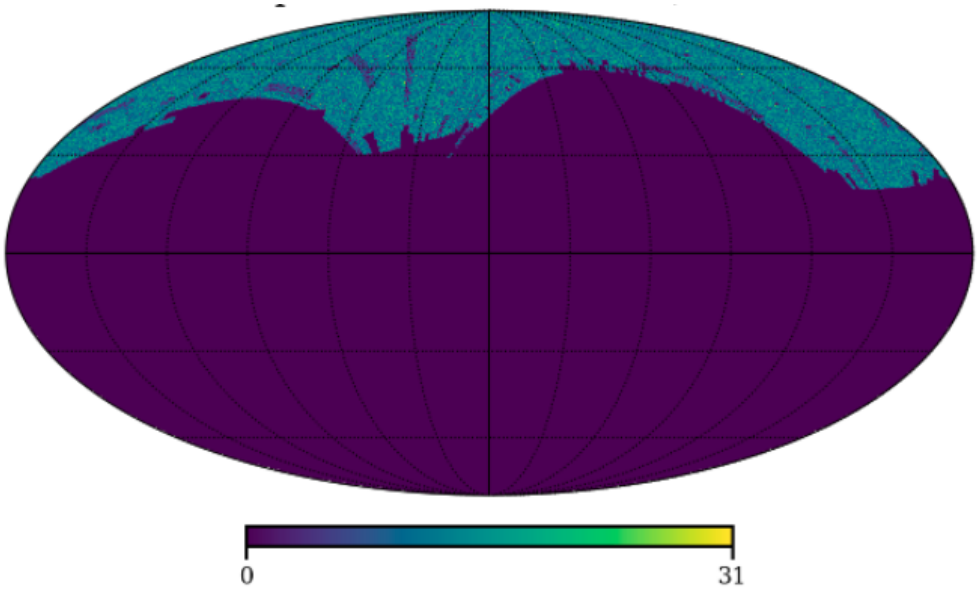

Figure A.12: The Mollview map of 'random0' file from SDSS galaxy catalog with Nside=256.

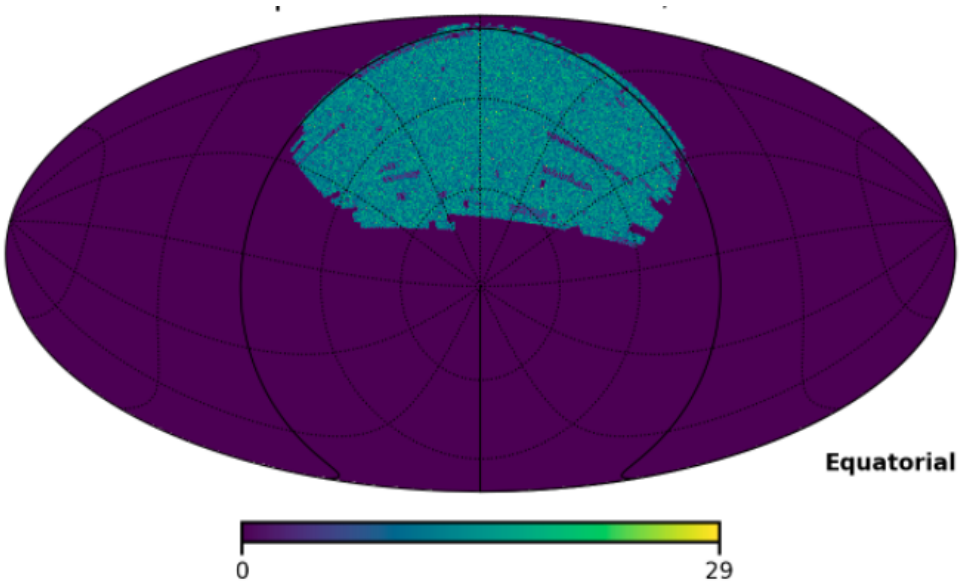

Figure A.13: The Mollview map of 'random0' file from SDSS galaxy catalog with Nside=256 in equatorial plane.

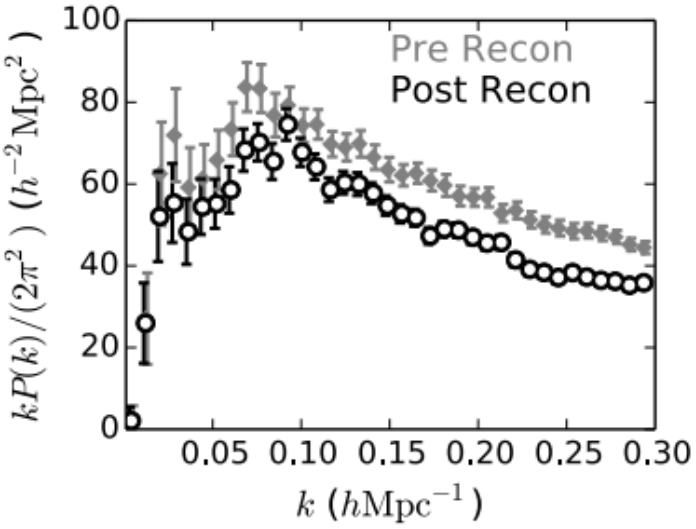

Figure A.14: 3D power spectrum obtained from Ross et al paper [59].

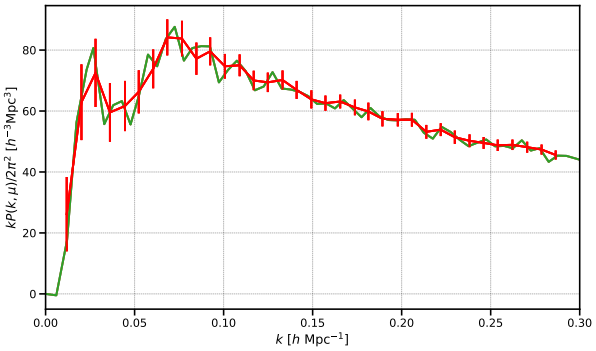

Figure A.15: 3D power spectrum obtained from our work.

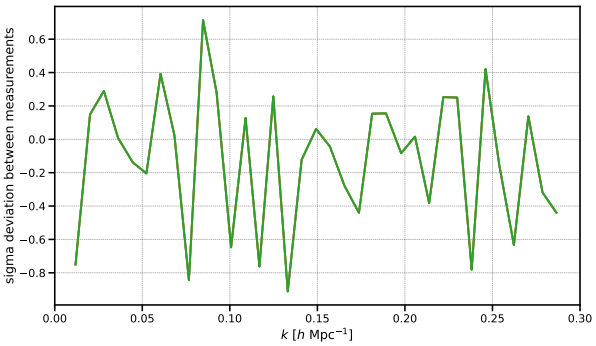

Figure A.16: Deviation in units of the 1-σ error bar from Ross et al measurement on galaxy power spectrum [59].

Appendix B

Notes on Details of the Code

Here we include the list of the inputs to the code along with a short description and their fiducial values for GLADE+. Values can be also adopted from any other galaxy surveys, namely, SDSS etc.

1. **Binning inputs**

   - Redshift binning information:
     $z_{min} = 0$, $z_{max} = 0.3$, $N_{bins} = 6$
   - BH mass number of bins. The fiducial value is set to one, just first to examine the effect of different host galaxy selection functions.
     $m_{bins} = 1$

2. **Inputs related to galaxy host selection functions**

   - The form of the selection function (a defined function in python). For now, we assume it is the unconditional (equation (5.19)).
     $p = P_{g,unconditional}$
   - Parameters of the function. The fiducial values basically means completely random selection. Also note that for GLADE+, we generated some random numbers for metallicity (just to keep the code coherent). Still, since the selection function for the metallicity part is set to a constant, it does not matter what are the values of metallicity of each galaxy. For SFR, though, we use the mean cosmological value.
     $p_{args} = [0, 0, 5, 0, 4000, 0, 0, 0.02 * 1e9, 0, 0.14 * 1e9, 0, 0, 0.5, 0, 1]$

These numbers are 15 numbers which are 3 sets of 5 numbers for mass, SFR, and as follows (basically parameters in equation (5.17)):
$p_{args} = [\alpha_M, \beta_M, M^*, M_{min}, M_{max}, \alpha_{SFR}, \beta_{SFR}, SFR^*, SFR_{min}, SFR_{max}, \alpha_Z, \beta_Z, Z^*, Z_{min}, Z_{max}]$

- Type of the input for SFR, which here is from the model.
  SFR-Z-type='model'

3. **Inputs related to BH mass modelling**
   Here we set $m_{bins} = 1$, so the mass modelling does not matter because we will not bin in BH mass. However, we need to specify these values due to the structure of the code. If we change the number of BH mass bins, we get different results for each bin affected by these inputs. Here we have two options:

   (I) Physical mass modelling:

   - Type of the mass modelling:
     p-m1-type='phys'
   - Name of the probability function:
     p-m1=m-kroupa
   - Parameters of the model:
     $p\_m1\_args = [5, 50, 2.3, 10^{-4}, 45, 1.5, -0.44, 0.0175]$
     where are gotten from equation (5.9), (**??**), and (5.12),respectively:
     $[m_{min}, m_{max}, \alpha, Z_*, M_{PISN}(Z_*), \alpha, \gamma, \zeta]$

   (II) Phenomenological mass modelling:

   - Type of the mass modelling:
     p-m1-type='phen'
   - Name of the probability function:
     p-m1=m-peak-model
   - Parameters of the model:
     $p\_m1\_args = [5, 50, 2.3, 30, 2.6, .05]$
     where respectively are from equation (5.9), (5.10),respectively:
     $[m_{min}, m_{max}, \alpha, \mu_g, \sigma_g, \lambda_g]$

   In addition, we also need inputs for the secondary mass of the binary system:

- name of the function:
  p-m2=sec-mass-sample-beta
- parameters ($[m_{min}, \beta]$):
  p-m2-args=[5,1]

4. Number of redshift in which we produce the window function (equation 5.14)). It is nothing about physics; just because it is time-consuming to calculate the window function for every siren, we do it for some redshifts and each siren, we use the one with the closest redshift.
   $n_z = 10$

5. **Inputs for amplifying the number of mergers:**
   ampl=1e4 , obs-time = 1

6. **Inputs related to the merger rage:**
   $t_{min} = 500e6$, $\kappa = 1$, grid-points=1999

7. **Inputs related to masking:**
   thresh=15 , nside-map=512 , nside-mask=256

Appendix C

Flowchart of the Code

Fig. C.1, provides a schematic description of different modules in the code. The main tasks are divided into 5 different parts. In the first part we calculate the number of mergers by implementing star formation rate density and delay-time distribution. In the second one, we apply our own masking prescription on the catalogs to make them more uniform in order to prevent additional bias (for example, we neglect under-dense and over-dense areas of catalogs). In the third and forth steps, we model the mass distribution of black holes and select host galaxies based on their astrophysical properties (such as mass, metallicity and SFR). In the last part, we calculate the 2D angular and 3D power (using nbody kit) spectrum with shot noise subtraction mentioned in chapter 5 and finally compute the bias parameter.

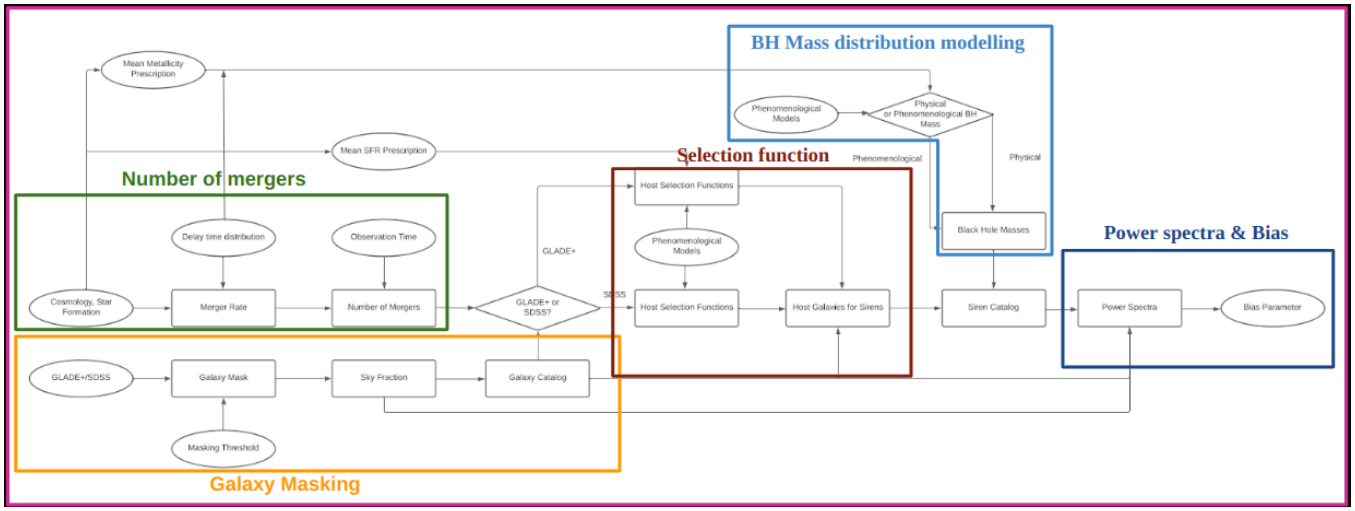

Figure C.1: The flowchart shows the steps in the numerical package.

I contributed to these parts of the code:

- Implementation the SFR, delay-time distribution and number of mergers.
- Masking both GLADE+ and SDSS DR7 catalogs (note that, codes related to the shot-noise subtraction are implemented by my collaborators).
- Implementing codes related to the calculation of the power spectra and bias parameter and feed them in the main body code.
- Implementing all codes related to SDSS DR7 catalog (relating the main body codes and 3D power spectra codes) and implementing the selection function for SDSS DR7.
- Implementing error bars for power spectrum and bias for SDSS DR7.